MAGNETIC PROPERTIES OF THE PYROCHLORE $HO_2RU_2O_7$

Magnetic properties of the pyrochlore $Ho_2Ru_2O_7$

By

SUNG-JAE KIM, B.Sc

A Thesis
Submitted to the School of Graduate Studies
in Partial Fulfilment of the Requirements
for the Degree
Master of Science

McMaster University

ABSTRACT

In this thesis, we investigated a recent and interesting issue in magnetism; **spin ice**, which is a term used for systems where there is a analogy between their magnetic structure and the proton structure of water ice. Until now, only three spin ices, $Dy_2Ti_2O_7$, $Ho_2Ti_2O_7$, and $Ho_2Sn_2O_7$, have been discovered. In 2002, $Ho_2Ru_2O_7$ was proposed as a candidate spin ice by Bansal *et al.* Given the similar structure and experimental behaviors of $Ho_2Ru_2O_7$ and known spin ice systems, it has been an issue whether $Ho_2Ru_2O_7$ is the fourth spin ice.

In order to determine whether the new candidate is spin ice or not, the magnetic characteristics of $Ho_2Ru_2O_7$ have been investigated. The frustrated system $Ho_2Ru_2O_7$ has a pyrochlore structure with magnetic spins located on lattice of corner sharing tetrahedra. The crystal field originated <1 1 1> anisotropy of this sites and ferromagnetic interaction of spins give the preference of a two spin in and two spin out to a center of the tetrahedra.

High quality polycrystalline samples were prepared and crystal growth attempts were made, then various measurements have been conducted. DC susceptibility data were used to determine the effective magnetic moment and value of Weiss temperature(θ). Zero field cooled (ZFC) and field cooled (FC) susceptibility data show a small irreversibility below 95K, which indicate ruthenium antiferromagnetic ordering. AC susceptibility measurements show a strong frequency dependence of the susceptibility which is a feature characteristic of spin glass or superparamagnetic materials.

Specific heat experiments were conducted to also confirm the existence of Ru magnetic ordering at 95 K. The Debye temperature is estimated to be $\sim$441 K.

μSR measurements were conducted at TRIUMF. The measurements of $Ho_2Ru_2O_7$ show signatures of ruthenium ordering near 95K and holmium near 1.4K. In agree-

ment with previous neutron scattering experiment we conclude that the ground state of $Ho_2Ru_2O_7$ is antiferromagnetic rather than spin ice. Presumably the ruthenium ordering acts to preclude the holmium moments entering the spin ice state.

Contents

List of Tables

List of Figures

Acknowledgments

Since I came to Canada, even though I considered myself planned and prepared; living in foreign country has been stressful experience. I was shocked by cultural differences which are sometime unpleasant. There are always good Samaritan's field that help me to overcome all the fluctuating difficulties.

I would like to express my sincere appreciation to my supervisor Graeme Luke for his guidance, support and advice which helped me in fulfilling my endeavor. I particularly appreciate his patience and understanding which is the virtue of the good Canadian.

I would like to acknowledge the assistance of my group members. Chris Wiebe has been patient to answer even my dumb questions. Greg MacDougall helped me with knowing Canada and thesis writing not to mention the inspiring physics discussions. Jose Rodriguez has always eager to help other people, and his comments shape this thesis.

I am deeply grateful to Jung-seek Hwang for assistance and advice provided throughout my stay at McMaster. I am also indebted to Tom Timusk for his support and David Venus for teaching the Condensed Matter Physics.

Special thanks Hanna Dabkowska her guidance in crystal growth experiments and Gord Hewitson, Paul Dube and all researchers and technicians for keeping the instruments and for a supply of liquid Helium.

I am also grateful to the following for their invaluable help: Yang Jing, Fan Lung, Zaho Yang, Athena Sefat, Heather Cuthbert, Mari-Angela Zumburabiri and Diego Lozano-Gorrin. I consider myself lucky to have a chance to work with all these talented people.

Finally, I wish to thank my wife for her loving support.

Chapter 1

Introduction

Dirt can be brushed aside or swept under the rug, but sooner or later it demands attention.

- Daniel L. Stein -

One of the most challenging subjects in the history of science is to understand condensed matter. In the 20th century, humankind has achieved considerable success on understanding what condensed matter is. However, the success was mainly for crystalline materials, referred to as ordered systems, because it is easy for people to deal with such systems mathematically and simply model their physical properties.

Ironically, in the real world, there are no perfectly ordered materials. Every bulk crystal matter has some disorder which spoils the perfect order; moreover much condensed matter is intrinsically disordered. Our understanding of these disordered system remains relatively primitive, despite the last three decades of study.

By the early 1970's, however, physicists were challenged to confront disorder. One of the most important attempts to understanding disordered systems has been the study of spin glasses[1]. Normal glasses are disordered crystallographically whereas spin glasses are magnetically disordered materials. Just as the atoms in a glass are frozen in random positions (unlike those in a crystal, which are ordered in a regular

periodic array), the magnetic moments in a spin glass freeze with random orientations. This discovery meant scientists could make and control the physical properties easily, and scientific interest on spin glasses materials exploded in the 1980s [2]. Moreover, the interest expanded outside the condensed matter physics community to neural network research, protein biophysics, the origin of life, computer algorithms, and others[3, 4, 5].

1.1 Frustration and Disordered Systems

A frustrated system is one whose symmetry hinders the possibility of every spin interaction in the system being satisfied at the same time. Frustration arise from either spatial randomness or geometrical arrangement of spins [6]. As seen in figure (1.1), there are two kinds of spin frustration mechanisms.

Firstly figure (1.1 (a)) is a spin glass below the freezing temperature. If only first-neighbor interaction $J_1 > 0$ (ferromagnetic) and second-neighbor interaction $J_2 < 0$ (antiferromagnetic) exist and $|J_1| = 2|J_2|$. The green arrow's total interaction is zero which indicate the spin frustrated. Philip Anderson assumed that all interaction is random and for canonical spin glasses exchange interaction between moments is RKKY[2, 5]. However those condition also give the same result.

Secondly figure (1.1 (b)) displays that the geometrical structure of spin arrangement and spin interactions determine the frustration.

1) If a magnetic ion with a spin occupies a corner of a triangle, and the spin interactions are ferromagnetic (left figure), then all spins can be aligned to the same direction. This material is magnetically ordered as a typical ferromagnet.

2) If the spin interactions are anti-ferromagnetic. It is easy to make two spins align on a triangle, but hard to suggest what will then happen to the third. This system exhibits geometrically frustrated magnetism. The frustration of the interactions leads to huge number of ground states of equal energy, and so the system is degenerate and

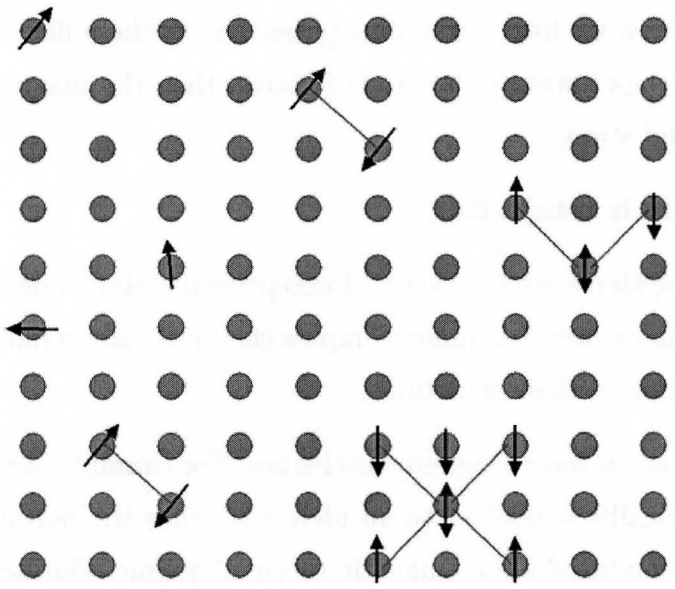

(A)

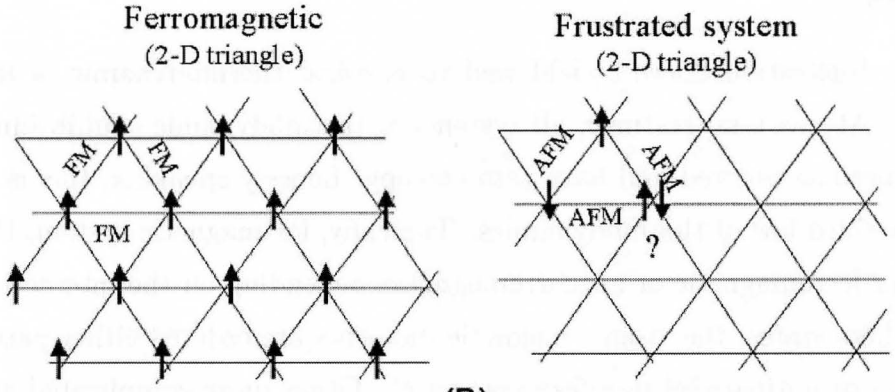

(B)

Figure 1.1: (a)Frustration of frozen states in canonical spin glasses. magnetic material bearing magnetic moments is diluted in nonmagnetic host. The double ended arrows display frustrated moments. Exchange interaction between moments is RKKY for canonical spin glasses. (b)Comparison of the ordered spin system and geometrically frustrated spin system. The combination of geometry and anti-ferromagnetic interaction make the geometrical frustration.

there is no unique ground state. The magnet may be able to move from one ground state to another if there are low or zero energy barriers to these fluctuations. If there are large energy barriers between the ground states, then the magnet will be frozen in a particular ground state.

Why frustration is interesting?

First, frustrated systems are not rare and exceptional states. They are ubiquitous. Scientists have become aware that many complex chemical compounds, as well as bio-matter have frustration in their structures.

Many states of matter have magnetic analogues. For example, a simple paramagnet is thermodynamically equivalent to an ideal gas, since the non-interacting spins of the paramagnetic material obey magnetic thermodynamic relationships which are equivalent to the familiar P,V,T variables governing an ideal gas. As with an ideal gas, a paramagnet deviates from ideality, because of interactions between the spins or molecules.

Finally, frustration doesn't yield well to classical thermodynamic or statistical mechanics. At low temperatures, all systems in thermodynamic equilibrium are expected to become ordered and have zero entropy. Loosely speaking, this is a way of stating the third law of thermodynamics. Typically, for magnetic system, the ordering is either ferromagnetic or antiferromagnetic, depending on the interaction of the spins. In these states, the atomic magnetic moments are ordered either parallel (ferromagnetic) or antiparallel (antiferromagnetic). Other more complicated structures such as ferri-magnetism are also possible. However, scientists have discovered that ordering is not always possible and surprisingly there are many examples of this (ice, spin glasses or spin liquid). In the case of geometrically frustrated systems, disordered states continue down apparently to zero temperature. The lack of unique order is incompatible with the third law of thermodynamics. It is expected that in real systems very small perturbations such as the dipolar interaction will become important and lead to order at very low temperatures.

Recently, the discovery of superconductivity in a pyrochlore lattice structured

transition-metal oxide (KOs_2O_6) was reported[5]. Although in that system the T_c is not so high, frustration might be an important element in the solution of the elusive high T_c superconductors. Beside condensed matter physics, frustration draws a growing interest in other academic communities. Understanding frustrated systems may lead to the creation of longer-life batteries and so-called ferromagnetic semiconductors, a class of materials in which the magnetic moments can be used to carry information in electronic devices.

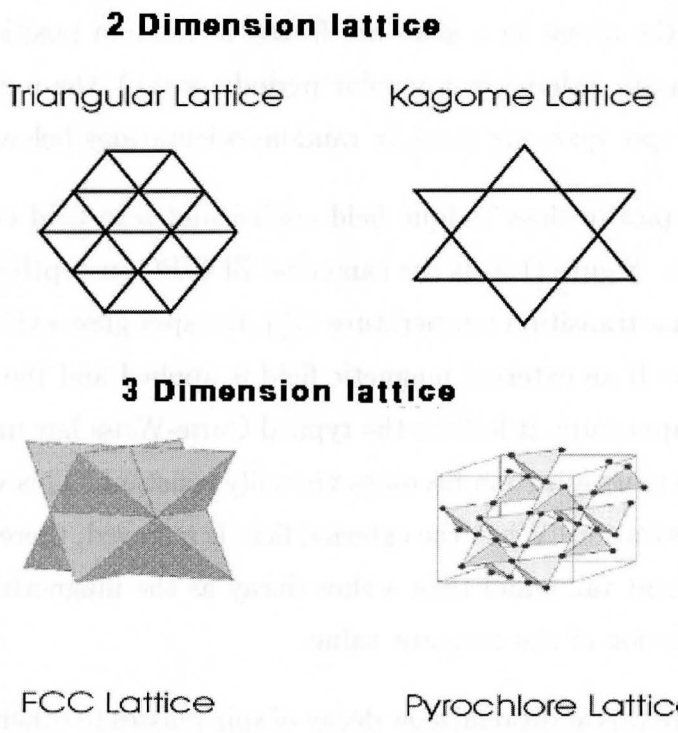

Figure 1.2: Common geometrical frustration lattices. Taken from reference [6]

1.2 Spin Glasses and Spin Ice

Both spin glasses and spin ice are disordered systems and show frustration phenomena. Spin glass have been researched for three decades but in recent years, a new kind disordered system, spin ice has been also studied.

Spin Glasses

Ordinary glasses have only short range ordered lattice atoms. Although a glass looks solid, it is actually a slow flowing liquid that is too slow to be recognized. Similarly, spin glass has short range magnetic spin ordering, and those magnetic spin moments are apparently frozen below certain temperature (spin glass transition temperature, T_g *or* T_f) which depends on the measurement frequency. In terms of magnetism, a spin glass is a disordered system where frustration is caused by the disorder. Just as the atoms in a glass are frozen in random positions (unlike those in a crystal, which are ordered in a regular periodic array), the moments associated with the ions in a spin glass are stuck in random orientations below T_g.

Spin glasses typically show unique field cooled and zero field cooled magnetization characteristics. Figure (1.3) is the canonical ZFC-FC susceptibility of spin glass. Above the spin glass transition temperature (T_g), the spin glass exhibits typical paramagnetic behavior. If an external magnetic field is applied and the magnetization is plotted versus temperature, it follows the typical Curie-Weiss law until T_g is reached, at which point the magnetization becomes virtually constant. This value is called the field cooled magnetization. When the external field is removed, there would be a rapid change to a remanent value and then a slow decay as the magnetization approaches zero or a small fraction of the remnant value.

We can compare this additional slow decay of spin glasses to other typical magnetic materials. For paramagnetism, when the external field is removed, the magnetization should rapidly go to zero. For ferromagnetism, the magnetization goes to a remnant value and then remains constant. In each case, the change is very rapid, but if carefully examined, it is exponential decay with a very small time constant. This time is related to relaxation rate which is a important physical factor for spin dynamics of the material. For spin glasses, very slow additional decay (often non exponential) is consistent with the idea of the glassiness of the spin glass state with many separating high energy barriers. Figure (1.4) shows typical time evolution of magnetization.

If a spin glass is cooled below T_g in the absence of an external field, and then

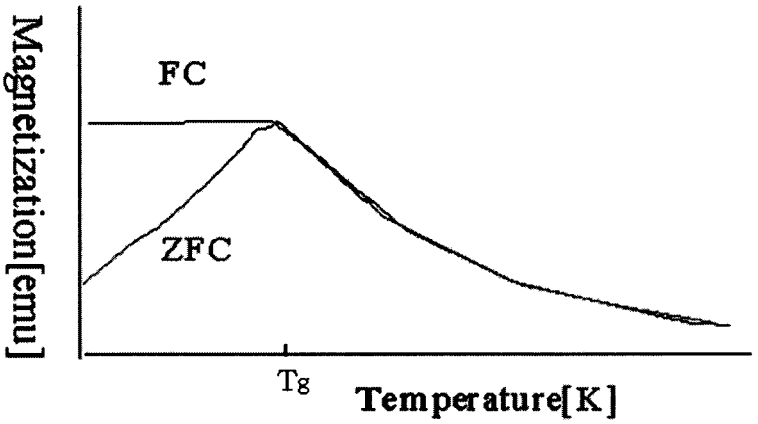

Figure 1.3: Irreversibility between FC and ZFC of static susceptibility of dilute spin glass $MnCu$. The onset temperature of χ_{zfc} and χ_{fc} divergence is glass temperature (T_g or T_f)

a field is applied. There is a rapid increase to a value called the zero-field-cooled magnetization, which is less then the field cooled magnetization, followed by a slow upward drift toward the field cooled value. This irreversibility between field cooled and zero field cooled is interesting fingerprint of spin glass behavior.

In addition to a field-cooled (FC) and, zero field-cooled (ZFC) divergence below T_g, there are several other experimental signatures of the spin glasses. One can also observe a strong frequency dependence in the AC susceptibility (both χ' [1] and χ'') below T_g, T^1 dependence of the electronic contribution to the heat capacity at very low temperatures [8], a sharp decrease in the spin fluctuation or spin relaxation time as measured by inelastic neutron scattering and muon spin relaxation below T_g [9], and the absence of long range order from neutron diffraction.

Spin Ice

For many years it was thought that frustration plays a role only in antiferromagnets, but recently it was shown that a new phase occurs in pyrochlore lattice with ferromagnetic interactions and strong <1 1 1> anisotropy. This phase, termed "spin ice" was discovered by Harris and coworkers [11]. Making an analogy between the

[1] χ' is a real part of susceptibility and χ'' a imaginary part of susceptibility

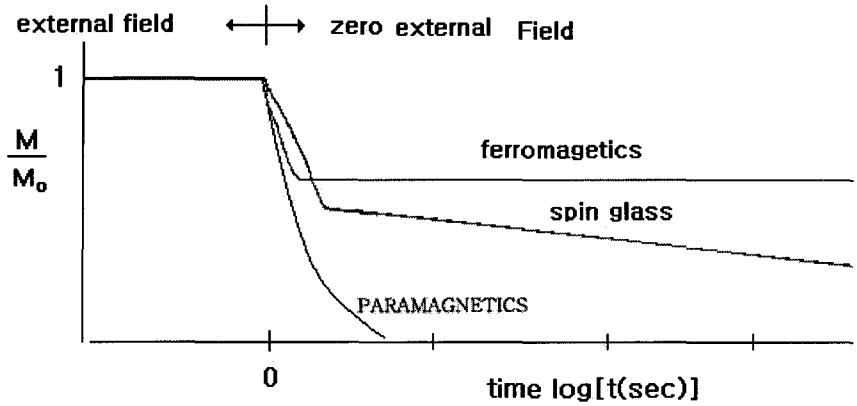

Figure 1.4: Magnetization time evolution. M_0 is the saturation magnetization. Removing external field at time = 0 shows different relaxation response with some magnetic systems

spin directions to the disordered hydrogen bonds of Pauling's cubic ice model, their system was shown to remain disordered even at $T = 0$ with a finite entropy.

In ice the position of protons are disordered. Ice has a residual entropy which has been measured and calculated, explained by Linus Pauling in his book *The Nature of the Chemical Bond*[15]. As seen in figure (1.5), the oxygen atoms form a fully ordered lattice, where each one has two closely bonded hydrogen atoms, and two distantly bonded atoms. A ground state exists when all oxygen atoms have two close and two distant hydrogen atoms. This is known as the ice rule. The ice rule can be satisfied in six ways for each oxygen atom, and the selection of a ground state at one oxygen does not constrain the ground state of the adjoining oxygens. Hence, the hydrogen atoms can remain disordered.

Known spin ices have the face centered cubic structure (space group $Fd\bar{3}m$) of the mineral pyrochlore as seen in figure (1.5). In these structures also have two interpenetrating sublattices, each consisting of corner sharing tetrahedra of metal ions[14]. The magnetic ions may lie on the vertices of a sublattice. In these systems, the rare earth moments experience a strong axial anisotropy and so can be treated as Ising spins. An Ising spin is one which can point in only two opposite directions, for

example inward or outward to the center of tetrahedron. The interaction between the spins is ferromagnetic, then the minimum energy configuration will have two-spin-in and two-spin-out as seen in figure (1.6). This is analogous to the proton disorder in water ice and is a good example of the many highly frustrated system yet discovered.

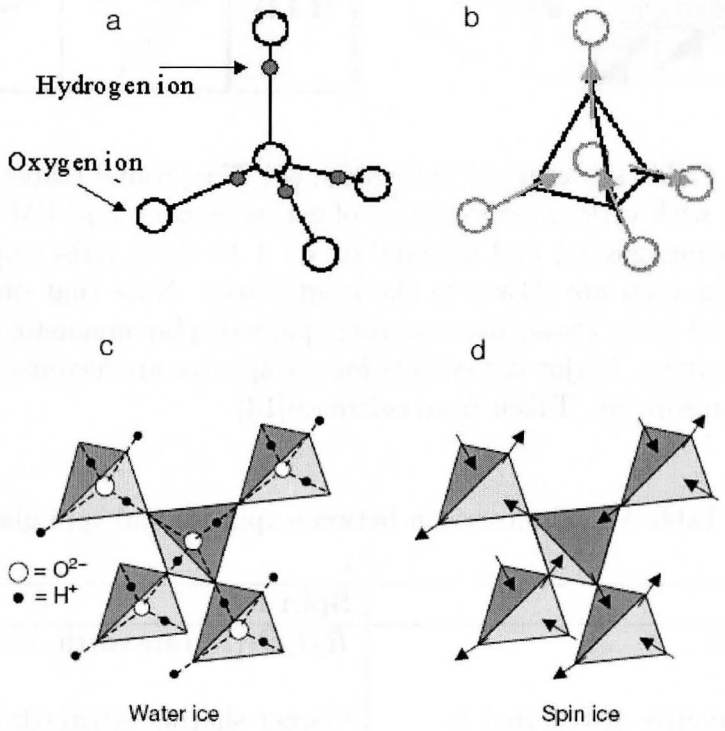

Figure 1.5: Spin Ice system analogy with water ice (a) Hydrogen bonding with oxygen in water ice (b) Spin ordering in tetrahedron lattice (c,d) six-fold symmetry of in water ice. There are no energy barrier over hexagonal structure, this may cause the fluctuation of spin ice at low temperature. Taken from reference[10].

The ground state has two spins pointing into the tetrahedron and two pointing out. Because there are huge number of tetrahedron in the sample, there is an extensively degenerate ground state and disordering of the moments throughout a crystal. The disorder persists, even to very low temperatures (this has been confirmed by neutron diffraction at ~50mK) in $Ho_2Ti_2O_7$ [11, 12].

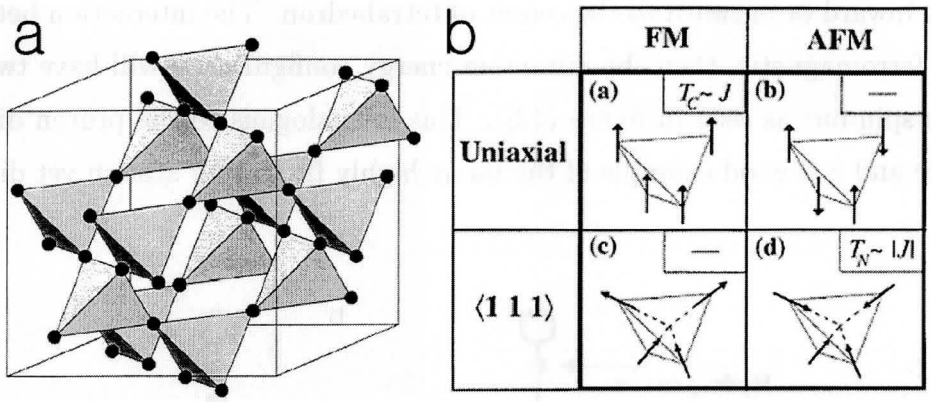

Figure 1.6: (a) Cubic structure of pyrochlore (b) The ground states of a single tetrahedron of spins with various combination of exchange coupling(FM = ferromagnetic, AFM = antiferromagnetic) and uniaxial or <1 1 1> Ising anisotropy. The ordering temperatures for each are shown in the inset boxes. Note that only the (uniaxial-ferromagnet) and (<11 1>-antiferromagnet) pairs display magnetic phase transitions at finite temperature. Major ingredients for the spin ice are ferromagnetic interaction and <1 1 1> anisotropy. Taken from reference[13].

Table 1.1: Comparison between spin ice and spin glass

Spin glass	**Spin ice**
$AuFe$, $CuMn$	$R_2T_2O_7$(R: rare earth, T: transition metal)
Spins are randomly distributed in the nonmagnetic metal and frozen below T_g (almost static random spins)	Corner sharing tetrahedral magnetic ions. Geometrical frustration prevent magnetic moments from ordering, No long range order down to 50 mk
No long range order between spins	No long range order between spins
very slow spin fluctuation below T_g	No distinctive T_g, slow spin fluctuation at low temperature

1.2.1 New spin ice candidate $Ho_2Ru_2O_7$

Until now, only three spin ices, $Dy_2Ti_2O_7$, $Ho_2Ti_2O_7$, and $Ho_2Sn_2O_7$ have been discovered [10]. In 2002, $Ho_2Ru_2O_7$ was proposed as a candidate spin ice by Bansal

et al. [16]. The $Ho_2Ru_2O_7$ system shows the similar structure and experimental behaviors with known spin ice systems. Moreover $Ho_2Ru_2O_7$ system is an effective Ising spin one-half system due to a strong <1 1 1> anisotropy and has effective ferromagnetic interaction between holmium moments. It could be the next spin ice. However, unlike other spin ices $Ho_2Ru_2O_7$ also has Ru^{4+} moments contributing the magnetic properties as well as Ho^{3+} magnetic moments. It has been unknown how the magnetic Ru^{4+} moment affects the system's magnetic properties.

More recently, Wiebe *et al.* [17] reported the long range antiferromagnetic order of holmium below 1.4K using samples that were grown for the experiments described in this thesis. Our explanation of the holmium ordering was that the internal magnetic field lifted the degeneracy of the spin ice state and at least partially removed the frustration allowing the Ho^{3+} moments to order. That is strong evidence that $Ho_2Ru_2O_7$ is not spin ice.

We performed several experimental technique such as DC, AC susceptibility, specific heat and μSR to examine the properties of $Ho_2Ru_2O_7$ and contribute to our understanding of the interesting system. Especially μSR is very sensitive magnetic probe to determine the magnetic properties of materials.

Chapter 2

Sample Preparation and Verification

Synthesizing of $Ho_2Ru_2O_7$ poly-crystalline samples is similar to that of ordinary ceramics. Normal ceramics includes earthenware, porcelain, bricks, and some kinds of tile and stoneware. Ceramic materials are compounds of inorganic materials and made rigid by exposure by heat. Usually, a ceramic sample is easily made and can be used as a starting material to grow a single crystal sample.

As described below, high quality $Ho_2Ru_2O_7$ ceramic samples were obtained from holmium oxide and ruthenium metal powder. X-ray diffraction measurements show that the $Ho_2Ru_2O_7$ polycrystalline samples where quite pure, having less than 1% impurities as seen in figure (2.4).

Generally, achieving an appropriately-sized single crystal is much more difficult than ceramics. However, it is valuable to have single-crystals in order to identify the anisotropic properties of the material. Moreover, single crystals may be more stable so that one can preserve them for longer time.

2.1 Synthesis and Verification of Ceramic Samples

Ceramics samples were produced from highly pure powders of holmium oxide and ruthenium metal. Alumina crucibles were used to prevent sample from contamination during heating, because alumina has a high melting point and gives off minimal amounts of contamination. All preparations were done in air. Holmium, Ho, is one

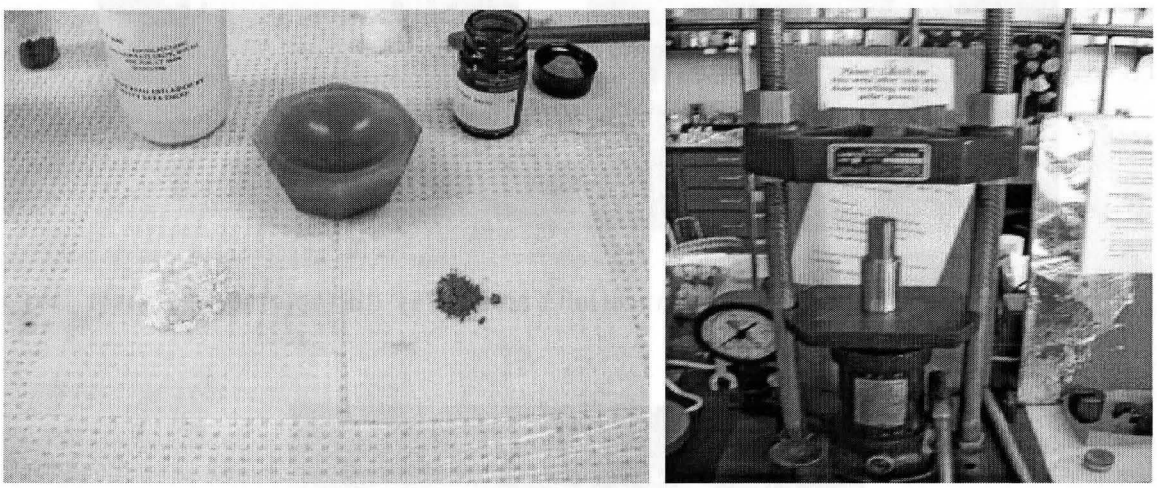

(a) (b)

Figure 2.1: (a) powder form holmium oxide (left) and ruthenium (right) (b) hydraulic press and stainless steel template

of the least abundant of the rare earth metals. It is a silver-colored metallic element and is one of the most strongly paramagnetic materials known. Very pure Ho_2O_3 (99.9%), which is a pinkish-white powder, was used for the reaction.

Ruthenium, Ru, is a gray-colored transition metal. Pure ruthenium metal powder was used for the reaction.

In the previous work by Bansal *et al.*[16], ceramic samples were prepared by mixing RuO_2 and Ho_2O_3. When we replicated Bansal's sample preparation method, we have found that the ruthenium oxide evaporated before it reacted with the holmium oxide[1].

[1]Bansal *et at.* might used a sealed container for the sintering.

Figure 2.2: High Temperature furance(left) and X-ray diffractometer(Bruker D8)

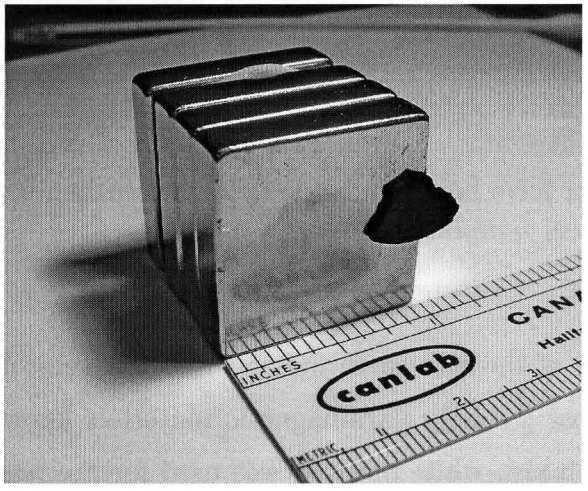

Figure 2.3: Black $Ho_2Ru_2O_7$ ceramic sample stuck to a NdFeB permanent magnet at room temperature. The large magnetic moment of Ho^{3+} causes this strong paramagnetism.

As a result, we got some impurities such as holmium oxide and ruthenium crystal. The holmium oxides mixed in with the $Ho_2Ru_2O_7$ sample and the ruthenium crystal was shiny and stuck on the crucible wall.

Table 2.1: Brief summary of physical characteristics of Ho and Ru

	Holmium(Ho)	Rutenium(Ru)
atomic number	67	44
Molar mass	164.93 g	101.07 g
Melting point	1474	2310
boiling point	2700	3900
Electron structure	[Xe] $4f^{3}5d^{0}6s^{2}$	[Kr] $4d^{7}5s^{1}$
crystal type	hexagonal	hexagonal
density	9.05	2.7
lattice constant	3.58	2.70

In order to solve the problem, We used ruthenium metal powder rather than ruthenium oxide. It proved that only small amount of ruthenium metal powder is evaporated.

These two materials were reacted according to the following chemical equation:

$$Ho_2O_3(powder) + 2Ru(metal\ powder) + 2O_2 \rightarrow Ho_2Ru_2O_7 \tag{2.1}$$

The mixing and reacting procedure was as follow:

First, all reactant powder was heated to remove impurities and moisture before mixing. Then, we weighed the desired amount of each constituent reactant, and poured into a mortar to mix them thoroughly. At this point, one notices that the color of the mixed powder changes to grey. The mixed powder was poured into a steel template to squeeze it into a pellet with a hydraulic press. The purpose of pressing the powder into a pellet was to make the grains closer together, and react better. It is worth noting that 2% excess ruthenium powder was added, because there is always some amount of ruthenium evaporation.

To reduce the contamination from the alumina crucible below the pellet during firing, powder left over from the pressing procedure was spread onto the bottom of the crucible. A PID controlled furnace was preheated to 850 C, and the pellet was sintered for 24 hours. The color of the pellet changed from grey to black, which demonstrated that a reaction took place. Most of the chemical reaction was done

during this stage. After cooling in air, the pellets were weighed to determine the mass change. There was no noticeable change.

X-ray showed some residual impurities phase due to incomplete reaction. We then crushed the samples into powder form and squeezed them into pellet form again. Then, we heated them to 1200 C for 48 hours. Through this heat treatment, we eliminated the remaining impurity phase.

2.2 X-ray Diffraction Measurement of The Ceramic Sample

Powder X-ray diffraction measurement is a conventional method to check the purity of a sample. A beam of x-rays is passed through a sample of randomly-oriented minute crystals, producing a distinctive circular pattern which is unique to each material. An x-ray detector rotates and detects the intensity of the diffracted x-ray beam around sample. Powder x-ray diffraction provides less information than single crystal diffraction. However, it is much simpler and faster. A Bruker D8 x-ray diffractometer was used for the measurement.

X-ray diffraction data show that the impurity ratio is less than 1 % by comparing amplitude of peaks. Also, the first heat treatment was enough to provide a quite pure $Ho_2Ru_2O_7$ powder sample. As one can see from the following figure, the dominant impurity in our sample is RuO, and the intensity of these peaks is small compared to $Ho_2Ru_2O_7$.

2.3 Single Crystal Growth Attempt

There are many methods for growing bulk single crystals, such as floating zone furnaces, flux growth, and the Bridgeman and Czochralski technique. The Czochralski

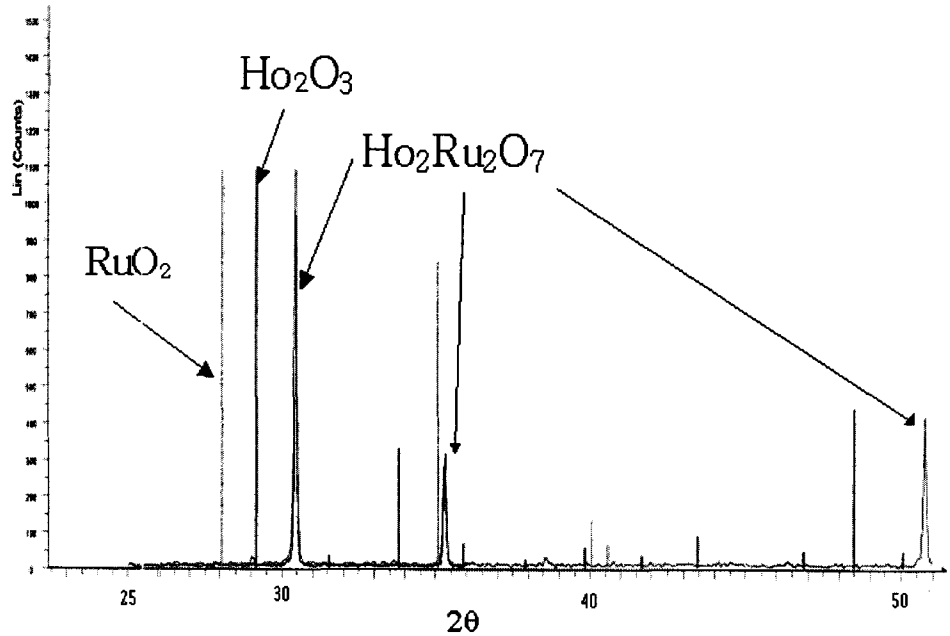

Figure 2.4: X-ray diffraction data for $Ho_2Ru_2O_7$. Note that impurity peak of RuO_2 and Ho_2O_3 is quite small compare to $Ho_2Ru_2O_7$ peak. Only reference peaks of RuO_2 and Ho_2O_3 are shown.

technique is commonly used for mass production[2] in the semiconductor industry, and the optical floating zone method is used for smaller but lower impurity samples, because there is no use of crucibles, which is dominant source of contamination.

Preparation

Sintered ceramic pallets were ground and then packed into a rubber tube which was then pressurized in a water chamber of a hydraulic press at 50 MPa for 15 minutes. After taking the sample out form the hydraulic press, the sample was removed by cutting the rubber tube. This process is tricky because $Ho_2Ru_2O_7$ polycrystalline powder sample is soft and brittle without a bonding material to hold the powder together.

Optical Floating Zone Furnace

[2]diameter of standard crystal ingot is over 25 cm

A schematic setup of optical floating zone furnace (also called image furnace) is shown in Figure (2.5). A high-purity polycrystalline rod is suspended above seed material at the bottom, and both are vertically aligned and rotated. The rod is enclosed in a cylindrical quartz tube within which mixtures of various gases, such as argon, nitrogen or oxygen, is maintained. During the growth process, a small zone ($\sim$0.5 cm) of molten material is created by strong light focused by elliptical mirrors. The molten material is contained by surface tension. One moves the molten zone downward, so that it traverses the whole length of the rod.

Unfortunately, several attempts of single crystal growth failed, because significant amount of ruthenium evaporated before the reaction took place. The $Ho_2Ru_2O_7$ started to decompose around 1600 degrees Celsius, and the remaining sample wouldn't melt for temperatures up to $\sim$2000 ^oC. Despite this failure, other techniques such as a flux growth method are worth trying to get a single crystal.

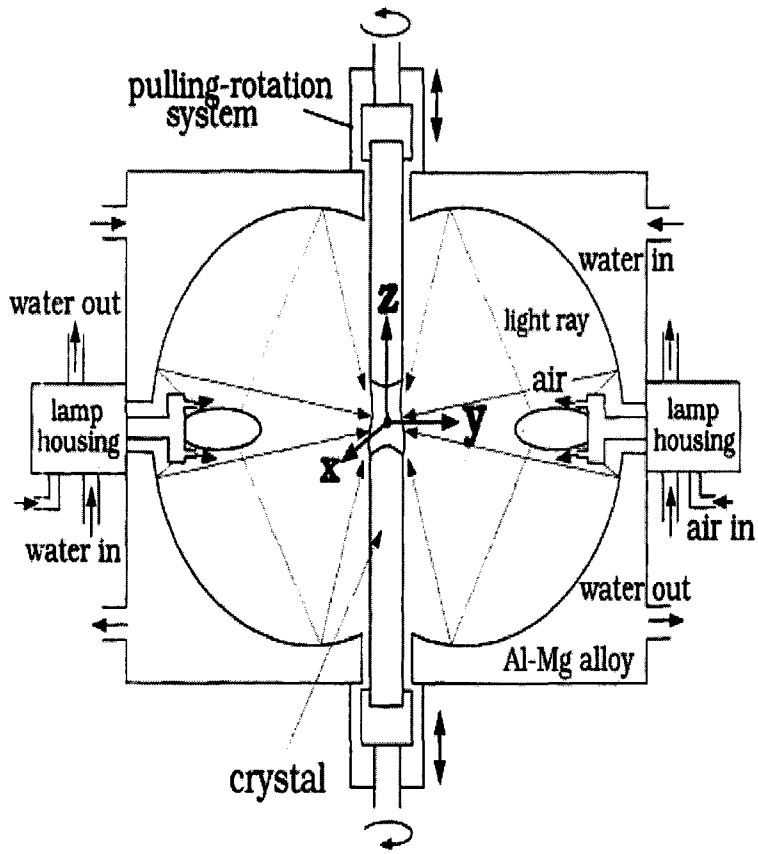

Figure 2.5: Diagram of image furnace of NEC machinery corporation. High quality signgle crystal can be obtained. Taken from NEC image furnace manual.

2.4 Development of Gas Flow Controller

In order to control the gas mixture precisely in the image furnace, a computerized Gas flow controller was developed. The system consist of three parts, MFC (Mass Flow Controller), DAQ (Data Acquisition Board), IBM personal computer with Windows 2000 operating system.

▲ MFC is a type 1179A of MKS instrument and the most important part of the system. Primary performances are determined by the specification of MFC.

▲ DAQ (PCI-6014) of National Instrument is PCI bus type which was inserted into the standard IBM compatible Personal Computer. The DAQ provides 16 input

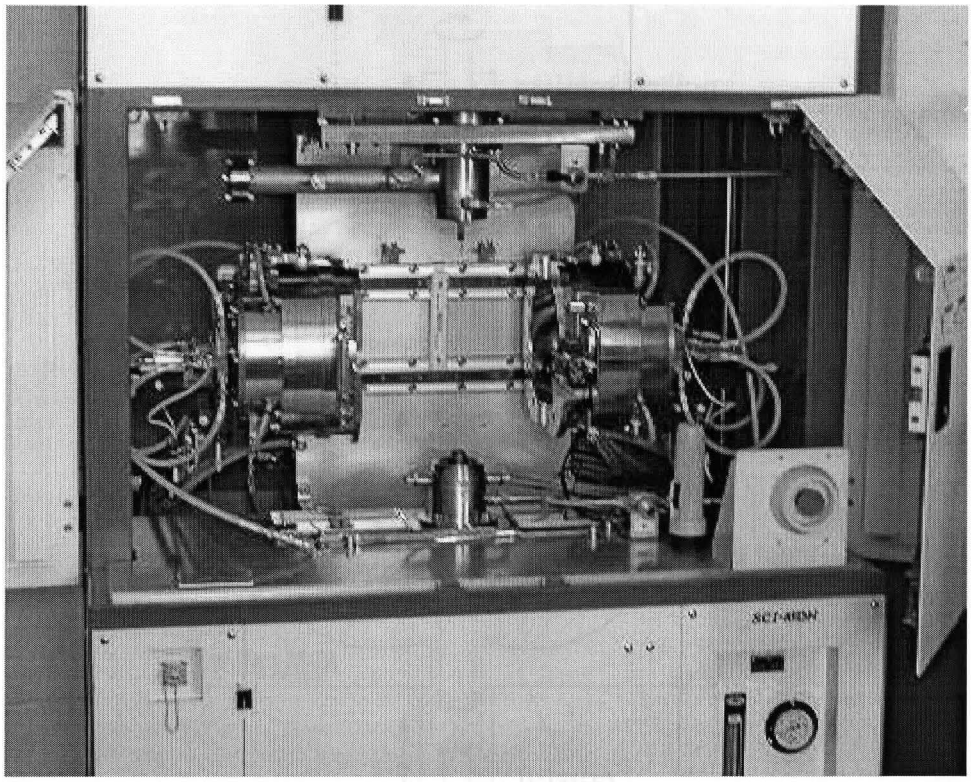

Figure 2.6: NEC image furnace. Computer controls most fuction of the machine. Shiny gold plated hemisphere mirror is opened to detach the quartz chamber in this photo.

channels of 16 bit resolution, 2 analog output channels and 8 On/Off outputs. Although the DAQ (PCI-6014) is cheap and slower than other DAQ, It is appropriate for our application. Because the system does not require high speed input/output channel, 10 Hz of Sampling rate is enough for human and gas control.

▲ LABview from National Instruments was used for programming the control programs operating in MicroSoft Windows 2000. Labview is the most widely used personal computer based control program development tool, and provides a convenient graphical measurement and automation development tools. We have used the system to provide the gas mixture for NEC image crystal growth furnace.

As described in the table (2.2), the system is able to control gas mixture quickly (~2 seconds) and precisely (1% accuracy). The main drawback is that we are not

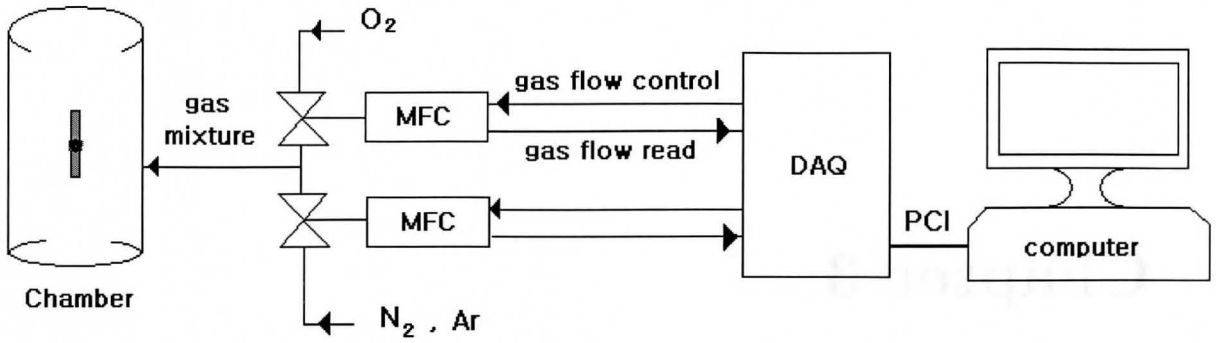

Figure 2.7: Computerized Gas flow controller. DAQ(Data Acquisition Board) generates and DC voltage signal for MFC and samples the MFC gas flow DC voltage signal. MFC(Mass Flow Controller) is a kind of valve and its openness is proportion to input voltage signal.

Table 2.2: Performance specification of Gas flow controller

Accuracy	± 1%
Settling time	<2 seconds
Maximum Inlet pressure	150 PSI
Differential Pressure	10 to 40 PSI
Resolution	0.1 %
Warm up time	2 minutes

able to raise the chamber pressure over 44 PSI[3] due to the specification of the MFC and limitation of only two gas mixture. Nevertheless, the system allow much easier method for providing gas mixtures for single crystal growth than was previously available.

[3]Differential Pressure is referenced to an MFC pressure at atmosphere

Chapter 3

DC and AC Susceptibility

3.1 DC Susceptibility

There are three main categories for magnetic states in materials: paramagnetism, ferromagnetism, and antiferromagnetism. In the absence of an applied field, atomic magnetic moments in paramagnetic materials do not interact strongly enough to cause order and are randomly oriented. The moments then cancel out so that total magnetization is zero. When a field is applied, magnetic moments align in the direction of the field, but thermal energy opposes this and acts to help keep the moments pointed randomly. Therefore, as temperature increases, susceptibility (χ) decreases inversely. If the magnetic moments are strongly interacting, they can spontaneously align parallel or anti-parallel, resulting in ferromagnetism (e.g. permanent magnets) or antiferromagnetism, respectively.

The interaction between moments is governed by **"Heisenberg exchange energy"**:

$$U = -2J\ S_i \cdot S_j\ , \tag{3.1}$$

where J is the exchange constant and S_i, S_j are the values for the moments of the atoms i, j.

Consider the case of a ferromagnetic material, where the exchange constant is positive. At high enough temperatures, thermal energy overcomes the exchange energy, and moments do not align. When the temperature decreases below a certain point, called the Curie temperature, every moment aligns parallel, and the sample achieves a spontaneous magnetization, even though there is no external field. This is a second-order phase transition.

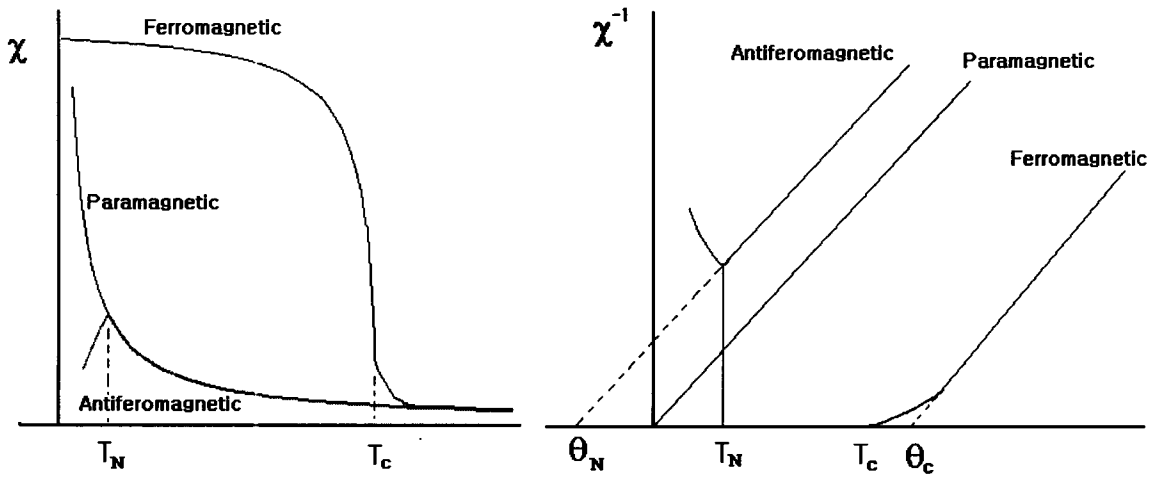

Figure 3.1: The susceptibility and inverse susceptibility for important magnetic behaviors.

If the the exchange constant has a negative value, moments align anti-parallel at what is called the Neel temperature (T_N). Here the total magnetization is zero, but the sample obtains a staggered magnetization in the order state.

$$\chi = \frac{M}{H} \quad [emu/cm^3Oe] \tag{3.2}$$

The magnetic susceptibility(χ) is an important magnetic property. It is defined as the degree of magnetization (M) of a material in response to an applied magnetic field

(H). Scientists often can tell the different magnetic states by measuring susceptibility as a function of temperature.

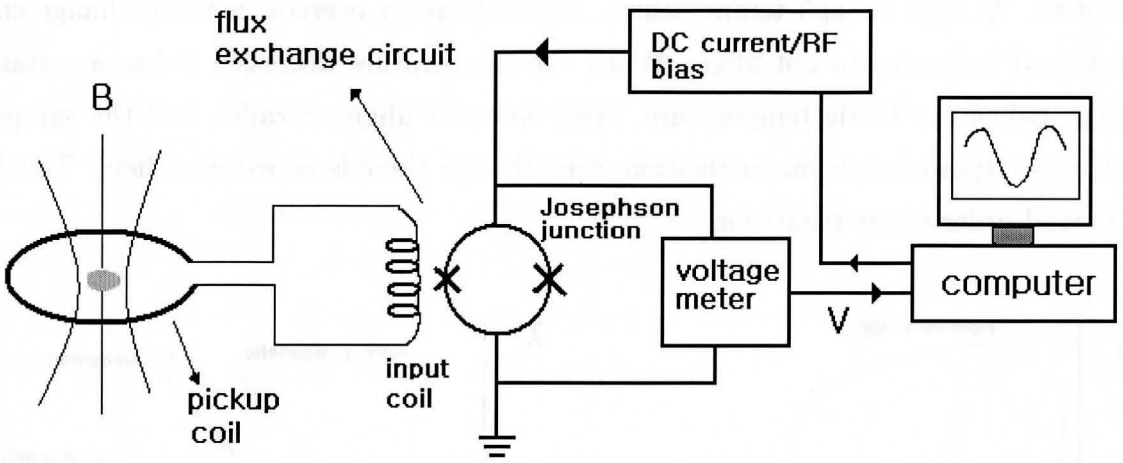

Figure 3.2: SQUID system block diagram

Figure (3.1) shows some typical features of the susceptibility. For ferromagnetic materials, the susceptibility become saturated below the phase transition temperature(T_C). An antiferromagnetic material shows sharp cusps at the phase transition temperature (T_N) while a paramagnetic materials susceptibility show positive linear magnetization with applied field. It is important to remember that the slope of the measured $\frac{1}{\chi}$ curve is proportion to an effective moment.

3.1.1 SQUID

A superconducting Quantum Interference Device (SQUID) is a extremely sensitive magnetic sensor, based on the Josephson junction effect. The flow of electric current, in the form of electron pairs (Cooper pairs), between two superconducting materials that are separated by an extremely thin insulator is termed the Josephson current. The penetration of the insulator by the Cooper pairs is known as Josephson tunneling.

As shown in figure (3.2), an RF-SQUID consists of two Josephson junctions in parallel in which rapidly alternating currents occur within the insulator when enough high DC voltage is applied across the superconductors. A steady flow of current through the insulator can be induced by a steady magnetic field [18].

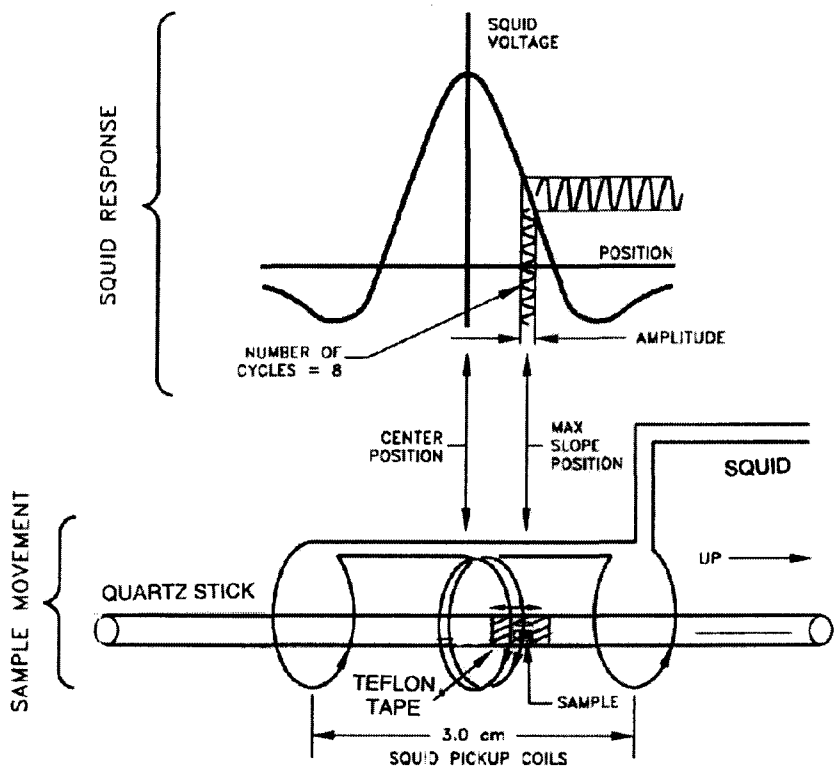

Figure 3.3: Two side coil wound opposite direction to cancel out the applied magnetic filed. Taken from a figure in our Quantum Design user's manual.

Our lab is equipped with a SQUID magnetometer manufactured by Quantum Design Inc. It can measure from 1.8K to 600K with a superconducting magnet ± 5.5 Tesla.

The SQUID system consists of the pickup coil, flux exchange circuit, data acquisition circuit, and control computer. The pickup coil in figure (3.2) are a second derivative configuration with 2.5 cm length. The coil is designed to reject signals from the constant external magnetic fields such as earth field and the applied field from

superconducting magnet. Inductance matching is required for optimum sensitivity in an inductively coupled SQUID detection circuit. The pickup coil inductance must be matched to the inductance of the input coil of the SQUID. The signal detected in the pickup coil is transferred to a voltage meter through the flux exchange circuit which reduces the RF noise.

3.1.2 Curie-Weiss Law

In this section, we will estimate Curie constant from experimentally fitted value and compare it with the theoretical one. The relation between susceptibility and temperature is defined by the Curie-Weiss law[19, 20].

$$\chi = \chi_o + \frac{C}{T - \theta} \tag{3.3}$$

where χ_o is a temperature independent constant, C is the Curie constant, and θ is the Weiss temperature (Weiss constant)

The mean field theory estimates θ as the algebraic sum of all the exchange interaction in the magnetic system[8].

$$\theta = 2S(S+1)/3\kappa_B \sum_{n=1}^{N} Z_n J_n \tag{3.4}$$

where Z_n is the number of n^{th} neighbors of a given moment, J_n is the exchange constant between n^{th} neighbors and N is the number of sets of neighbors for $J_n \neq 0$.

It is worth to remember that a bigger θ correspond to a stronger exchange interaction. In case of many familiar ferromagnetic materials, there is almost zero frustration and long range ordering occurs near $|\theta|$. For such ordering, the frustration factor $\frac{|\theta|}{T_c} \sim 1$, where T_c is critical temperature below which the long range ordering is established. For antiferromagnetic order, the ratio depends on the exact magnetic structure, but typical values for non-frustrated lattices show $\frac{|\theta|}{T_N}$ is in the range of 2 to 5. Frustration is considered to significant when frustration factor $\frac{|\theta|}{T_N} > 10$.

In the $Ho_2Ru_2O_7$ system, however, there are two kind of moments and three interactions of Ru-Ru(strong), Ho-Ho(weak)and Ru-Ho. Whether the above criterion is appropriate or not is unclear for multiple spin systems like $Ho_2Ru_2O_7$.

However, holmium's effective moment is ten times bigger than ruthenium. Therefore holmium spins dominate the DC susceptibility signal. We may roughly consider Weiss temperature(-17.4K) as holmium alone, we take Wiebe's report[17] that holmium show antiferromagnetic order at 1.4K. Then the frustration factor is 12.4.

Theoretical Curie Constant Calculation for $Ho_2Ru_2O_7$

Effective magnetic moment is related to the Curie constant by:

$$\mu_{eff}[\mu_B] = \frac{\sqrt{\frac{3\ \kappa_B\ C}{N_A}}}{\mu_B} = \sqrt{8\ C}\ \ [emu/cm^3Oe] \quad , \tag{3.5}$$

where κ_B is the Boltzman constant, μ_B is the Bohr magneton, and N_A is Avogadro's number.

The effective magnetic moment of a free ion (μ_{eff}) is defined as

$$\mu_{eff} = g\sqrt{J(J+1)} \quad , \tag{3.6}$$

where g is the Lande g-factor for the system, and J is its total angular momentum.

For a free atom the g-factor is given by the Lande equation.

$$g = 1\ +\ \frac{J(J+1) + S(S+1) - L(L+1)}{2J(J+1)} \tag{3.7}$$

The theoretical Curie constant is easily calculated by using equation (3.5) and (3.6). $Ho_2Ru_2O_7$, unlike other spin ices such as $Ho_2Ti_2O_7$, has Ru^{4+} moments contributing the magnetic properties as well as Ho^{3+} magnetic moments. Therefore, the total Curie constant (C_t) is the addition of the Ho^{3+} and Ru^{4+} Curie constant.

$$C_t = 2\ C_{Ho^{3+}}\ +\ 2\ C_{Ru^{4+}} \tag{3.8}$$

where 2 is for number of holmium and ruthenium atoms in the chemical formula.

Ho^{3+} has J = 8, g = 1.25 and Ru^{4+} has S =1, g = 2 because their orbital angular momentum is quenched by the crystal field. Substituting the above values into equation (3.6). Then

$$\mu_{eff}^{Ho} = g\sqrt{J(J+1)} = 1.25\sqrt{8(8+1)} = 10.6\mu_B$$

$$\mu_{eff}^{Ru} = g\sqrt{J(J+1)} = 2\sqrt{1(1+1)} = 2\sqrt{2}\mu_B$$

$C_{Ho^{3+}} = \frac{\mu_B^2}{8} = \frac{10.6^2}{8} = 14.05$

$C_{Ru^{4+}} = \frac{\mu_B^2}{8} = \frac{(2\sqrt{2})^2}{8} = 1$

Therefore holmium contributes around 95% of the system's susceptibility. Substituting this into (3.5):

Introducing these results into (3.8), we can get the theoretical Curie constant of the $Ho_2Ru_2O_7$ system:

$C_t \sim 2 \times 14.05 + 2 \times 1 = 30.10$ [emu/cm^3 Oe]

DC susceptibility data fit for C, χ_0, θ

One can obtain the Curie constant (C), temperature independent part (χ_0), Weiss temperature (θ) by fitting the experimental DC susceptibility data with Curie-Weiss law. Our SQUID system's temperature range is 2K to 600K. For 310K $\sim$ 600K range, we need to install the heating device (oven) to the sample chamber.

We performed a χ measurement in two experiments(one from 2K to 350K and another from 310K to 600K). Then I combined two data sets. We fit the susceptibility data to extract fitting parameters (χ_0, C, θ) by MatheMatica from 200 K to 600K which is well higher than the Ru ordering temperature, The fitting function is the equation (3.3).

The Weiss temperature fitted to -17.4K, which is larger than the report (-4K) of Bansal et al [16]. The Curie constant fitted to 29.61 [emu/cm^3 Oe] which is quite close to the theoretical estimation of 30.10 [emu/cm^{3}Oe]. The temperature independent constant consisting of diamagnetic and Van Vleck term is 0.001778 [emu/cm^{3}Oe].

However, fits with a (200K $\sim$ 350K) temperature range, we fit -5K for Curie temperature (similar to -4K of Bansal) and 0.005 for Van Vleck term. This likely indicates that Bansal's temperature fit range was too low to extract the accurate Curie-Weiss behaviors.

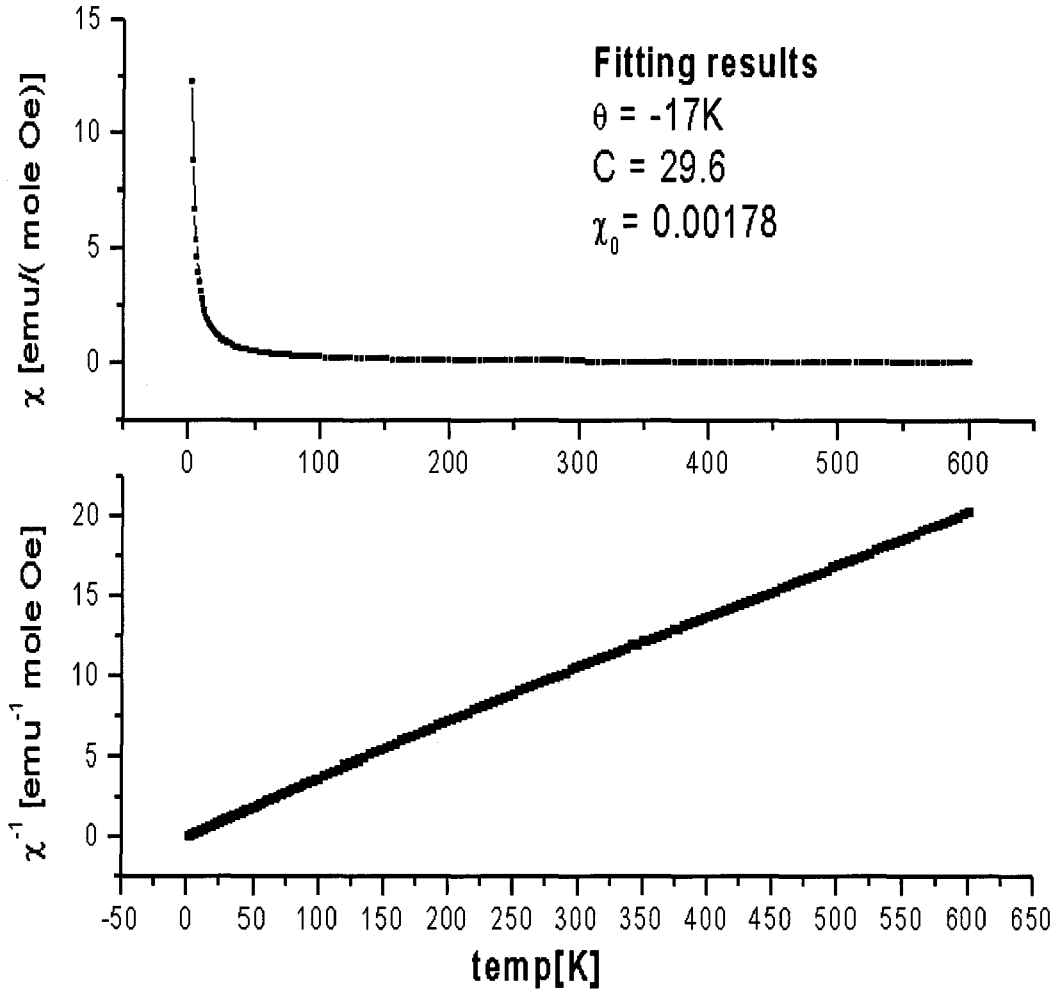

Figure 3.4: DC susceptibility data from SQUID. Curie-Weiss temperature θ is estimated to be -17 K

3.1.3 Field Cooled (FC) and Zero Field (ZFC) Cooled Irreversibility

In the known spin ice systems, $Ho_2Ti_2O_7$, $Ho_2Sn_2O_7$, and $Dy_2Ti_2O_7$, the transition metal ions do not have a moment. However, the rare earth ion Holmium (Ho)

and the transition metal ion ruthenium (Ru) are both magnetic in the $Ho_2Ru_2O_7$ system.

$Ho_2Ru_2O_7$ susceptibility data, shown in figure (3.5) show a small irreversibility below 95 K. This is a typical spin glass characteristic. But as mention by Ito, it is also associated with of ruthenium magnetic moment's antiferromagnetic ordering and can be regarded as an almost long-range ordered state [21].

It is worthwhile to notice that χ continue to rise below 95K. it is reasonable to think that smaller moment system (ruthenium) is ordered or freezing at the temperature therefore the remaining response to the applied field is coming from the holmium moments. The measured susceptibility of the $Y_2Ru_2O_7$, which has magnetic contribution from Ru moments only, has two orders of magnitude less susceptibility[21].

This 95K divergence agrees with the specific heat data which will be discussed in chapter 4. Ito *et al.* also reported that irreversibility were observed at the temperatures of the specific heat jumps in $Y_2Ru_2O_7$, $Nd_2Ru_2O_7$ [21]. The $R_2Ru_2O_7$ pyrochlore (R=rare earth) showed specific heat jump in the temperature range 75K $\sim$ 160K which was correlated with the rare earth ion size. Neutron scattering studies also reported antiferromagnetic ordering at the temperature range. Moreover, the negative Weiss temperature (-17.4K) indicates the antiferromagnetic exchange. Although most susceptibility comes from holmium moments, it is difficult to conclude the type of exchange between the ruthenium moments.

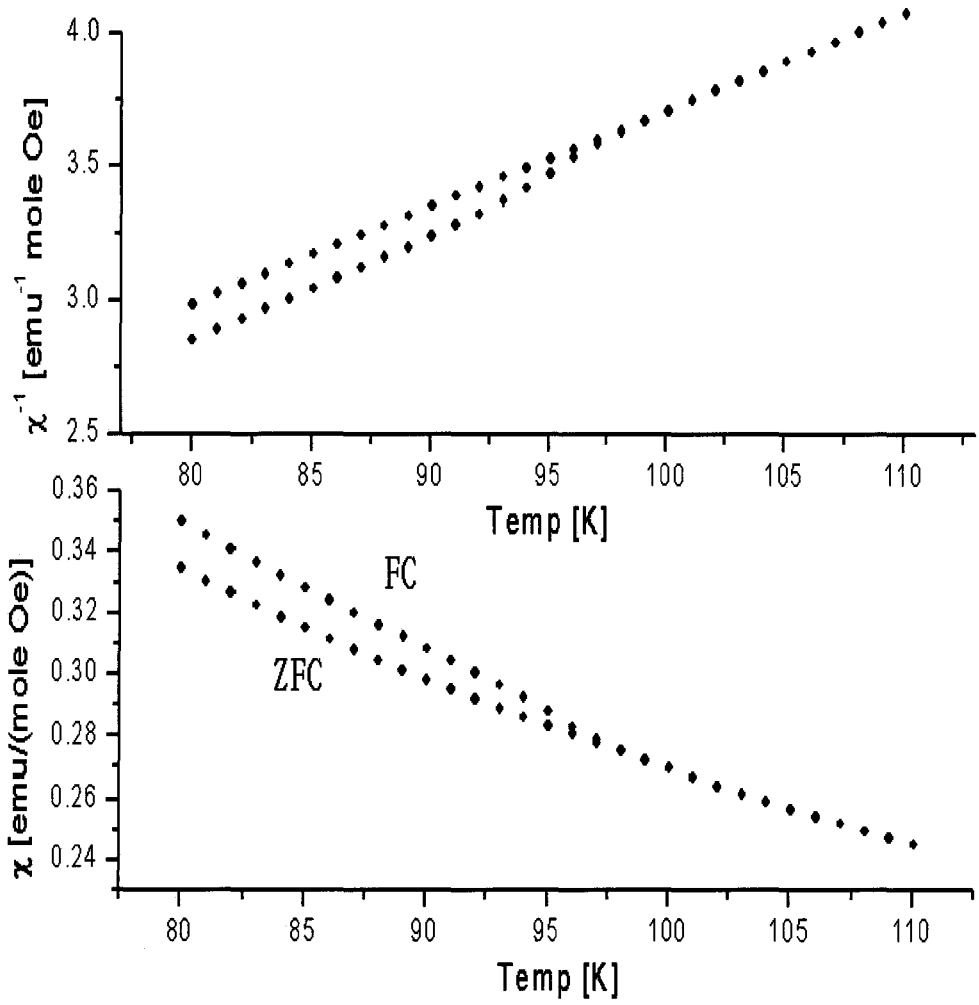

Figure 3.5: Field cooled and zero field cooled susceptibility with 100 Oe. Irreversibility occurs at 95K. $Nd_2Ru_2O_7$ shows same behavior. Given its small moment of ruthenium compare to holmium is associated with the irreversibility.

3.2 AC susceptibility

AC susceptibility experiments measure the susceptibility of materials and are relatively simple technique for measuring magnetic properties. Unlike DC susceptibility

measurements which the sample is under a constant field, AC susceptibility measurements apply a alternating field (0.1 $\sim$ 10 kHz) [1]. It is now used extensively to study spin glass phenomena, superconducting transitions, vortex dynamics and critical current densities. Basically AC susceptibility is based on the electric principle of Faraday induction law.

$$\varepsilon = -\frac{\partial \phi_B}{\partial t} = -\frac{\partial}{\partial t}\int_S B \cdot da \quad (MKS\ unit) \tag{3.9}$$

where ϕ_B = magnetic flux.

The above Faraday induction equation means that if time varying magnetic field is passed through electric a wire coil, then an electric motive force (voltage) is induced. In summary, a time-varying magnetic field is applied to a sample, the sample is magnetized and sensing coils detect the AC magnetic field of the sample's magnetization. Because applied AC magnetic field is canceled out by a compensation coil, one gets only information from the sample. The simplified diagram of AC susceptibility measurement system is shown in figure (3.6).

Driving coils generate small AC magnetic field (normally less than 10 Oe) which is applied to the sample. Some experiments might apply strong DC magnetic field on top of AC magnetic field (DC magnetic coil is not shown in this diagram). To increase the signal amplitude, it is good idea to measure bigger mass samples and apply appropriately high field as long as samples have linear response.

AC susceptibility is different from other magnetometers such as the vibrating sample method (VSM) and SQUID, which the sample is under constant(or very slowly changing) magnetic field. That is, one can change the frequency of AC applied magnetic field up to $\sim$20 KHz.

At higher frequencies, the AC moment of the sample often does not follow along the DC magnetization curve due to dynamic effects in the sample. The phase delay of magnetization is shown in figure (3.7). Comparing to mechanics, a high frequency

[1] μSR frequency range is $10^4 \sim 10^9$ MHz and neutron is $10^8 \sim 10^{12}$ MHz

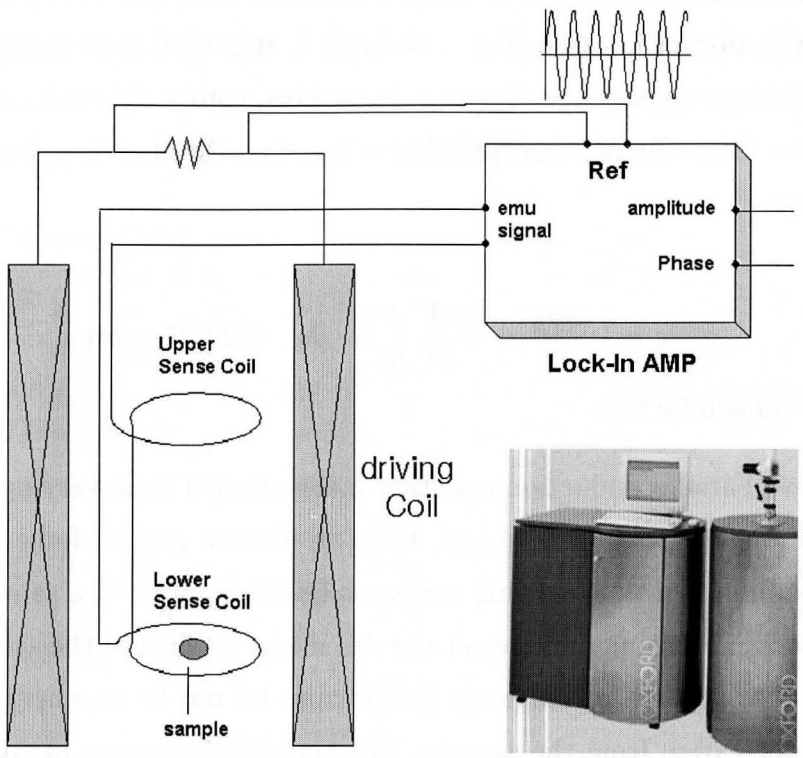

Figure 3.6: AC susceptibility measurement system. Upper and lower coil is wounded opposite direction so that it can eliminate the signal of AC Driving coil. Therefore one can extract only the signal of sample's magnetic moment. Lock-In Amplifier is very sensitive instrument to pick up the precisely same signal having reference signal which is the frequency of AC magnetic field. Same Oxford magnetic properties probe can be used for both DC and AC susceptibility measurement.

AC driving magnetic field is analogous to sinusoidal mechanical force and inertia of spin, friction prevent spins from change direction fast enough to AC magnetic field. Therefore, magnetization lags behind the applied AC magnetic field.

AC susceptibility may be used to determine the phase transition. Normally second order transition (magnetic transition) often displays a peak in χ'. On the other hand, first order transition shows broad change of χ' slope.

AC susceptibility provides valuable dynamic magnetization information as well as static information. Although a low frequency AC field experiment reduces the signal

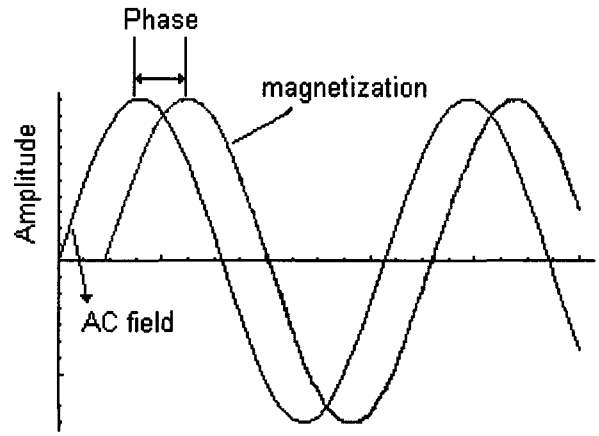

Figure 3.7: AC susceptibility signal. $\chi_{AC} = \chi' + i\,\chi''$. χ' is the amplitude of magnetization. χ'' is phase lag and a measure of how how fast the spin can respond from the oscillating magnetic field. One can make an analogy of χ' (dispersion) to resistance and χ'' to capacitance (absorbtion) of the electrical system.

amplitude and therefore increase the measurement time, its result is almost same as that of DC magnetometers. This valuable experiment probe of the spin dynamics of materials is the consequence of one's ability to change the frequency of AC driving magnetic field.

3.2.1 AC susceptibility data analysis

Frustrated system shows similar AC susceptibility behavior to spin-glass which displays unique AC susceptibility signatures. The AC susceptibility measurement is particularly important for spin-glass, because the freezing temperatures are difficult to measure with other experimental technique such as specific heat measurement. In a spin-glass, magnetic spins are frozen randomly below the freezing temperature, and the system is paramagnetic above this temperature. First known spin-glass systems are dilute alloys of paramagnets or ferromagnets in nonmagnetic noble metals, $Cu_{1-x}Mn_x$.

It was in the early 1970s that sharp cusps were discovered in the AC susceptibility

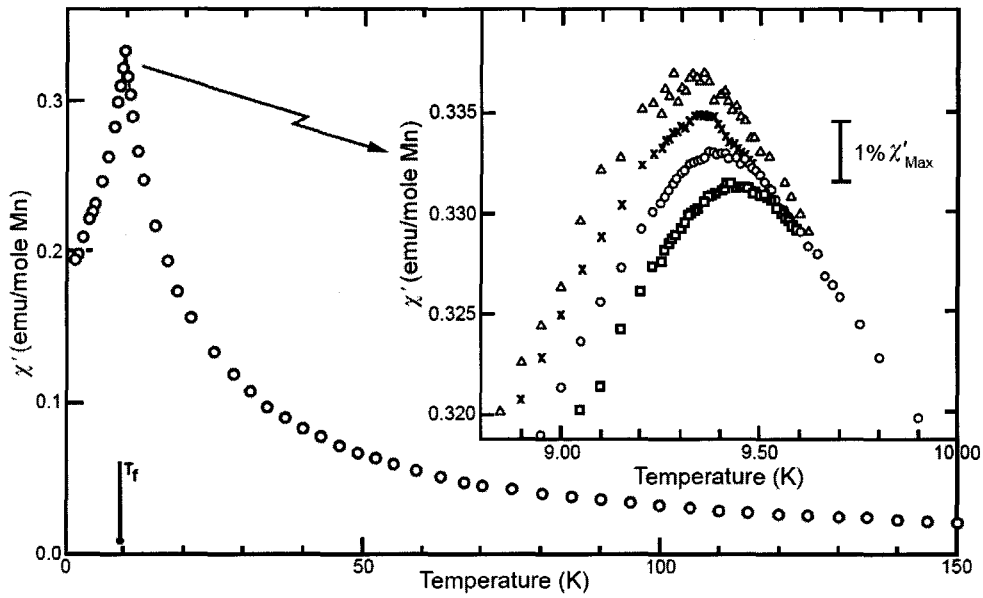

Figure 3.8: AC susceptibility as a function of temperature for $CuMn(0.9\% of Mn)$ showing the cusp at the freezing temperature (T_f). This shape of cusp is similar to that of the typical long range antiferromagnetic susceptibility measurement. The inset shows the frequency dependence of the cusp from 2.6 Hz (triangles) to 1.33 kHz (squares) [23].

of $CuMn$. Figure (3.8) is the AC susceptibility data as a function of temperature for $CuMn$ (0.9% of Mn). The freezing temperature is determined by measuring χ' vs. temperature curve which reveals a cusp at the freezing temperature. It is important and unique signature that peak temperature is getting higher and peak amplitude is shifted downward with deceasing the magnetic field frequency.

Figure (3.9) is AC susceptibility data with various frequency (from 20Hz to 10KHz) for $Ho_2Ru_2O_7$. Measurement data below 20Hz was quite noisy and is not shown. The AC susceptibility shows a typical spin glass feature which is the freezing temperature (T_f) shift with magnetic field frequency. The 3 dimensional AC susceptibility of χ' and χ'' are shown in figure (3.11) and (3.2.1).

The cusp (T_f) of χ' shows a significant frequency dependence and is shifted to higher temperature with increasing magnetic frequency. The amplitude of χ' decreases

with increasing frequency below 3K but shows frequency independence above 5K. Since there is normally no frequency dependent in paramagnetic regime, the frequency dependent indicate that there is a significant slow down of spin fluctuation below 3K.

There is strong frequency dynamics of χ', χ'' for 1.4K < T < 3K, indicating that there still spin fluctuation in that frequency range.

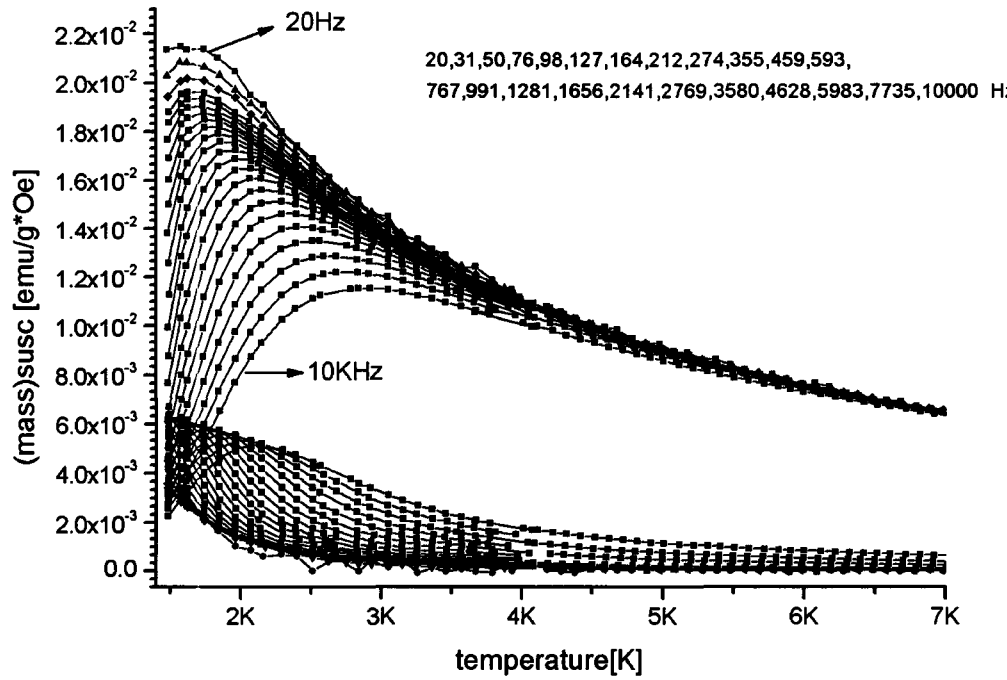

Figure 3.9: AC susceptibility with various frequency(from 20Hz to 10KHz) show a strong frequency dependency both χ'(upper lines), χ''(lower lines). This display the frequency dependency which is a typical signature of spin glass state or frustrated system.

In order to get the T_f shift with frequency quantitatively, we defined the following equation :

$$\beta = \Delta T_f \; / \; [T_f^L \; (\Delta(Log\; \omega_H) - \Delta(Log\; \omega_L)] \tag{3.10}$$

Where β is the T_f shift per decade of measuring frequency, ΔT_f is the temperature

difference between lower and higher T_f, T_f^L is the cusp temperature at lower frequency, and ω_H is the higher measuring frequency, ω_L is the lower measuring frequency (Hz).

$Ho_2Ru_2O_7$'s T_f shift between 20Hz and 10000Hz is

$$\beta = (2.9 - 1.6)/(1.6\ (Log10000 - Log20)) = 0.25$$

Table (3.1) is the T_f shift for various materials. The measured value 0.25 is similar to that of superparamagnet[2]. The canonical spin glasses have quite little cusp shift compare to spin-glass-like materials. This cusp shift in T_f offers a good criterion for distinguishing canonical spin glasses from a superparamagnet.

Table 3.1: Frequency dependence of T_f for various materials

	system	β
Spin glass	CuMn(0.9% of Mn)	0.0050
	AuMn	0.0045
Superparamagnetism	$(LaGd)Al_2$	0.06
	$a(Ho_2O_3)(B_2O_3)$	0.28
	$Ho_2Ru_2O_7$	0.25

In order to analyze the frequency shift of cusp better, we used the **Arrhnius** law.

$$\omega = \omega_0 \exp[\frac{-E_a}{K_B\ T_f}] \qquad or \qquad ln(\frac{\omega}{\omega_0}) = -\frac{E_a}{K_B}\frac{1}{T_f} \tag{3.11}$$

Where E_a is a activation energy, K_B is a Boltzman constant, ω ia the measuring frequency (or $1/\omega$ is called as the relaxation time), ω_0 is the characteristic frequency (or $1/\omega_0$ is defined as the characteristic relaxation time), T_f is the maximum susceptibility temperature.

Figure (3.10) shows the frequency dependence of T_f and display two different regimes (high frequency/high temperature, low frequency/low temperature) with a temperature crossover at ~1.8K. We fitted both regime to Arrhnius law.

[2]superparamagnet($a - (Ho_2O_3)(B_2O_3)$) has a very small ferromagnetic phase grain (1~10 nm). Thermal energy disturbs the direction of the nano-size grains, superparamagnet display the similar behavior to paramagnetism even at temperature below T_C, T_N

E_a and ω_0 were extracted 17K, 4 MHz in the high temperature regime and 32K, 17 GHz in the low temperature regime.

For the canonical spin glass, $CuMn$, fitting to the Arrhenius law gives $\omega_0 \sim$ 100 MHz, $E_a = 10$K. Spin ice $Ho_2Sn_2O_7$ and $Ho_2Ti_2O_7$ have 19.6K and 27.5K of activation energy barrier respectively [24]. The E_a, ω_0 of the low temperature regime are similar to the spin ice.

However, Unlike canonical spin ice, there are a crossover between the two regime in our system. This aspect probably reflect that a simple Arrhnius law is too crude to describe the spin dynamics of $Ho_2Sn_2O_7$.

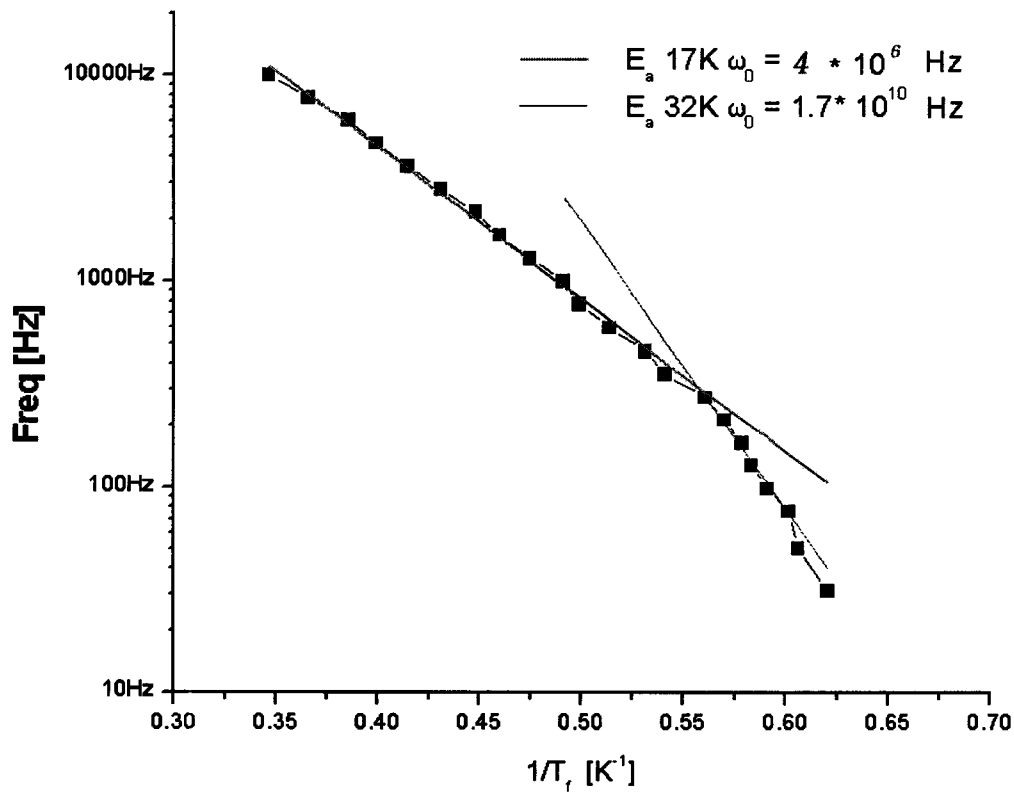

Figure 3.10: Maximum susceptibility temperature (T_f) changes with frequency. The magnetic relaxation time ($1/\omega$) exponentially increases with decreasing temperature. There are two linear regime. Above 0.55(red line) activation energy and characteristic frequency fit to 32K, 1.7×10^{10}Hz which is similar to that of spin ice.

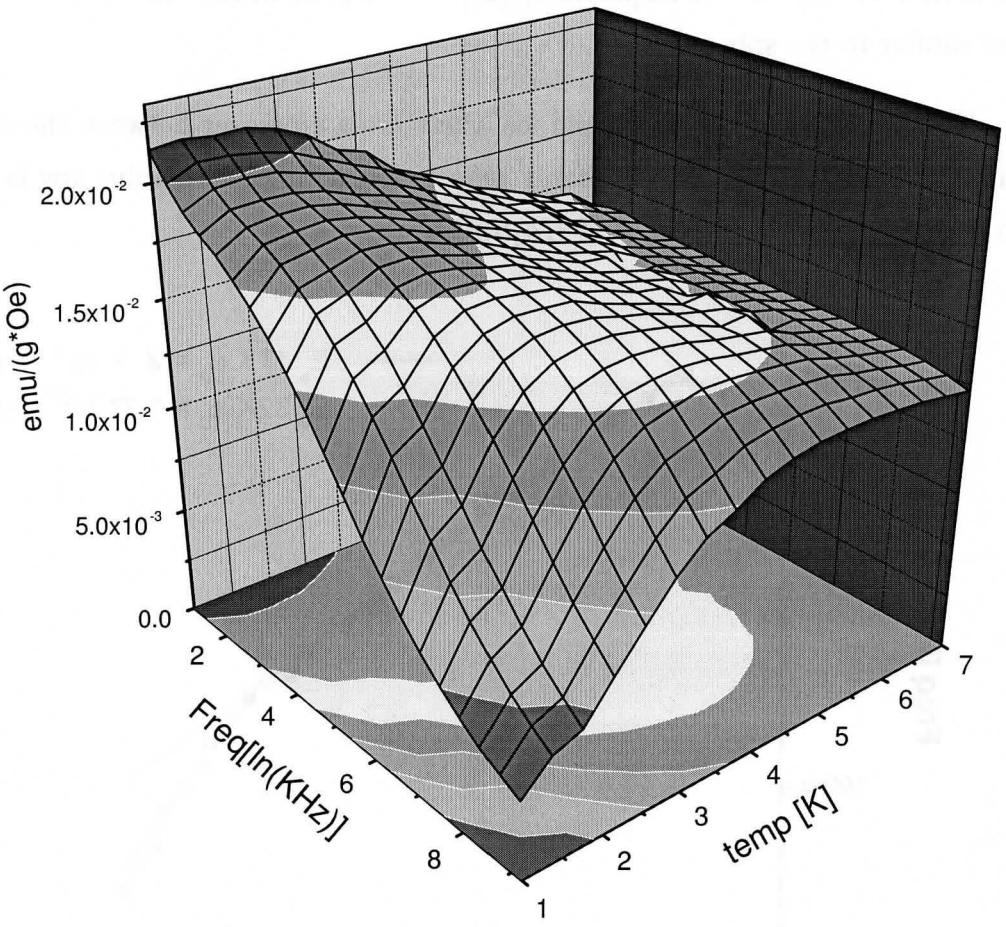

Figure 3.11: 3 dimensional AC susceptibility of χ'. Above 5K there is little frequency dependence of T_f. Below 3K, however, there is a significant frequency dependence of T_f.

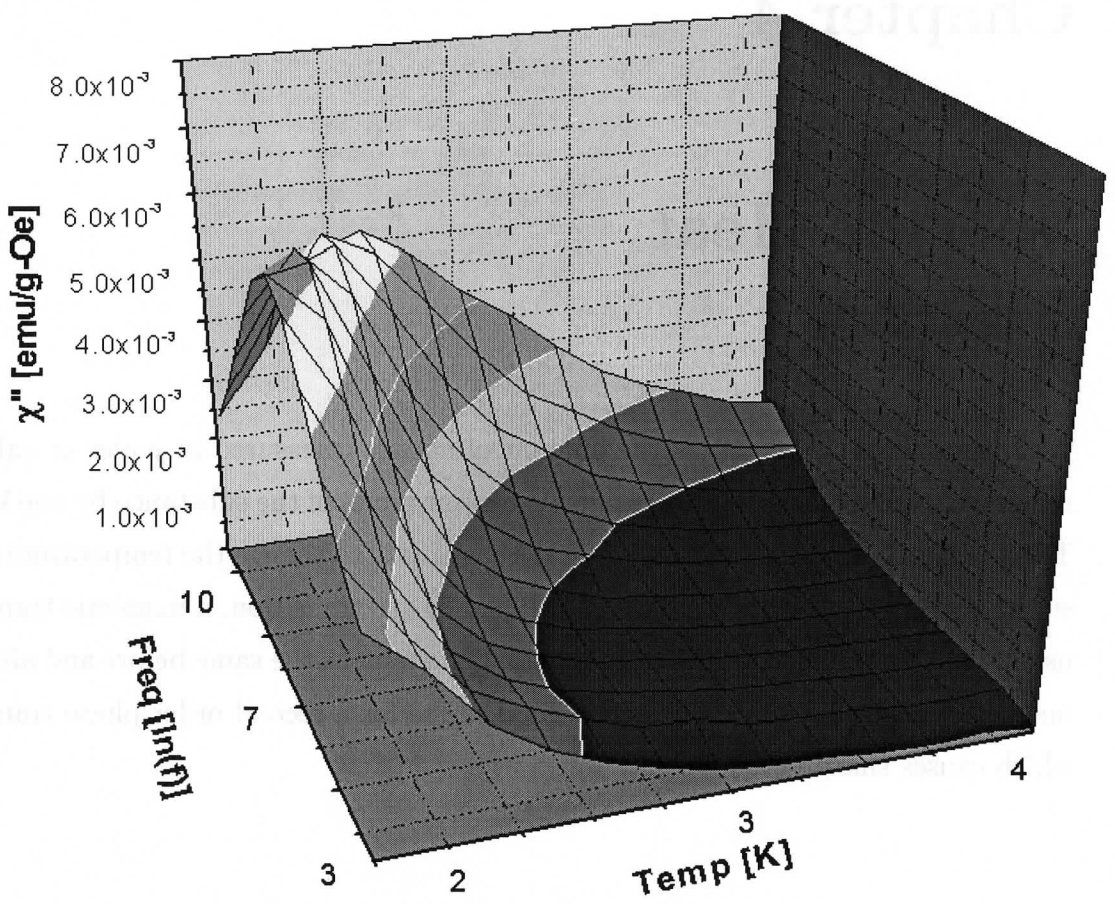

Figure 3.12: 3 dimensional AC susceptibility of χ''

Chapter 4

Specific Heat

Specific heat is defined as the amount of energy (measured in joules or calories) required to raise the temperature of one gram(or mole) of the substance by one kelvin. The smaller the specific heat capacity, the easier it is to change the temperature of the substance and vice-versa. Unlike solid, liquid or gas transition, a magnetic transition usually has no visible changes. A magnetic system looks the same before and after the magnetic ordering. Specific heat is a good probe for a second order phase transition which causes sharp lambda shape jump.

$$C = \frac{\Delta Q}{\Delta T} \tag{4.1}$$

where C is the specific heat, ΔQ is the applied energy, ΔT is temperature change.

In a solid material, the heat capacity is the sum of several different sources such as the lattice (phonon), electron, and magnetic contribution. Figure (5.1) is the molar specific heat of a typical solid as a function of temperature. Materials tend to have their unique specific heat pattern[25].

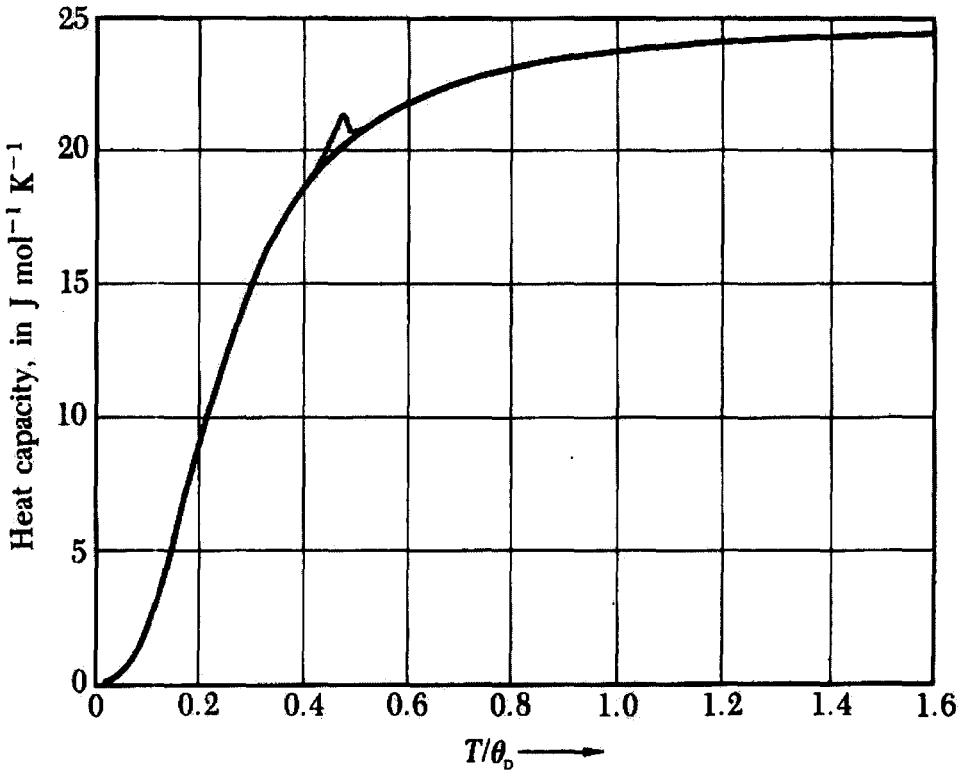

Figure 4.1: Heat capacity of typical solid as calculated by the Debye approximation. The horizontal scale is normalized to the Debye temperature. The saturation of the specific heat value at the high temperature is 3R $\cong$ 25 Joule/(mol K) or 6 cal/(mole K). The red spike drawn on the black line is a typical second order transition signature of magnetic materials. Figure taken from [26]

4.1 The Oxford Microcalorimeter

The calorimeter is the device used to measure thermal properties such as specific heat, latent heat, etc. The basic principle of calorimeter is **Conservation of energy** which *James Joule(1818-1889)* first discovered.

$$Q_{cold} = -Q_{hot} \tag{4.2}$$

The energy leaving the hot area of the system by heat(or work) is equal to that entering the cold area of the system for an isolated system. We can think of heat

as an energy transfer across the boundary of the system caused by a temperature difference between the system and its surrounding. The quantum mechanical concept of heat is a phonon gas in the lattice.

Historically, the first technique for measuring specific heat is heating sample T_x , placing it in a vessel contains liquid such as water of known mass and temperature($T_{liqud} < T_x$) then measuring temperature of the liquid of the equilibrium. However, the accurate measurement of the specific heat C [joule/K -gram] at an elevated temperatures is a difficult and tedious process if the ordinary calorimetric methods are used. Moreover there is limitation of conducting wide range of temperature measurement and large sample is required to get accurate measurement.

The use of the ohmic pulse heating in measurements of the specific heat was first described by deLapp in 1929 and modifications were subsequently exploited by others. In these methods, a sample is rapidly heated through a heater pad while the electric current passing through the heater is measured simultaneously. This technique is known as the semi-adiabatic heat pulse or the time-constant or relaxation method. A sample platform is suspended in vacuum for minimum heat loss to the surrounding atmosphere. After electrical heat, the chip temperature will decay exponentially toward the new higher level according to

$$T \cong T_1 + \Delta T_o\Big(1 - \exp(-t/\tau)\Big) \tag{4.3}$$

where T_1 is the initail temperature and $T_1 + \Delta T_o$ is the final equilibrium temperature.

If $\Delta T = T - T_1$ in time t, we get an alternative equation as

$$\Delta T(t) \cong \Delta T_o\Big(1 - \exp(-t/\tau)\Big) \tag{4.4}$$

The time evolution response of the chip temperature and heating energy is shown in figure (4.2)

It is convenient to remember that the time constant is the amount of time to reach around ~70 % of the saturation temperature. Analogous to the electrical law

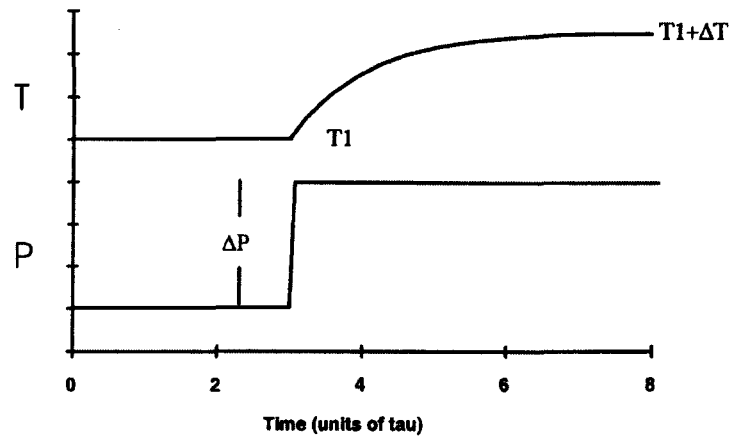

Figure 4.2: Heating power and temperature response of the sample

of serial circuit containing a resistor and capacitor, it is the product of the thermal resistance (R_{TH}) and total heat capacity (C) including the sample, sapphire substrate and thermometer etc.

$\tau = R_{TH}\ C$

Substitute the thermal resistance $R_{TH} = \frac{\Delta T_o}{\Delta P}$ into the time constant equation, one can get equation (4.5) for the specific heat.

$$C = \frac{\tau}{R_{TH}} \tag{4.5}$$

The instrument measures the supplied heat energy $\Delta P = (I^2 R_{heater})$ and τ, then obtains the specific heat.

4.2 Sample Preparation and Mounting

Sample preparation and mounting of the sample for the specific heat measurement is a tricky job. This is because samples are tiny (around 10mg) and the sample

platform is suspended by very fragile thin tungsten wires. Figure (4.3) shows the sample holder of specific heat measurement system.

Sample preparation

Samples should be prepared into a thin and small rectangular shape to be placed on the sapphire platform. Samples size are typically $3 \times 2 \times 1mm$, and they should have a thin and even flat surface to conduct heat quickly. A emery based sand paper has been used to grind the sample surface. After final grinding, I clean the surface with Kimwipes and trichlorethane. One should be careful about using Emery based sand paper because it contains Fe_3O_4 a highly ferrimagnetic material. Aluminium oxide based sand paper is preferable for magnetic sample grinding. Samples masses were around 10 mg.

Sample mounting on the sample holder

The sample is placed on the fragile sample platform. The contact between sample and platform should have low thermal resistance and enough mechanical adhesion. At first Wakefield grease was used to provide thermal contact between sample and platform, but Wakefield grease did not provide enough adhesive force on somewhat porous ceramic samples and we found that the sample tended to fall off easily during measurements[31]. Apiezon N grease as an alternative thermal compound was tried and found to provide good adhesion. The sample holder is then inserted to heat capacity probe. A turbo vacuum pump was used to evacuate air($\sim 10^{-7}torr$) from the probe to minimize the heat loss of sample to surrounding air. Then the heat capacity probe is inserted into the cryostat.

4.3 Measurement of $Ho_2Ru_2O_7$ Sample

Figure (4.4) displays the specific heat data of a $Ho_2Ru_2O_7$ ceramic sample. We had some difficulties conducting the measurement. First, the signal was noisy as temperature increased. Second, needle valve leak caused a ice build-up and the jamming

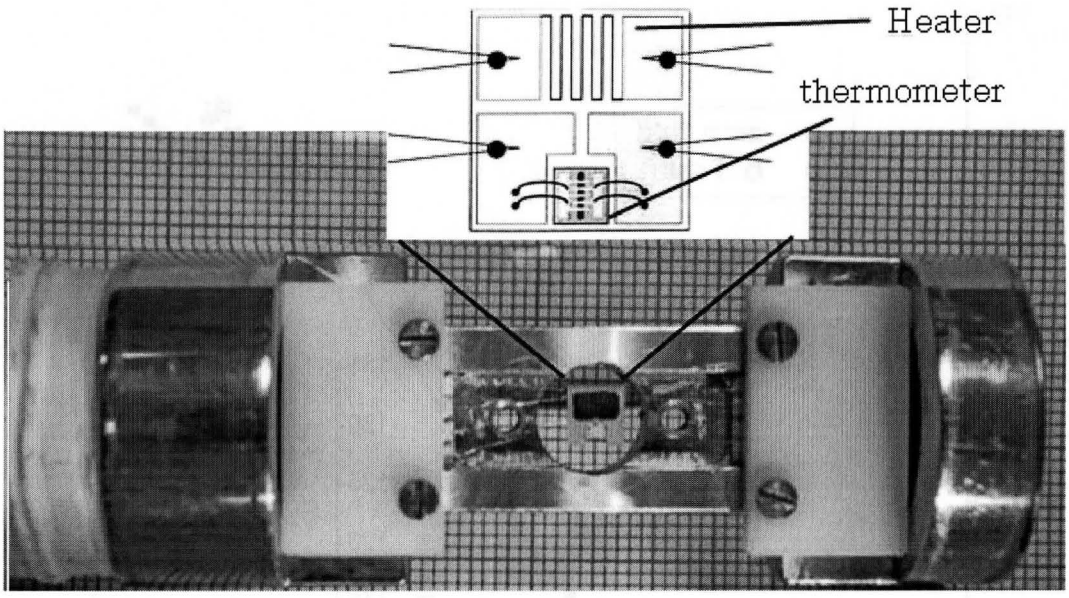

Figure 4.3: Calorimeter sample holder. The inset shows the microcalorimeter chip, which is suspended by 20μm gold plated tungsten leads. It consist of a sapphire platform on which a thin metallic film heater (zig-zag pattern) is masked and the cernox thermometer. The sample (dark object of bottom picture) is placed on top of the heater

of the valve motor. We developed an external heater to prevent ice-build-up and reduce the possibility of needle valve problems.

The instrument was set for fine temperature steps around 95K for the transition behavior. Specific heat data is shown in figure (4.4) and exhibits a sharp jump around 95K, which is in good agreement with the temperature of irreversibility of field cooled and zero field cooled susceptibility. As discussed in previous chapter, the jump is due to the antiferromagnetic ordering of ruthenium moments.

This second order-like transition is observed for other ruthenium pyrochlore systems such as $R_2Ru_2O_7$ (R is rare earth elements)[21, 22]. Neutron Rietveld analysis have elucidated that long range antiferromagnetic order of ruthenium spins form below the specific anomaly. Lattice distortion does not participate in the transition and ruthenium spins magnetic ordering is the only cause of the transition.

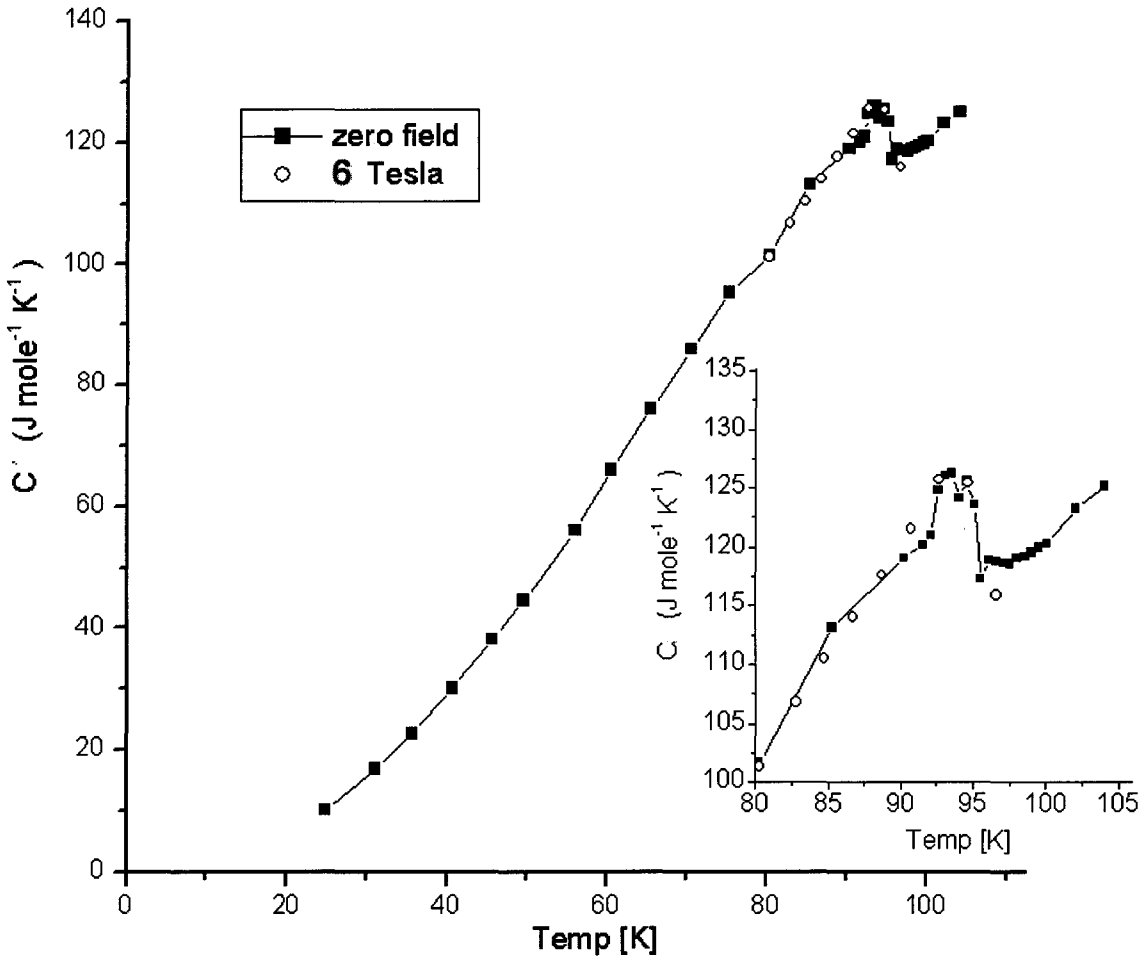

Figure 4.4: Specific Heat measurement display a lambda anomaly at 95K due to ruthenium antiferromagnetic transition. The inset expands around the transition temperature.

Ito *et al*[21] have measured all the $R_2Ru_2O_7$ pyrochlore system showing a specific heat jump in the temperature range 75-160K. The specific heat jump temperature increased with atomic radius(r) of the rare earth elements R^{3+}. It can be explained by considering that, as *Lee et al.*[27] pointed out, the transfer energy(t)[1] of the 4d electrons between the nearest neighboring ruthenium ions increases as r increases by calculating electronic band structure. Since the exchange interaction increases as t increases, specific heat jump temperature is naturally expected to increase as r

[1] 2 × band gap energy

increases, if the transition is primarily driven by a magnetic origin.

An attempt to isolate the lattice contribution to the specific heat was made. We applied a high magnetic field during the specific heat measurement. An applied field could make magnetic spins along the field, and then eliminate the entropy due to magnetic spins. As shown in figure 4.4 we found that a 6 Tesla magnetic field made no discernible difference to C_p data. Therefore the exchange field of the ruthenium moments must be much larger than 6 Tesla.

4.4 Estimation of Magnetic Specific Heat and Debye Temperature

The total specific heat is the sum of the electron, phonon and magnetic spin contribution. $C_{lattice}$ consist of the conduction electron contribution $C_{electron}$ and the phonon contribution[28].

$$C_{total} = C_{lattice} + C_{magnetic} = C_{electron} + C_{phonon} + C_{magnetic} \tag{4.6}$$

A theoretical equation of C_{phonon} was established by Dutch scientist Debye. The electronic term is added then

$$C_{electronic+phonon} = \gamma T + 9NR\,(\frac{T}{\theta_d})^3 \int_0^{\frac{\theta_d}{T}} \frac{x^4 e^x}{(e^x-1)^2} dx \tag{4.7}$$

where γ is the Sommerfeld coefficient, $x = \hbar\omega_d/k_BT = \theta_d/T$, θ_d is the Debye temperature, N = the number of atoms per formula unit.

The equation (4.7) of specific heat of solid material can be expressed in a somewhat simpler equation at low temperatures($T < \frac{\theta_{debye}}{10}$).

$$C_{low} = \gamma T + \beta T^3 \tag{4.8}$$

where γ is related to the free electron density of state(DOS). β is due to phonon, and related to the Debye temperature.

For an insulator, γ is expected to be much smaller($\cong 0$) than a conductor. Spin glasses often show a linear temperature dependence of the specific heat which is due to the macroscopic degeneracy of magnetic ground states.

The magnetic entropy S_m is obtained by integrating C_m/T over an appropriate temperature range.

$$S_m = \int_0^T \frac{C_m}{T} dT \tag{4.9}$$

This magnetic molar entropy is expected to be same with the theoretical value $S = Rln(2J + 1)$, where J is the total magnetic moment.

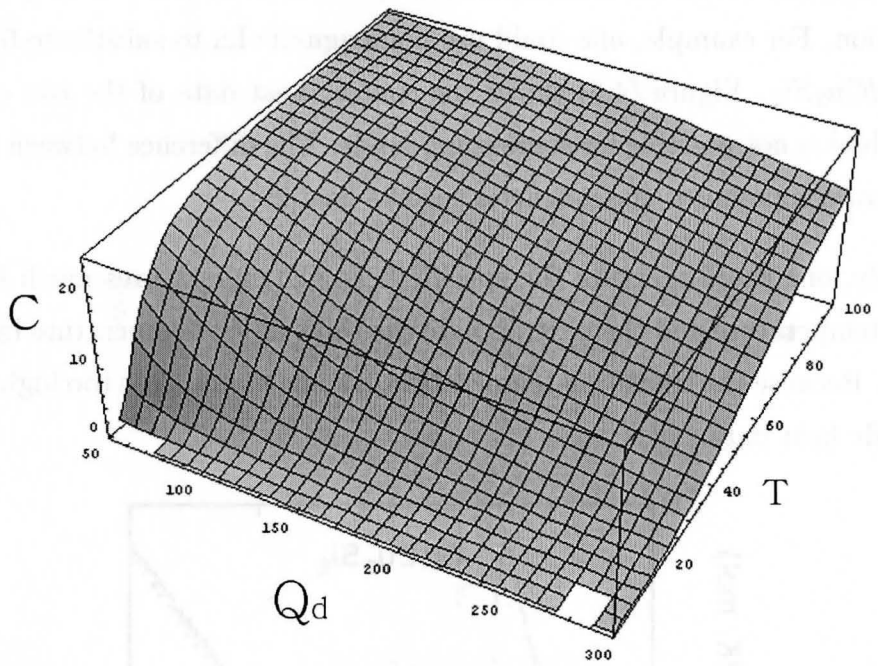

Figure 4.5: Simulation of the Debye equation(specific heat($joule/(moleK)$ with varying θ_d and temperature). At high temperatures, molar specific heat of elements approaches the maximum value of 25. Some compounds have a higher maximum multiplied by N

There are difficulties evaluating the magnetic contribution. The specific heat that we actually measure is the total sum of the magnetic, electronic and lattice contributions. Moreover N is not applicable for some complicated compounds. That is, N could be determined by high temperature(well beyond the Debye temperature) of specific heat values.

There are several methods to isolate the magnetic specific heat C_{mag} from C_{total}.

The first method is to apply a high magnetic field sufficient to align the spins above magnetic transition temperature. This eliminates magnetic spins entropy and provide pure lattice contribution. This method could not be used if the available magnetic field is not strong to fully order spins in the system. The difference between field and non-field specific heat is the magnetic contribution

Secondly, one could use isomorphous nonmagnetic compounds to get the lattice contribution. For example, one could use nonmagnetic La to substitute for magnetic Gd in $GdCu_2Si_2$. Figure (4.6) shows the specific heat data of the two compounds. This method is not possible for some compounds. The difference between the specific heat of two compound is the magnetic specific heat[29].

Thirdly, one could measure the specific heat at temperatures much higher than ordering temperature,and then extrapolate the value at low temperature by the Debye equation. Because the transition temperature of some materials is too high to measure the specific heat data.

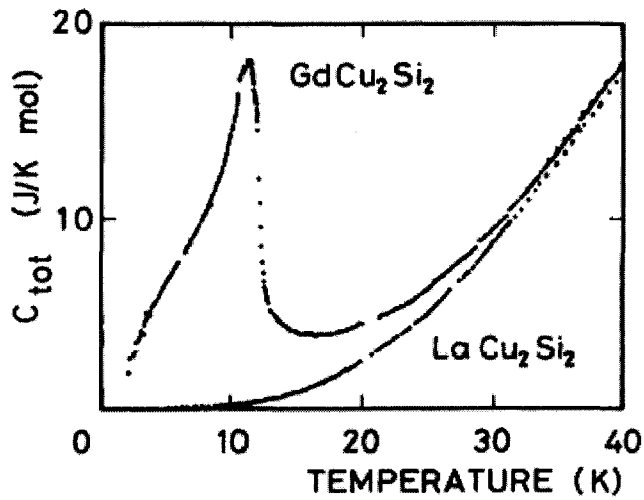

Figure 4.6: Specific heat measurement of $GdCu_2Si_2$ *and* $LaCu_2Si_2$(La is nonmagnetic). The $LaCu_2Si_2$ curve should be normalized by correction factor which is related to molar mass of compound. In this case, the correction is not much because molar mass of Gd and La are similar

Extraction of Debye temperature and magnetic Entropy

In order to extract the magnetic component of the total specific heat, we tried to use the first method but as mentioned above 6 Tesla is not enough to wash out ruthenium moment entropy over 95K. Therefore we have used third method.

Since we could not measure enough high temperature data, data fitting could have some error. We also safely assumed that the empirical parameter N of Debye equation is 11 (the number of atoms in $Ho_2Ru_2O_7$). The data slope well above the ruthenium ordering transition temperature is only due to the lattice component. Therefore it should be same with that of Debye equation. In other words, the specific heat data above ruthenium transition temperature should fit to the Debye equation. Unfortunately data points above ruthenium transition(95K$\sim$104K) is not enough for accurate fit. Figure (4.7) is the result of fitting. A Debye temperature $\theta_d \cong 441$K is obtained.

We also estimate the Debye temperature by another way. If we look at figure (4.6), the magnetic specific heat arise before the transition. This mean that we can get Debye temperature by matching Debye curve to the highest point of experimental specific heat data. In this way, Debye temperature $\theta_d \cong 450$K is obtained which is not much different thanour above estimate.

It is worthwhile to compare the measured magnetic entropy(S_m) with theoretical one. In order to do that we need to extract the magnetic contribution from the experiment data. The magnetic component of specific heat (C_m) of figure (4.8) can be extracted by subtracting the lattice component from total specific heat of experiment data in figure (4.7).

Then one can calculate the magnetic entropy due to magnetic spins with equation (4.9). As seen in figure (4.8), the integration range for experimental data is 25K to 104K. The calculated entropy for the range is 18.9 [J/mole K].

Our minimum temperature is 25K in this plot which is not enough low to fit for the low temperature specific heat law (equation 5.10). In order to get the entropy

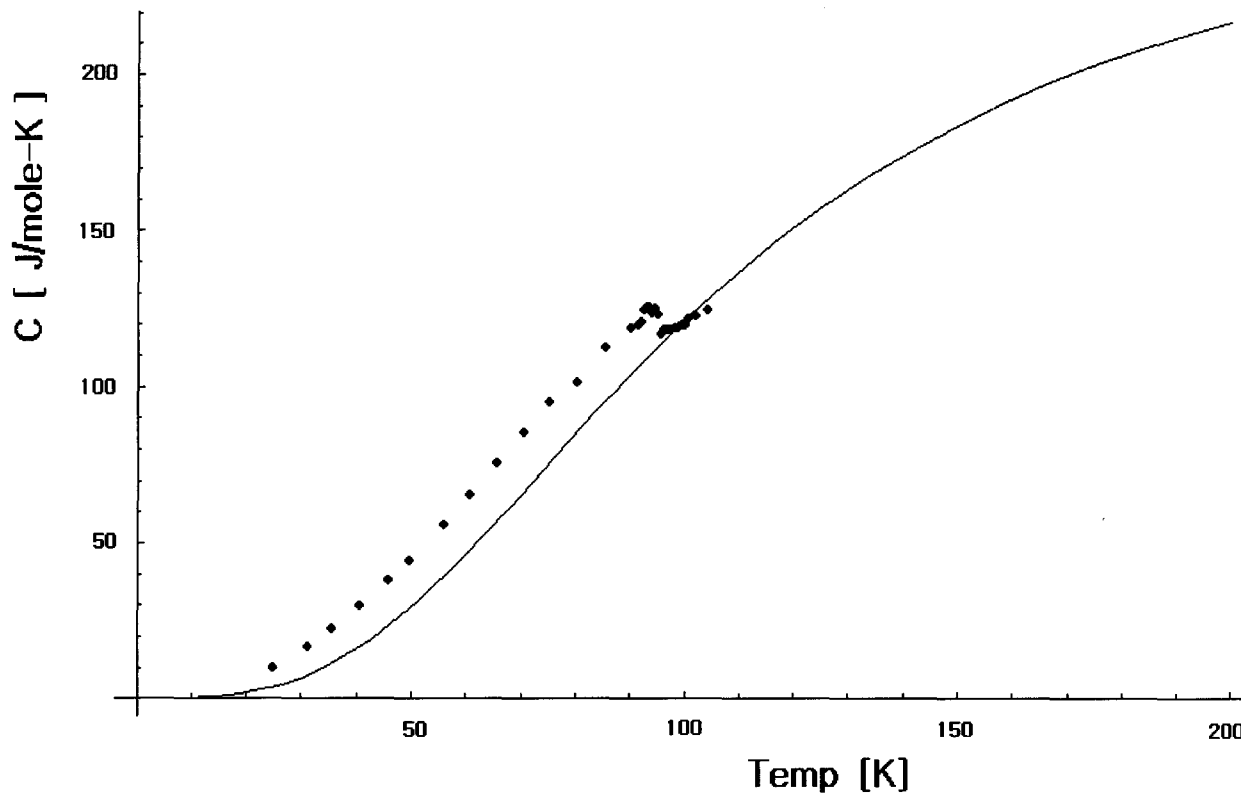

Figure 4.7: Specific Heat measurement for $Ho_2Ru_2O_7$. Solid line is fitting from Debye equation and dotted line is experimental data(20K - 104K). Solid line is lattice component by Debye equation. Specific heat anomaly at 95K due to ruthenium antiferromagnetic transition

associated with below 25K, we tried T^2 and T^3 extrapolation, which are calculated to 3.1, 2.7 [J/mole K]. So it does not lead a little difference which extrapolation we choose. The experimental magnetic entropy is ~22 [joule/(mole-K)].

Theoretical magnetic entropy is $S = R\ ln(2J+1)$, where J is the total magnetic moment.

Ru : $2 \times R\ ln(2J+1) = 2 \times 8.3 \times ln\ 3 = 18$ [joule/(mole-K)]

Ho : $2 \times R\ ln(2J+1) = 2 \times 8.3 \times ln\ 17 = 47$ [joule/(mole-K)]

Theoretical entropy = Ru entropy + Ho entropy = 65 [joule/(mole-K)]

As our experimental magnetic entropy ($\sim$ 22 [joule/(mole-K)]) is 22 % higher than theoretical ruthenium one. This likely indicate that some holmium entropy contributes as well.

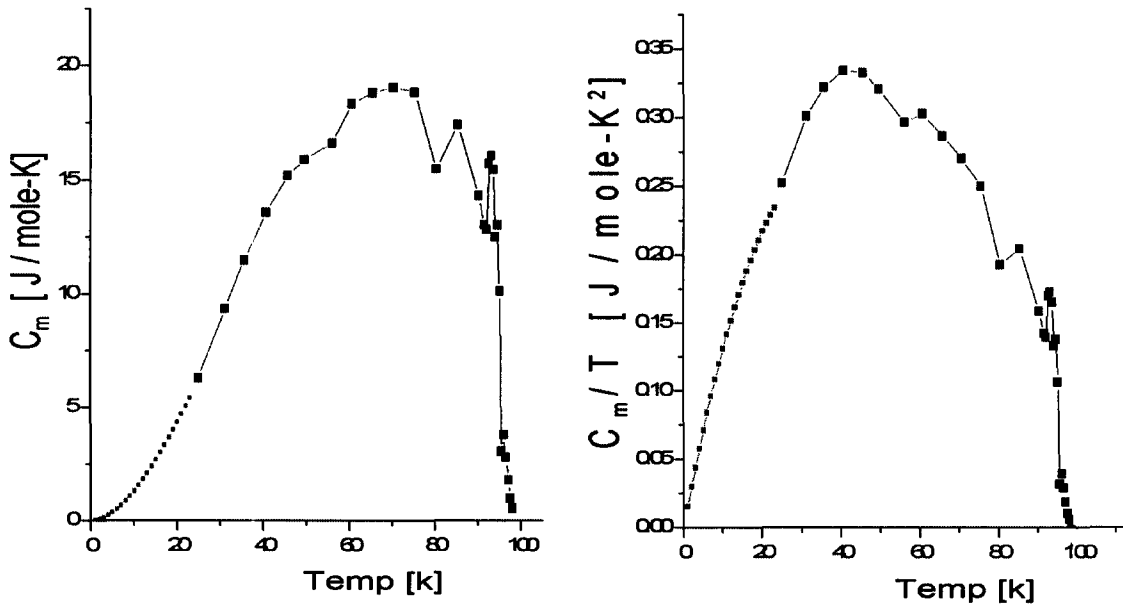

Figure 4.8: Magnetic specific Heat component of $Ho_2Ru_2O_7$ calculated by subtracting the lattice component. One can obtain entropy due to magnetic by calculating the area below C_m. Black symbols are experiments data and Red symbols are extrapolation data.

For canonical spin glasses such as $CuMn$, C_m display broad maximum above $T_f(T_{max} \sim 1.5\ T_f)$ and gradual fall off at increasing temperature. Unfortunately since lower temperature limit of our specific heat measurement is 25K, it is difficult to compare $Ho_2Ru_2O_7$'s data with canonical spin glasses' around freezing temperature.

The fitting is performed by Mathematica, the details are in the Appendix.

Chapter 5

Muon Spin Relaxation; μSR

Muon Spin Relaxation (μSR) detects the distribution and dynamic characteristics of magnetic fields within a sample. In this technique, radioactive muon particles are implanted in a sample and the ejected positrons pattern is used to reveal the magnetic properties of the sample. μSR is a valuable experimental tool for the study of superconductors, semiconductors, and magnetic materials.

5.1 Brief History of μSR

The muon was discovered in 1937 by American physicists S.H. Erlenmeyer and C. D. Anderson (and simultaneously by J. C. Street and E. C. Stevedore) in a cloud chamber during a cosmic-ray experiment. The discovery was published as "New Evidence for the Existence of a Particle Intermediate Between the Proton and Electron" [34] . Before this point, the fundamental particles were presumed to be electrons, protons and the then newly discovered neutrons. This new elementary particle was called the "mu meson".

In 1935, the existence of a particle of about the same mass had been predicted by Japanese physicist Yugawa. However, the muon's behavior did not conform to that

of Yugawa's meson theory (which actually describes the pion, discovered more than 10 years later), and the muon is now classed as part of the lepton family rather than as a meson.

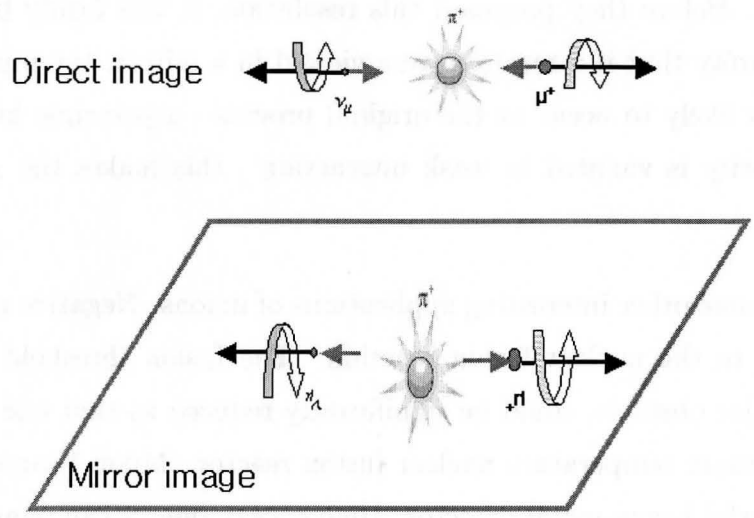

Figure 5.1: Parity violation. Initially a positive pion with a zero spin, has a zero angular momentum and zero linear momentum. Then the pion decay to a positive muon and a muon neutrino in opposite directions with equal and opposite momentum. Parity conversion (or mirror conversion) flip the spin direction, not momentum. Orange and black arrows display spin and momentum respectively. Mirror image reaction could not be observed because muon neutrino always have the opposite direction of momentum and spin which is called left-hander. On the other hand, muon could be either left-hander(same direction of spin and momentum) or right-hander(opposite direction of spin and momentum).

The muons are a second generation lepton (non-nuclear particles). They can be produced by the weak decay of pions into a muon and a muon neutrino. Muons which we use for μSR have an electric charge of $+e$ and an average lifetime of 2.197 μS. Neutrinos are the electrically neutral partner of the muon. Muon neutrinos, like electron neutrinos, have a extremely small mass, but apparently non-zero. Determining the neutrino mass is of great current interest.

Scientists quickly tried to find ways to use muons for application. The first use

as probes of magnetism in matter was reported by Rasetti in 1944[35]. However, a attempt was not successful until the revolution in theoretical physics. In 1956 and 1957, T.D. Lee and C.N. Yang predicted that any process governed by the weak nuclear interaction might not have a corresponding "mirror image" process of equal probability[36]. Before they proposed this resolution, it was firmly believed by the physics community that if a reaction were viewed in a mirror, the mirror image was a priori just as likely to occur as the original process - a principle known as parity symmetry. Parity is violated in weak interaction , this makes the μSR technique possible.

There are some other interesting applications of muons. Negative muon (μ^-) acts like a catalyst in the nuclear fusion reaction. The fusion threshold energy, which has been a major obstacle, could be significantly reduced so that one could create a very compact room temperature nuclear fusion reactor. Muon beams could also be used as a powerful heavy metal detector. High energy muons can penetrate shipping containers to detect nuclear materials such things as uranium.

5.2 Creation of Muon and Positron

Elementary particles such as muons, pions are created by striking high-speed ionized hydrogen ions (protons) against a low atomic number target such as carbon or beryllium.

5.2.1 Pion

Particle physicists explained the behavior of the strong nuclear force by introducing another type of elementary particle, called a pion. Protons and neutrons interact in the nucleus by exchanging pions. Exchanging pions pulls protons and neutrons together.

Table 5.1: Summary of pion and muon characteristics

charge state	π^o	π^-	π^+	μ^+	e^+
mean life(sec)	8.9×10^{-15}	2.6×10^{-8}	2.6×10^{-8}	2.2×10^{-6}	stable
spin	0	0	0	1/2	1/2
mass(Mev/c^2)	135	139.5	139.5	105 MeV	0.5 Mev

Pions in the nucleus exist only for the briefest instant of time, no more than 10^{-23} seconds, but even during their short existence they can provide the attraction that holds the nucleus together. Pions can also exist as independent particles outside of the nucleus of an atom. Free pions also live for a short period of time (about 26 ns) and then decay into a muon and a neutrino. At TRIUMF, pions are produced by a 500 MeV proton beam with a carbon or beryllium target. To obtain an optimum number of single pions, the incident protons should have energies in the range of 500 MeV to 1000 MeV.

Pion creation processes

$p + n \rightarrow p + p + \pi^o, \qquad p + n \rightarrow p + p + \pi^-, \qquad p + n \rightarrow n + n + \pi^+$

Pion decay processes

$\pi^o \rightarrow \gamma + \gamma, \qquad \pi^- \rightarrow \mu^- + \bar{\nu}_\mu, \qquad \pi^+ \rightarrow \mu^+ + \nu_\mu$

where π , p , n, μ, ν_μ, and $\bar{\nu}_\mu$ are pion, proton , neutron, muon, muon neutrino, and anti muon neutrino respectively.

5.2.2 Positive Muon (μ^+)

Most positive muon beams at μSR facilites are generated from pions decaying at rest in the surface layer of the production target, These muons are called surface muons and have the remarkable property that all the muons have the same energy and a spin polarization directed opposite to their linear momentum. These properties are the result of conservation of linear and angular momentum with parity violation in the pion decay. A surface muon has momentum about 29.8 Mev/c. The muons

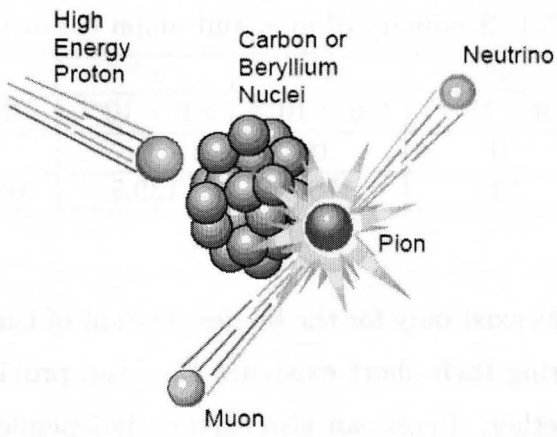

Figure 5.2: Pion is created after proton hit target and it decay into muon and neutrino. The mirror-image reaction(parity symmetry) never occurs in nature. The parity inversion performed by the mirror changes a left-handed neutrino to a right-handed one, which the weak interaction cannot produce. This is called parity violation. Taken from [39]

are collimated and directed onto a sample. The muon penetration depth depends on its energy. Since all the muons have the same energy, all are embedded in the sample to about the same depth (roughly 0.1 millimeter). For most experiments it is not important to know the penetration depth exactly. We can consider that measurement of 0.1 millimeter depth shows the bulk characteristic of the sample.

Since muons are charged particles, they can be directed by magnetic and electric fields. Quadropole magnets are used for focusing the muon beam while dipole bending magnet are used to select a desired muon momentum. The muon beamline consists of quadropole magnets and dipole bending magnets to collect and transmit muons efficiently.

5.2.3 Negative Muon (μ^-)

Looking at above three the decay processes, π^o decay does not produce muons and negative pions stopping in the production target are almost always captured in the

nuclei before they have a chance to decay. This problem is overcome by allowing the pions to decay in flight within a long superconducting solenoid. The muons that are emitted opposite to the direction of the pion momentum are called *backward muons*, which can be selectively extracted by a bending magnet. While this method can also be used for μ^+SR, for μ^-SR there is no alternative. Compared to surface muon beams, decay muon beams have higher momentum (approximately 50-100 MeV/c), a larger momentum spread and much larger phase space (and therefore lower luminosity). While the two latter features are less desirable, decay muons are the only means of studying samples contained in a thick target vessel. Such vessels are used in studies of gases or liquids and studies of high-pressure effects.

5.2.4 Positive Muon (μ^+) Decay to Positron

A positive muon has an radioactive lifetime of 2.2 μs. After that point, a neutrino-antineutrino pair and a positron will be created. Figure (5.3) display the positron decay. If both neutrino are emitted with their linear momentum in the same direction, this will lead a maximum energy positron (52.8 MeV). The decayed positrons are distributed around the muon spin direction according to the probability function.

$$W(\theta, a) = 1 + a \ \cos(\theta) \tag{5.1}$$

where the factor 'a' depends on the positron energy.

In the figure 5.3, the polar graph axis is probability density and area of each closed curve should be 1. If all decay positron's energy is 52.8 MeV, asymmetry is 1 and experiment time could be minimized. In reality, decay positron muons' energy are in between 0 MeV and 52.8 MeV. In order to reduce the experiment time, one has to maximize the ratio of higher energy muons. In the experiments, a 'degrader' is often inserted between the sample and detector to absorb the low energy positrons.

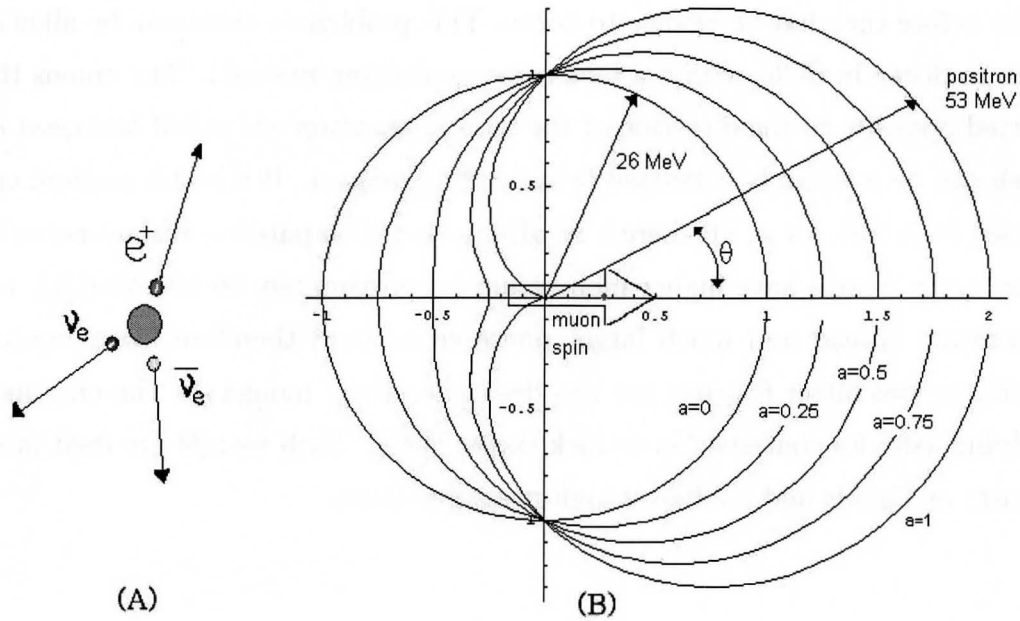

Figure 5.3: Muon decay into positron and positron's angular distribution. Angular distribution of positrons probability density of muon decay. Simulated by Mathematica.

5.2.5 μSR Facilities

The muon beams currently available for μSR are distinguishable by their time structure.

Continuous Wave(CW)[39]

The CW facilities deliver a nearly continuous source of protons that are used to produce muons. The great advantage of this type of muon beam is that the time resolution of the μSR can be made quite small ($\sim$100 ps) with an appropriate choice of detectors and electronic detection scheme. Better time resolution allows detection of larger magnetic fields and fast relaxing signals. On the other hand, the muon-stopping rate is limited by the muon lifetime, because consecutive muon decay events must be rejected over a time interval of many muon lifetimes to avoid ambiguity in relating a decay positron to its parent muon; that situation is called as 'pileup'. In the CW μSR

technique, each individual 'unpiled-up' muon and its decay positron are individually counted. However, recent innovations in detector design (called MULTI) that make more efficient use of the available muons are rapidly reducing the constraints imposed by the maximum muon-stopping rate at CW sources[38].

Pulsed Beam

The Pulsed beam facilities direct intense bunched proton pulses produced from a synchrotron or linear accelerator onto the muon production target. The pulse structure of the primary surface muon beam reflects the pulse structure of the proton beam, but with the pulses further smeared out by the pion lifetime. A general requirement of the μSR technique at a pulsed muon source is that the time width of the muon pulse must be considerably shorter than the muon lifetime, while the pulse repetition period must be longer than the muon lifetime. The width of the muon pulse limits the time resolution, because all the muons in a given pulse are counted together, although the muons do not arrive simultaneously. Because the pulse widths are on the order of 10$\sim$ 100ns, a pulsed beam cannot compete with a CW beam in providing information on fast muon relaxation rates and cannot be used to measure precession in large magnetic fields. The advantages of a pulsed muon beam are that in principle one can use the entire incoming muon intensity and there is almost no background in the μSR signal due to accidental coincidences between the incoming muons and decay positrons. The virtual absence of background related to contamination of the beam with particles other than muons allows detection of muon decay events beyond 10 muon lifetimes ($> 22\mu S$) which CW beam does not. A pulsed muon source is also ideally suited for resonance studies, since an RF field and/or light illumination can be synchronized with the muon pulses.

Ultra-Low Energy Muons for Surface Science

While conventional surface muon beams can be used to investigate rather small samples, there is a desire for still lower energy muons that can be stopped near sample surfaces, in thin films and near multi-layer interfaces. A number of ingenious methods have been used in attempts to produce 'ultra-slow' muon beams, however

Table 5.2: Muon facilities around world

Name	Country	type	Intensity (muons/$cm^3 - sec$)
TRIUMF	Canada	cyclotron	$\sim 2 \times 10^6$ (continuous)
PSI	Switzerland	synchrocyclotron	$\sim 3 \times 10^7$ (continuous)
LAMPF	US	Linac	$\sim 1 \times 10^6$ (pulse)
RAL	U.K.	synchrotron	$\sim 1 \times 10^6$ (pulse)
KEK	Japan	synchrotron	$\sim 3 \times 10^6$ (pulse)

the successful approach has been simple moderation in a thin degrader consisting of a condensed van der Waals gas (Ar or N_2). Fortunately, the 'moderated muons' remain highly polarized. At the PSI muon facility moderated positive muon beams with tunable energies in the range of 0.5 to 30 KeV are produced. This energy range corresponds to implantation depths in solids of less than a nanometer to several hundred nanometers which is very useful in surface science. One drawback of the moderation method is that the intensity of the ultra-low energy muon beam emerging from the downstream side of the moderator is reduced several orders of magnitude below that of the incident surface muon beam. Nevertheless, ultra-low energy muons have the potential to revolutionize μSR, having recently demonstrated their applicability to investigations of surfaces and thin-film samples by addressing some longstanding issues in condensed matter physics. Their recent arrival means that researchers can use the μSR technique as a tool to directly compare information on magnetic phenomena observed near the surface to that observed in the bulk of the same sample.

5.3 Basic μSR Experiment Setup

Muon Spin Rotation/Relaxation/Resonance(μSR) is an experimental technique used to study condensed matter through the magnetic interaction of muon spins with their environment. The principle is similar to Nuclear Magnetic Resonance(NMR), and Electron Spin Resonance(ESR) but there are several advantages over these conventional techniques.

- It can be applied to virtually any specimen
- It covers the time scale from 1ns through some tens of ms (filling the gap between neutron scattering and NMR)
- It is sensitive to very small moments, like 0.01 Bohr magneton. Moreover, it is complementary to neutron diffraction in the sense that it can be used to study spatially inhomogeneous systems (such as "spin glasses")

In addition, since μSR can measure the spatial distribution of magnetic field directly, μSR is the ideal tool for the study of vortex state in the type II superconductors to find the physical properties of superconductivity though the detailed magnetic structure of vortices.

Another important field is the study of defect dynamics in crystalline solids as probed by μSR, which includes quantum diffusion of positive muon and muonium[1] in metals and insulators.

Summary of the Experiment Procedure

1. Creation of muon at the accelerator
2. Polarized muons are implanted into a sample and come to rest at interstitial sites.
3. Muon's spin precess in local magnetic field.
4. Muons decay to positrons and positron is distributed with muon spin asymmetrically.
5. Analyzing magnetic properties by positron spectrum.

[1] a muonic analogue of atomic hydrogen where the proton is substituted by a positive muon

5.3.1 The Asymmetry Spectrum and Analysis

Muons are implanted one at a time in a sample and subsequently decay into positrons. By virtue of parity violation, the distribution of decay positrons are asymmetric with respect to the spin polarization vector. Analysis of positron distribution gives information on magnetic field distribution within a sample. Scintillation detectors placed around the sample detect the positrons. The positron count rate of

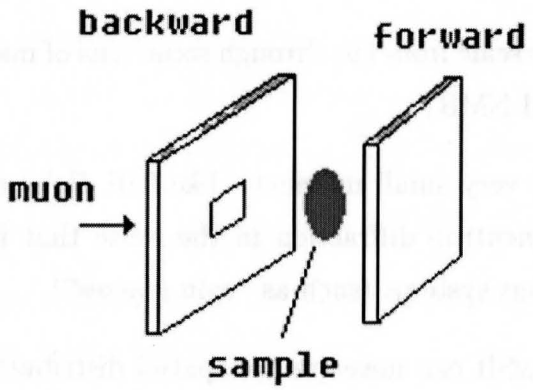

Figure 5.4: Forward and backward detector arrangement in longitudinal field experiment.

each counter $N_{B,F}$ is the integral of the positron angular distribution over the counter solid angle and positron energy. By accumulating a sufficient positron events (typically $\sim 10^7$), one can find the muon polarization function as a function of time.

$$N_{B,F}(t) = B_{B,F} + N_o \times e^{-t/\tau}[1 \pm A_{B,F}P_z(t)] \tag{5.2}$$

where $B_{B,F}$ = beam-born background in the positron detector
$A_{B,F}$ = intrinsic asymmetry of positron detector
$P_z(t)$ = time dependent muon polarization function
N_0 = normalization value

At a continuous muon source like TRIUMF muon facility, $B_{B,F}$ is generally time independent and determined by using negative time ($t < 0$) time bins in

positron spectra. Specifically background signals($B_{B,F}$) are obtained by delaying the positron(e^+)signals with respect to the muon trigger signal.

The **Raw Asymmetry** is defined by

$$A_{raw} = \frac{(N_B(t) - B_B) - (N_F(t) - B_F)}{(N_B(t) - B_B) + (N_F(t) - B_F)} \tag{5.3}$$

Exponential terms are removed in the asymmetry equation.

In reality, alignment error of positron detector exist. This causes different backward and forward solid angle and eventually result in a 'baseline shift'. Therefore, In case of $\alpha \neq 0$ and $\beta \neq 0$ small correction to the raw asymmetry is required.

The corrected asymmetry then becomes:

$$A_{cor}(t) = \frac{(1-\alpha) + (1+\alpha)A_{raw}(t)}{(1+\alpha\beta) - (1-\alpha\beta)A_{raw}(t)} \tag{5.4}$$

where $\alpha = \frac{N_F}{N_B}$, $\beta = \frac{A_F}{A_B}$

α is the ratio of the forward and backward counts. β is the ratio of the counter asymmetries and is close to one and $\beta \neq 1$ slightly distorts the shape of the asymmetry. One can experimentally obtain α, β by fitting the data of applied weak transverse field of a standard sample such as pure silver.

Obviously $\frac{1-a}{1+a}$ is the total asymmetry for unpolarised muons. Total asymmetry $A_{cor}(0)$ is $0.2\sim$ 0.3 in a normal μSR experimental setup but some experiment setups might have lower total asymmetry value.

By extracting the asymmetry and $P(t)$ from transverse field (TF), longitudinal field (LF) measurement for a given sample as a function of temperature, magnetic field, pressure etc, one can get information on the spatial distributions and dynamical fluctuations of magnetic field inside the sample. The measured magnetic field is averaged over the all muon sites.

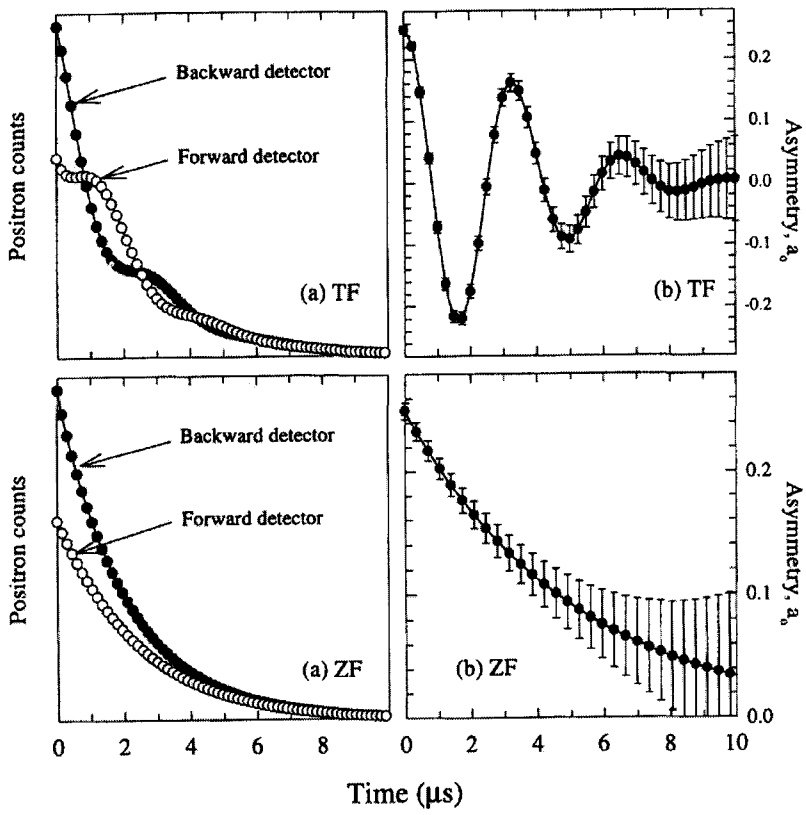

Figure 5.5: (a)Simulated raw positron spectra in forward and backward detector for transverse field(TF) and zero field(ZF).

5.4 Probing Magnetic Field due to Static Random Spins

Many materials have spins that are oriented in a random static. Thanks to μSR technique, one can explore the magnetic field configuration without applying magnetic fields in the sample.

Thirty years ago, Japanese physicists Kubo and Toyabe elucidated the random static spins in zero and low external fields[40]. The Kubo-Toyabe theory assumes that there are no fluctuations in the spin system. In this static situation, each muon detects a local field which causes spin precession around the axis of external magnetic

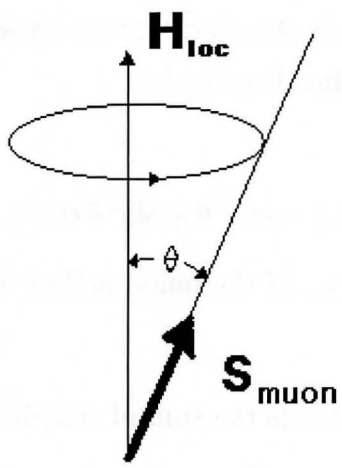

Figure 5.6: Larmor spin precession, S_{muon} is the initial muon direction and H_{loc} is static local field. Precession frequency $\omega = \gamma_\mu \ H_{loc}$. One can find the internal magnetic field by measuring the precession frequency.

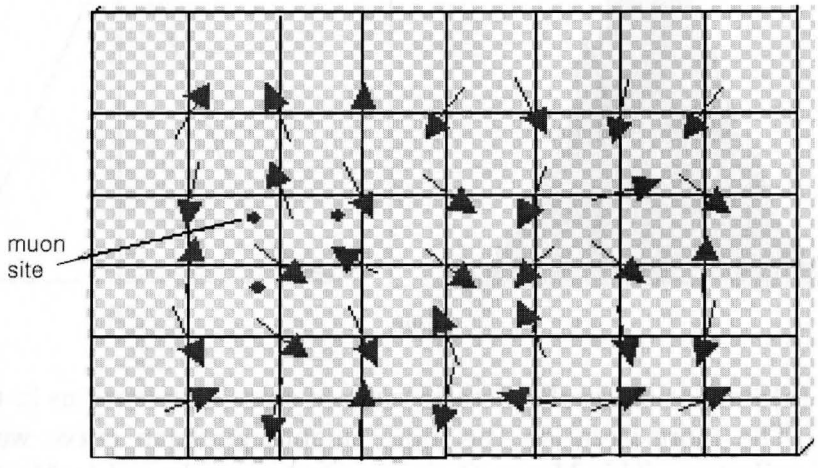

Figure 5.7: Random oriented spin system shows the random static field distribution in the square lattice solid material. After being implanted in the sample, muon finally stopped at electrically interstitial site, the so called muon site. It must be remembered that all muons are same spin direction initially (100% spin polarization). If there is no external magnetic field, only local magnetic fields can depolarize muon spin direction.

field.

The spin polarization function of a single muon whose spin is at an angle θ to the local field B_Z as a function of time is given by

$$S_z(t, B_z) = \cos^2\theta + \sin^2\theta \cos\gamma_\mu B_z t \tag{5.5}$$

where the gyromagnetic ratio, γ_μ, of the muon is $2\pi\times$ 13.5KHz/Gauss (or $2\pi\times$ 135 MHz/Tesla).

The total polarization function is the sum of contributions from all muons;

$$P(t) = \int \rho(H) S_z(t, B_z) dB_z \tag{5.6}$$

where $\rho(H)$ is the distribution of local magnetic fields.

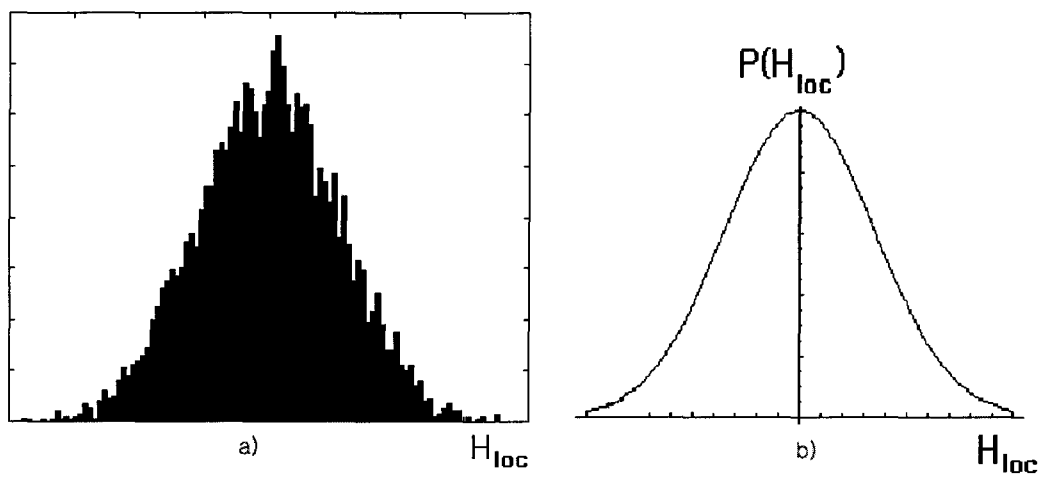

Figure 5.8: (a)Simulation result of static random spins distributions in the solid(1000 iterations). The more iteration the more smooth gaussian curve we get (b)Ideal Gaussian distribution. This Monte-Carlo simulation conducted in Matlab

We can illustrate the Kubo-Toyabe theory by considering a random local magnetic field distribution is generated by periodic crystal lattice with atomic size of above Figure (5.7). The random local magnetic field, H^{loc}, at the muon site can be approximated by a Gaussian distribution[2] with a width of random field Δ =

[2]this distribution corresponds to a the dense random spin system. If magnetic moments such as in canonical spin glasses are dilute, the field may be represented by a Lorentzian function.

$\gamma_\mu \sqrt{\frac{1}{2}(< H_x^{loc} >^2 + < H_y^{loc} >^2)}$ and the random local magnetic field distribution $\rho(H)$ at the muon site is a gaussian field;

$$\rho(H) = \frac{\gamma_\mu}{\sqrt{2\pi}\Delta} \cdot \exp(-\frac{\gamma^2 H^2}{2\Delta^2}) \tag{5.7}$$

where Δ is related to the width of the gaussian distribution

After averaging equation 5.5 over the field distribution function then we can get the time evolution of the muon spin polarization function, which is called Kubo-Toyabe function:[40]

$$P^{GKT}(t, \Delta) = \frac{1}{3} + \frac{2}{3}(1 - \Delta^2 t^2) \exp(-\frac{\Delta^2 t^2}{2}) \tag{5.8}$$

The constant $\frac{1}{3}$ term is an important sign that the local field is static, and the damped $\frac{2}{3}$ term is related to Δ.

One can get more information about the magnetic characteristics by applying longitudinal field. The first longitudinal field experiment was performed by R.S. Hayano *et. al* [41]. The effect of external field modify the ZF polarization function. The LF muon spin polarization function in a Gaussian field distribution is given by

$$\begin{aligned} P^{GKT}(t, \Delta, H_L) &= 1 - (\frac{2\Delta^2}{\omega_L^2}[1 - \exp(-\frac{\Delta^2 t^2}{2}) \cos \omega_L t] \\ &+ (\frac{2\Delta^4}{\omega_L^3}) \int_0^t \exp(-\frac{\Delta^2 \tau^2}{2}) \sin \omega_L \tau d\tau \end{aligned} \tag{5.9}$$

where H_L stands for the applied longitudinal field and $\omega_L = \gamma_\mu H_L$.

In zero external applied magnetic field, equation 5.9 is reduced to as equation 5.8. That is, one can observe the decaying and then persisting $\frac{1}{3}$ term. As the external applied magnetic field gets stronger, the signal gets flatter, because the second and third term can be ignored for $\frac{\Delta}{\omega_L} \to 0$. The Δ can also be extracted from the initial Gaussian decay rate. The LF polarization function can be observed on Figure (5.10). The effect of recovering the total asymmetry with LF is called 'decoupling'.

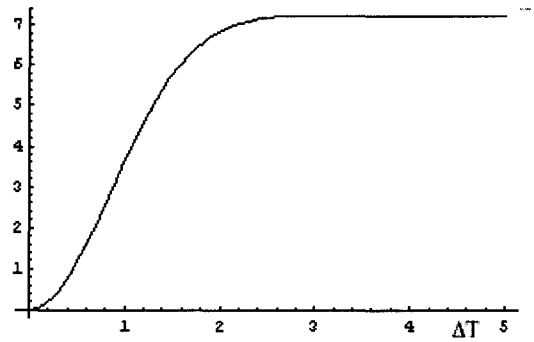

Figure 5.9: Integral term $\int_0^t \exp(-\frac{\Delta^2\tau^2}{2}) \sin\omega_L\tau d\tau$. When $\Delta T > 5$, the integral term becomes essentially time constant.

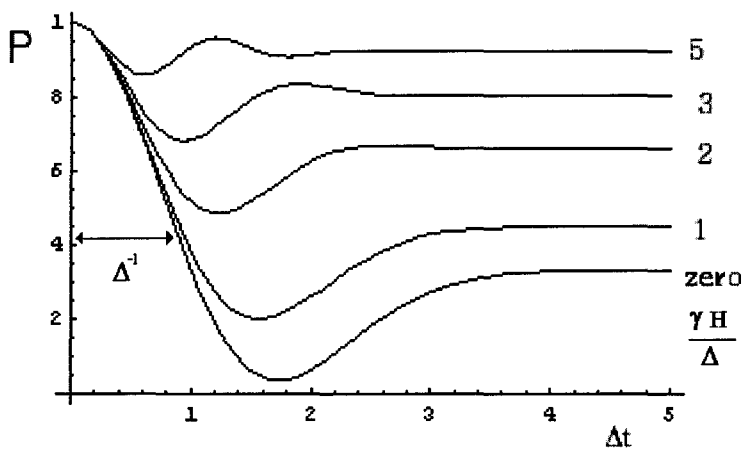

Figure 5.10: Muon spin polarization function of the gaussian distribution of random static spin system with various longitudinal field. The recovery of total asymmetry with increasing applied magnetic field is a one of the most important feature of LF μSR experiment. Also note that static only spin systems show a constant long time signal[33].

5.5 Dynamic Relaxation for Gaussian Local Magnetic Field

In the previous section, it was assumed that the local magnetic field is static at the muon site. In some case, however, the local field is modulated by fluctuating

local moments. What we measure is the the effect of possible coexisting static and dynamic local fields.

Strong Collision Model[41]

One way to investigate the effects of fluctuating fields is to employ the strong collision model. This model assumes that the local magnetic field changes its value at a time t with a probability $\rho(t) \propto \exp(-\nu t)$. It will be assumed that after the collision, the spin has lost all information about its previous spin direction.

At early time, the relaxation function will decay following the static Kubo-Toyabe function. Suddenly, a first collision happens at $t = t_1$. At that very point, a new Kuto-Toyabe starts with t_1 as the initial time. And second collision happens at $t = t_2$ and this procedure will repeat until asymmetry decrease to zero. This process can be described by following equation:

$$\begin{aligned} P_z(t,\nu) &= \exp(-\nu t)[P_z(t) + \nu \int_0^t P_z(t_1)P_z(t-t_1)dt_1 \\ &+ \nu^2 \int_0^t \int_0^{t^2} P_z(t_1)P_z(t_2-t_1)P_z(t-t_2)dt_1 dt_2 + \cdots] \ , \end{aligned} \tag{5.10}$$

where P_z is the static relaxation function.

In the limit of fast fluctuation($\nu/\Delta > 5$), equation 5.10 is reduced to:

$$P_z(t,\nu) = \exp(-2\Delta^2 t/\nu) \tag{5.11}$$

It is worthwhile to note that at high enough temperature (corresponding to very fast fluctuation) the relaxation due to fluctuation decrease and will be negligible. Because muons can be not respond. Figure 5.11 shows the dynamic relaxation function for various values of $\frac{\nu}{\Delta}$.

On the other limit of slow fluctuation, One can observe the $\frac{1}{3}$ tail of the ZF Kubo-Toyabe function and the polarization function of the long time tail is calculated as:

$$P_z(t,\nu) = \frac{1}{3}\exp(-2/3\nu t) \tag{5.12}$$

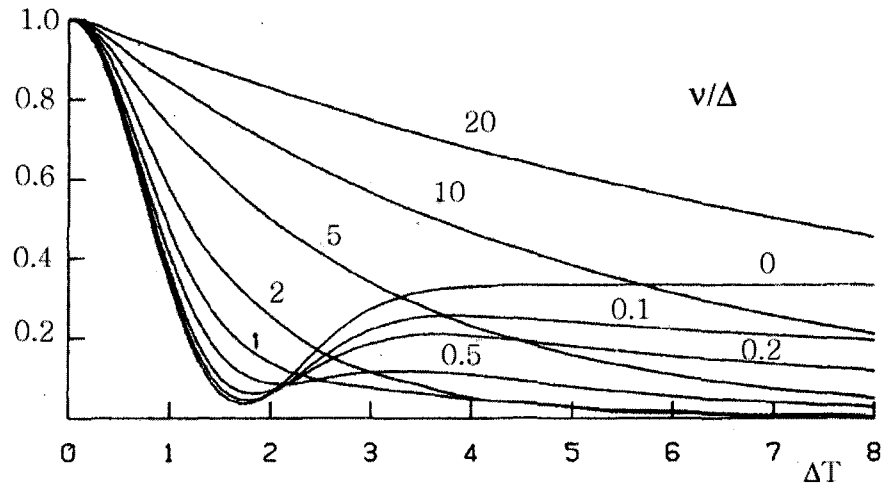

Figure 5.11: Zero-Field muon spin relaxation of the dynamic local field numerically obtained by equation 5.10. As fluctuation is stronger, the relaxation become slower and the gaussian line shape changes into an exponential shape

When a LF is applied, dynamic spin flipping process would make above equation's ν in ZF to $\nu/(\omega^2+\nu^2)$. Therefore one can obtain the relazation rate with applied field:

$$P_z(t,\nu,\omega_L) = \exp[(-2\Delta^2\nu t/(\omega_L^2+\nu^2)] \tag{5.13}$$

5.6 Stretched Exponential Relaxation Function

In the paramagnetic regime, dynamic relaxation data is often well fitted to exponential function. Systems with more than one spin fluctuation rate or with more than one muon site will have more than one relaxation rate. The spin polarization function can often be characterized expressed by a **stretched exponential function**[30],

$$G_z(t,\lambda,\beta) = A_1 \exp(-\lambda_1 t) + A_2 \exp(-\lambda_2 t) + ... \cong A \exp(-\lambda t)^{\beta} \quad , \qquad (5.14)$$

where β is exponent.

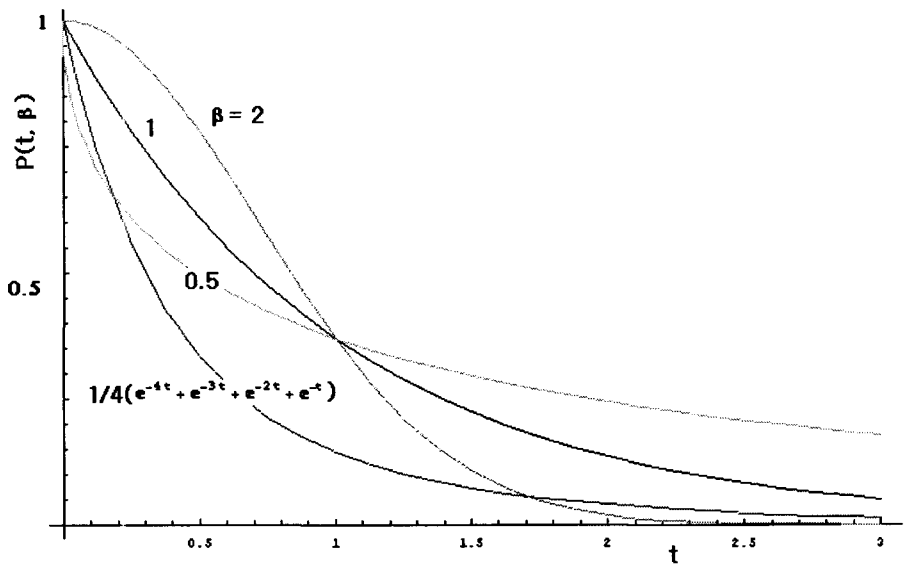

Figure 5.12: Stretched exponential polarization function for various β with $\lambda = 1$.

For example, moderately concentrated(5% $\sim$ 10%) spin glasses show stretched exponential polarization. When the temperature is lowered toward T_g, relaxation rate increases and β decreases from a value of 1 at higher temperature to 1/2 as T_g is approach. This has been experimentally measured in AuFe [37]. The above 1/2 reduction of β assumes that all magnetic moments are fluctuating with a single frequency ν. If we consider various ν, then β will approach 1/3 theoretically[9]. Stretched exponential behavior has been observed in geometrical frustrated system, with β varying from 1 at high temperatures down to $\sim$ 0.4 at low temperature[?].

5.7 Sample Mounting and μSR Measurement

The next table presents the three different μSR measurements performed on $Ho_2Ru_2O_7$. See Appendix A for a complete listing of all μSR measurements.

	beamline	spectrometer	experiment	temperature
1	M20	LAMPF	ZF/LF(2000G)	2K~200K
2	M15	HiTime	ZF/LF(2000G,1T,3T,5T)	2K~250K
3	M15	DR	ZF/LF(2T,3T)	15mK~5K

▲ **LAMPF** has a 3 dimensional Helmholtz coil for magnetic field (0.3 T/z(0.39 T on M15), and 10 mT/x,y).

▲ **HiTime** has a superconducting magnet (7.0 T/z). The sample space and scintillators are of special compact design in order to achieve high field and high timing resolution.

▲ **DR** is a spectrometer combining a dilution refrigerator and superconducting Helmholtz magnet (5 T/z, 5 mT /x,y).

5.7.1 Sample Mounting

The ceramic sample had dimensions of 20 mm×10 mm×2 mm(thickness). Given the imperfection of muon beam collimation, a small fraction of the incoming muons could be implanted in the sample holder. In order to minimize this background muon signal, the sample holder should be made of materials with small nuclear dipole moments. A sample holder made from silver was used because silver has almost no nuclear magnetic moment.

Like in specific heat measurements of chapter 5, APiezon N grease was used to hold the sample to the sample holder. The grease also provides good thermal contact between sample and sample holder. A thin silver foil was used wrapped around the sample and sample holder.

Zero-Field (ZF) and Longitudinal-Field (LF) μSR measurements were conducted on the M15 and M20 beam line at TRIUMF. The sample temperature was controlled between 2K and 250K in a He cooled cryostat. Zero field calibration (less than 0.5 gauss) was conducted by using Hall probe and confirmed using the muon precession signal in an empty sample holder.

The DR (dilution refrigerator) measurements was performed on M15. The sample temperature was controlled between 0.15K and 5K.

5.7.2 Positron background

Unfortunately, the muon beam is not 100% pure. There are impurity particles such as positrons. If muons somehow collide with the apparatus before being implanted the sample, then positrons are generated by muon decay. Even though the muon scintillator can discriminate most of the incoming positrons, some positrons have enough energy to trigger the muon counter. Those positron are few in comparison to muons. However this affects only a small beginning time window(a few nanosecond) and consequently create a high pulse in the beginning. The positron speed is around $\sim$25% of speed of light and distance between muon counter and forward counter is around 10 cm. Therefore a peak exists around 1 ns.

Figure (5.13) shows the positron noise peak. Here the peak appears as a dip in the asymmetry spectrum which combines spectra from backward and forward detectors.

High temperature asymmetry data was chosen because there is no big asymmetry signal change in the beginning. The noise signal peaks at 1 ns and extends up to 10 ns. It cause unwanted noise on the asymmetry signal within 10 ns, and one needs to chop the first 10 ns out of the signal.

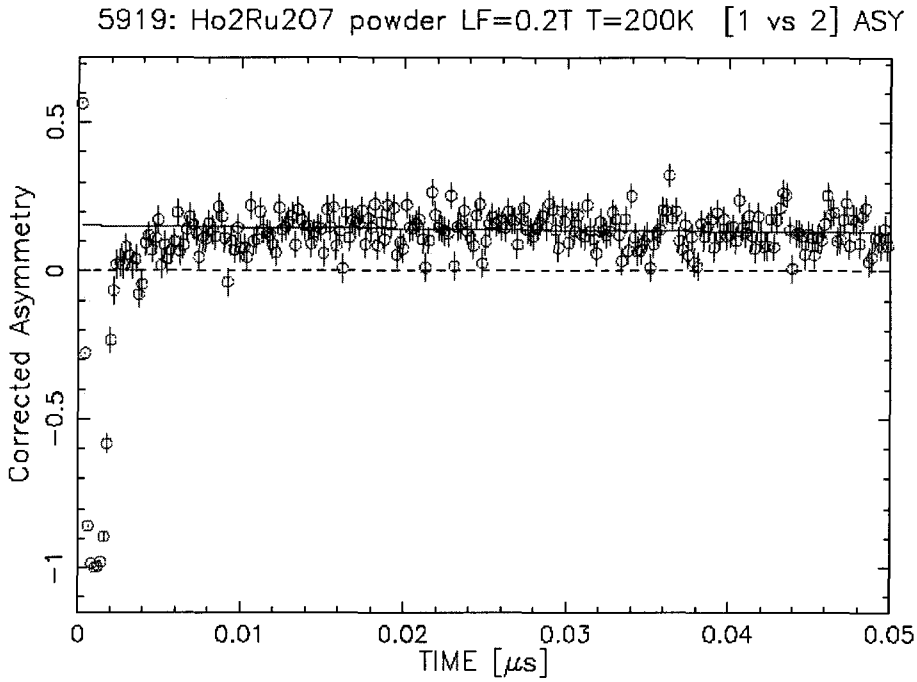

Figure 5.13: Positron background exists at 1ns and extended up to 10 ns

5.7.3 ZF Data Analysis

ZF-μSR is a powerful tool for probing magnetic properties, because samples can be measured without applied magnetic field which might perturb the sample. Moreover, ZF-μSR works well with both ceramic and single crystal samples.

We used the computer program called **MSRFIT** to analyze and fit the μSR data. MSRFIT uses another subprogram MINUIT which minimize χ^2 to find a optimal values for fit parameters.

Figure 5.14 shows selected ZF runs between the range of 2K$\sim$199K from M20. Below 65K we see a two component relaxation function. When the relaxation rate becomes sufficiently rapid at low temperature, we can not observe the high relaxation because it is hidden in early 10 ns window.

Even though the TRIUMF continuous wave (CW) μSR facility has a extremely

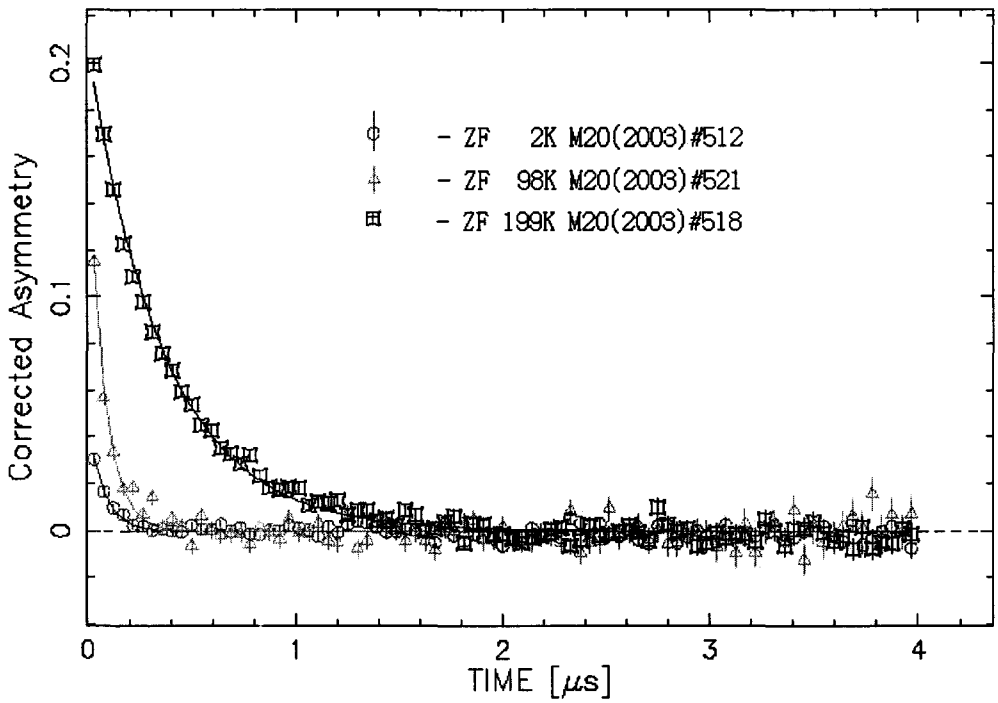

Figure 5.14: Muon spin polarization data for $Ho_2Ru_2O_7$ at various temperatures in ZF from beam line M20(2003).

high time resolution ($\sim$ 100 ps), the muon depolarization below 50K is so fast that a large portion of the muon signal disappears during the hidden 10 nS time window, as mentioned previous section. This indicates that the gaussian field distribution width (Δ) due to the is quite large. At 2K, Δ looks bigger than $\sim \frac{1}{10nS} = 100\ \mu s^{-1}$. Therefore, below 2K the average internal field can be roughly estimated to be bigger than $B_{int} = \frac{\Delta}{\gamma_\mu} = 0.7$ T (Tesla).

Figure (5.15) shows a significant increase of the relaxation approaching 95K with decreasing temperature. This spin ordering temperature is agreed with the susceptibility data and heat capacity data of previous chapters.

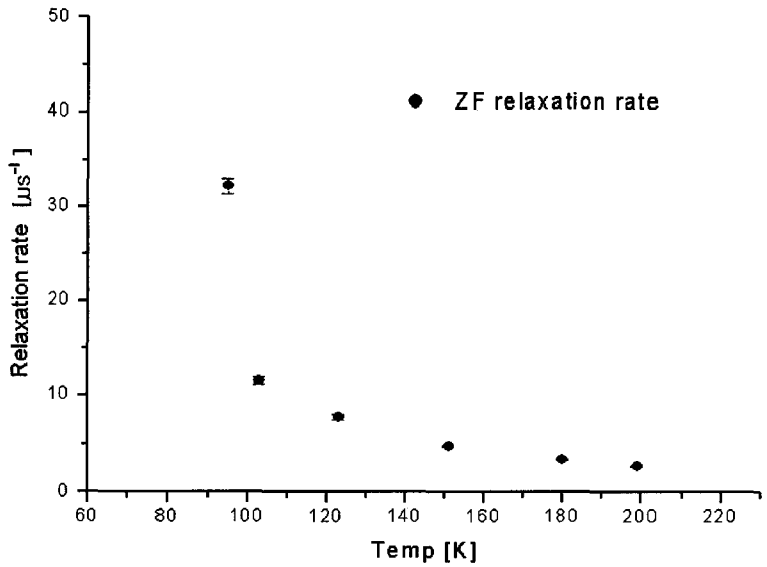

Figure 5.15: ZF Relaxation rate. Relaxation rate sharply increase around 95K which is the ruthenium antiferromagnetic transition temperature.

Muon Precession Signal due to Ruthenium AFM Ordering

As seen in Figure (5.16), we observed precession signals in the ZF data below the ruthenium ordering transition temperature (95K). This indicates that all muons feel roughly the same magnetic local field due to ruthenium antiferromagnetic ordering at muon sites.

The polarization signal between 2K and 150K was fit to the two-component equation (5.15).

$$\frac{2}{3}Ae^{-\Delta_1 t}\cos(2\pi ft) + \frac{1}{3}Ae^{-\Delta_2 t} \tag{5.15}$$

where A is asymmetry and f is precession frequency. Δ_1 is the dephasing rate of the muon precession signal and Δ_2 is the relaxation of the 1/3 tail by field fluctuations.

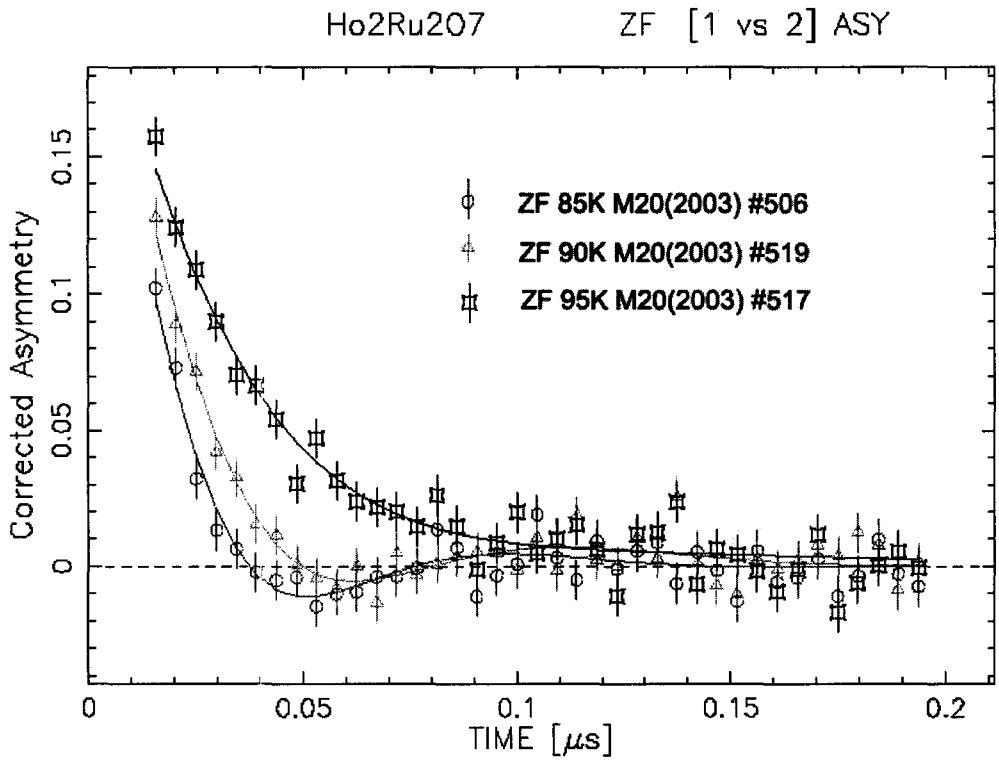

Figure 5.16: The precession signal due to Ruthenium antiferromagnetic internal field. The strongest precession signal is observed at 85K.

The fitted frequencies as a function of temperature are shown in figure (5.17). At 85K, where the precession signal is most clearly displayed, the frequency found to be 8.5 MHz and relaxation rate is 39 μs^{-1}. Therefore average internal field due to ruthenium AFM ($\frac{8.5MHz}{\gamma_\mu}$) is 630 Gauss.

The precession signal is weaker as temperature gets lower due to the increase of Δ_1. Below 50K, one can not notice any oscillation in the polarization data, despite the frequency likely being increased with decreasing a temperature due to the ruthenium antiferromagnetic ordering magnetization. Presumably holmium spin fluctuations wash out the precession signal.

As seen in figure 5.17(B), The Δ_1 starts rising around 100K. This indicates the ruthenium ordering get stronger. Since a large portion of polarization signal is lost

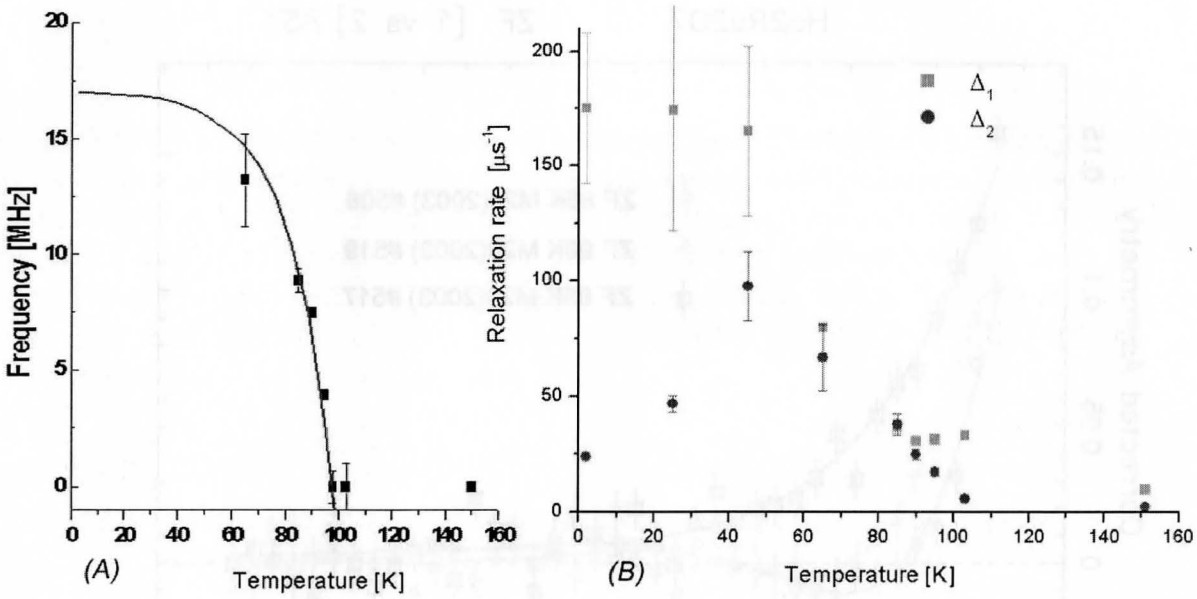

Figure 5.17: (a) Precession frequency with temperature. The frequency is proportion to ruthenium antiferromagnetic ordering which we can call the ordered parameter. Theoretically it become saturation value as temperature approach zero. Red solid line which display the mean field theory fit to 17 MHz at zero temperature. 17 MHz is correspond to 1200 Gauss. (b) Δ_1, Δ_2 with temperature. Below 50K, the Δ_2 have large error bars. Because a large portion of polarization signal is lost in the early 10 ns window.

in the early 10 ns window below 50K, we found that Δ_2 below 60K have large error bars. As we previously discussed, reduced precession signals is caused by the high value of Δ_1.

In the case of others frustrated systems, relaxation begins to rise at around $2\times T_N$(AFM transition temperature)[42]. However, relaxation of $Ho_2Ru_2O_7$ seems to begin to rise at $\sim$125K($\sim 1.3T_N$). This may indicate that geometrical frustration of ruthenium is not as strong as many other frustrated systems.

The LF data shows that much of the relaxation of the precession signal is due to dynamics, not by static inhomogeneous field.

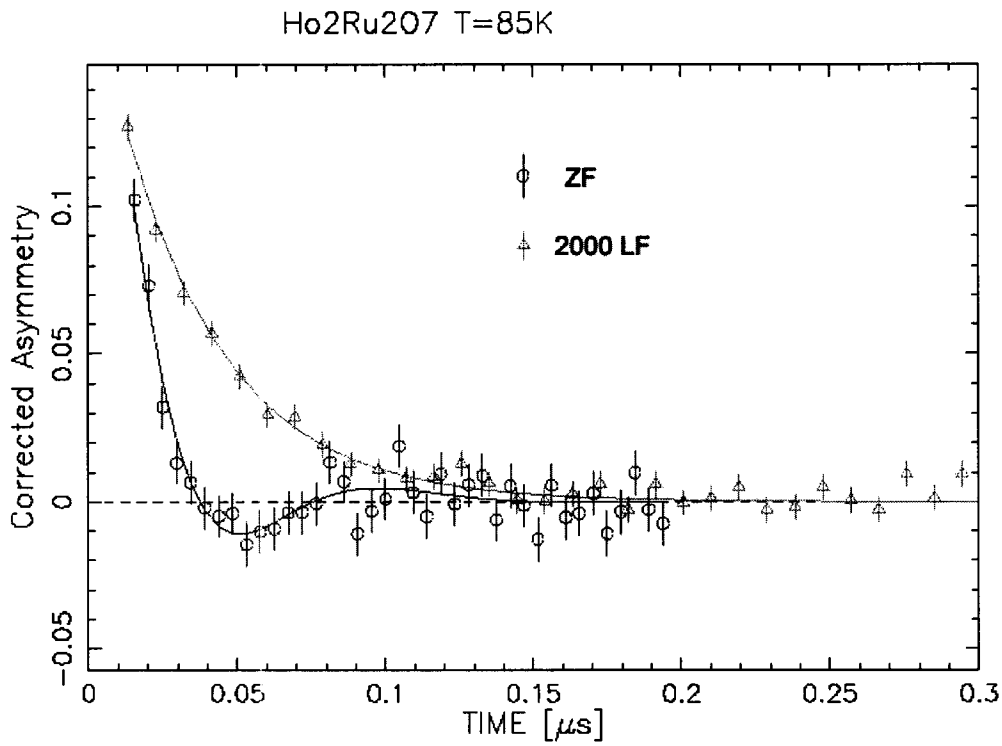

Figure 5.18: *mu*SR spectra at 85K. The precession signal in ZF due to ruthenium relaxed due to holmium moments. Triangle symbols are 2000 Gauss LF at 85K. The relaxation of 2000 Gauss LF is the result of fluctuating moments.

Zero Field DR data

The large internal field at low temperatures causes that much of the μSR signal is hidden within the early 10nS time window. ZF-DR data Figure (5.19) shows this reduction of asymmetry signal. What we can see is the remaining tail of the relaxation signal. It looks like there is little temperature dependency over 0.015K and 1.4K range. One thing we can say that relaxations showing some fluctuation of local field continue to exist down to 0.015K. The precession signal of holmium moment below its ordering temperature (1.4K) is probably hidden within the early 10ns time window.

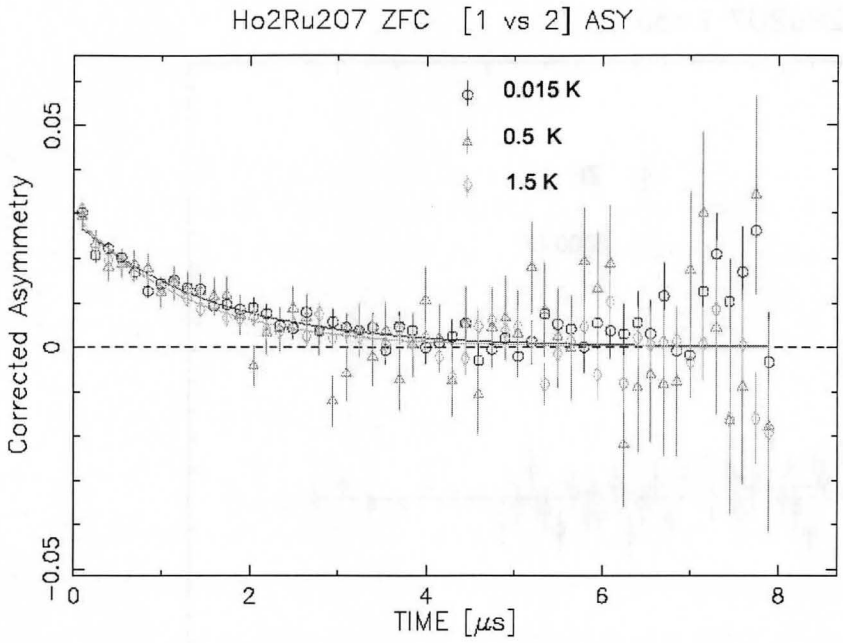

Figure 5.19: ZF-DR data from beam line M15(2003). Data of 0.015K, 0.5, 1.4K and 5K are displayed. There is no visible precession signal of holmium AFM ordering temperature. 1/3 tails continue to decrease to zero and relaxation ~0.4 MHz. Considering the relaxation due to nuclear dipole(~ 0.1 MHZ) , there may be a dynamic component contributing this relaxation down to 0.015K.

5.7.4 LF Data Analysis

ZF measurements are the subset of LF measurement with no applied magnetic field. LF measurements provide many advantages for experiments of random spin systems such as spin glasses, spin liquid, frustrated system. However, when longitudinal field is applied, there are some systematic efforts to be considered.

In LF measurement, α may change as the external field shifts the path of the incoming muons and positrons. The behavior of α with increasing temperature shows a increasing trend. Because as temperature decreased small amount of thermal contraction of cryostat slightly change the effective angles of the detectors. At low temperature, we estimated α by extrapolating the measured high temperature α data. The low temperature data from M15 was analyzed with the appropriate α fixed, since

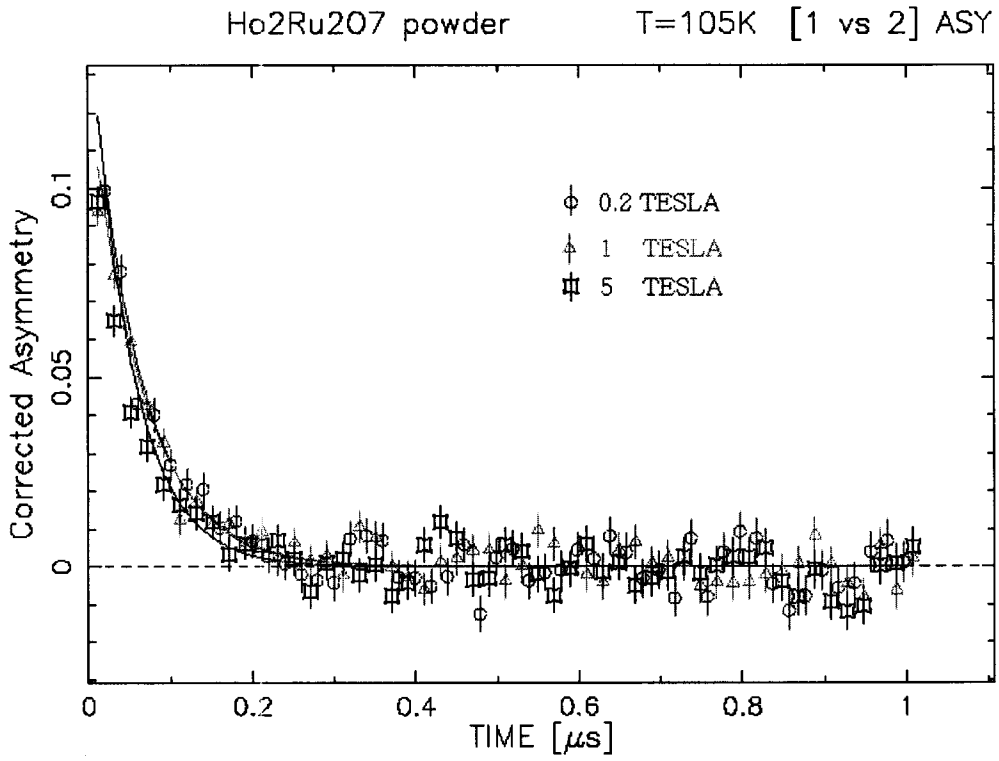

Figure 5.20: High temperature (105K) relaxation data above Ruthenium transition temperature (95K). There is little LF dependence of the relaxation rate showing the fluctuation rate ν is rapid. In most case, dynamic relaxation rate($1/T_1$) of paramagnetic regime shows little dependence on LF

fitting parameters often play-off one another.

One can get some critical footprints to determine the magnetic state of the solid by LF measurement. In the paramagnetic regime(above the ruthenium ordering temperature of 95K), the relaxation rate of figure (5.20) shows little dependence on longitudinal field.

If we use the equation 5.13, the relaxation rate is dependent on both the applied longitudinal field and the fluctuation. The typical fluctuation rate in solids varies between $\nu = 10^9 \sim 10^{13} Hz$ [9]. Since ω_L is only around 135 MHz($\sim 10^8$ Hz) when LF=1 Tesla is applied($\nu \gg \omega_L$), polarization will not be changed much when 1 Tesla of longitudinal field is applied. The little dependence on longitudinal field indicates

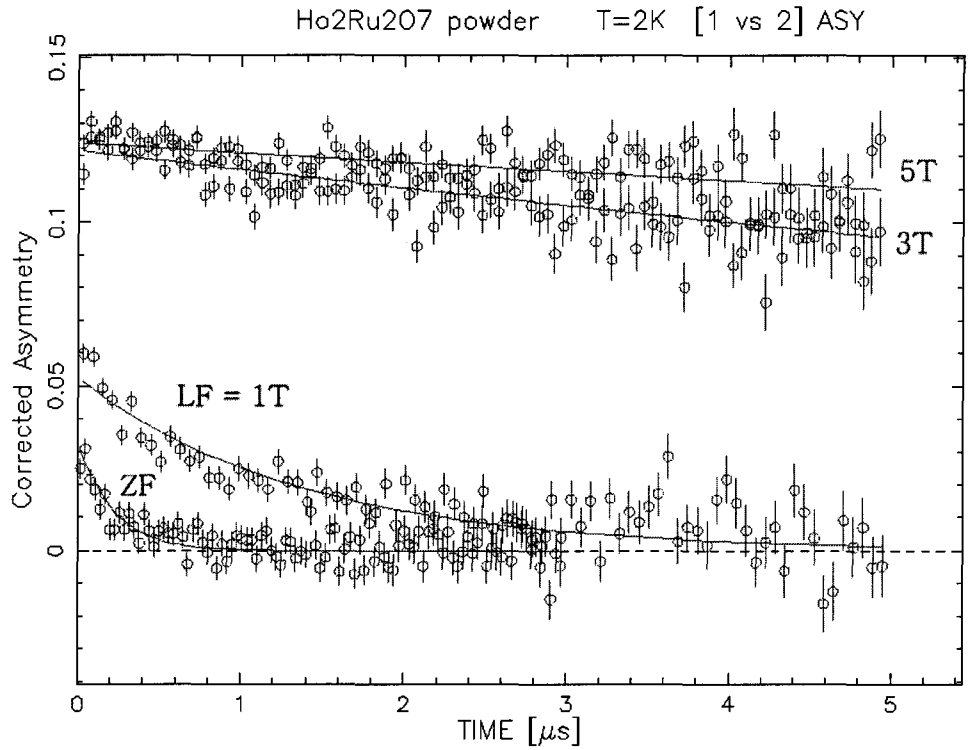

Figure 5.21: Muon spin polarization data for $Ho_2Ru_2O_7$ with various LF at 2K. The muon spin is depolarized by mostly big holmium moments. The restoration of the total asymmetry with increasing LF is called 'decoupling' and 3 Tesla is needed for full decoupling.

that the relaxation is caused by rapid spin fluctuations.

It is interesting to examine the temperature range (below 95K) in which a ruthenium is a ordered and the holmium is a paramagnetic. Unlike dynamic process, static field is sensitive to LF and one can get the strength of static field by measuring the degree of the sensitivity. The figure (5.21) shows the ZF and LF data (HiTime/M15) at a temperature of 2K just above the homium ordering temperature. The two bottom lines are the ZF and LF = 1T data. More than one third of the relaxation happens within the 10 nS hidden time window that the instrument is not able to observe. Therefore what we are seeing in the figure is the remainder of one third tail.

From the high temperature relaxation data of figure (5.20), total asymmetry is

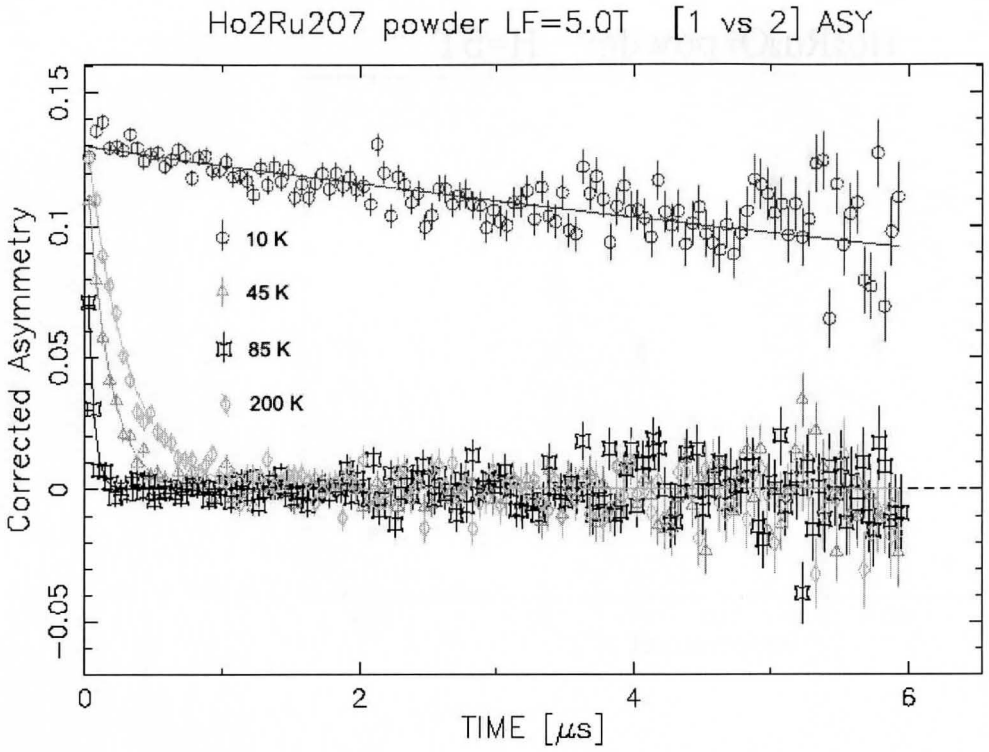

Figure 5.22: LF muon spin polarization data for $Ho_2Ru_2O_7$ at various temperatures in 5 Tesla.

determined to be about 0.16. The ZF data at longer times flattens out with a small negative slope. The LF = 1T data also show that two thirds of amplitude is invisible in the hidden window and then show continuous decreasing signal. The LF = 3 and 5T data display weak relaxation. Muon spins are depolarized by internal magnetic field at 2K. And the degree of depolarization speed is decreased (decoupled) by increasing longitudinal field. This means that the external longitudinal field (5 T) is larger than the internal field.

Figure (5.22) displays LF muon spin polarization data for $Ho_2Ru_2O_7$ at various temperatures in 5 Tesla. The polarization signal is significantly decoupled at 10K which indicate the fluctuation slow down at low temperature. Figure (5.23) shows the 5 Tesla LF relaxation rate as a function of temperature. The relaxation rate is maximum at 80 K although error bars make it difficult to identify the exact maximum

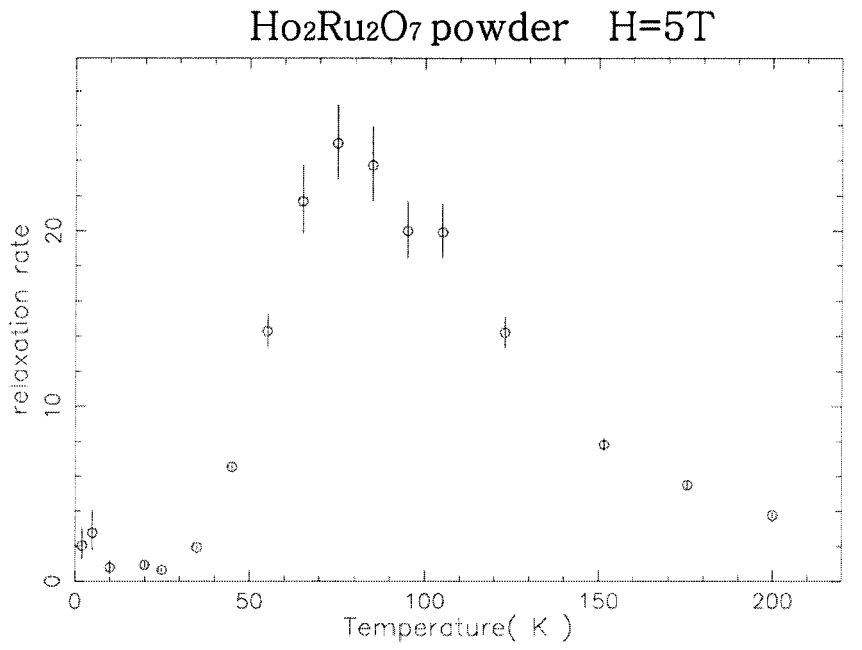

Figure 5.23: 5 Tesla LF experiment. Relaxation rate is maximum at 80 K but error bar make it difficult to identify the exact maximum value.

value. Unlike the ZF experiment (M15), significant relaxation is measured well above ruthenium transition temperature(95K). Small increase of relaxation below 5K might be reflecting the slow down of holmium spin fluctuation.

Although we discuss the little LF dependence on relaxation rate above the ruthenium ordering temperature, we found LF relaxation is little larger than ZF one. As we use the equation 5.13, this indicates that application of a large LF actually decreases the fluctuation rate(ν) more than the increase of ω_L.

Figure (5.24) shows spectra measured at 0.02K. 1K, 5K. The 0.02K. 1K data show the decoupling of the long-time tail, indicating that local field are becoming quasi-static. In order to examine the decoupling more accurately. We plot the decoupled asymmetry of 1T LF data in Figure (5.25) as a function of temperature. This indicate that holmium fluctuation have slowed down compared to our applied field (1T or 135 MHZ) below 3K and we interpret this is an evidence for holmium spin freezing.

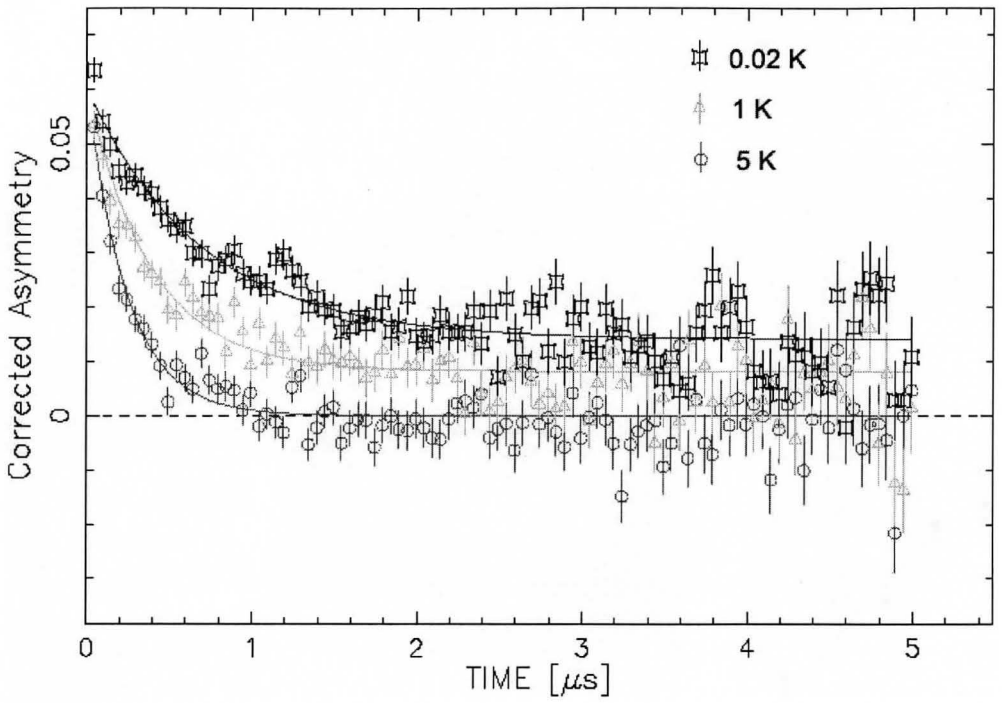

Figure 5.24: 1T LF shows that baseline shift down as temperature increase. Red, green, blue lines indicate 5, 1, 0.02K measurement respectively.

Moreover the result is in agreement with our AC susceptibility data and a supporting evidence of the holmium antiferromagnetic ordering (T=1.4K) observed by neutron scattering measurement[17].

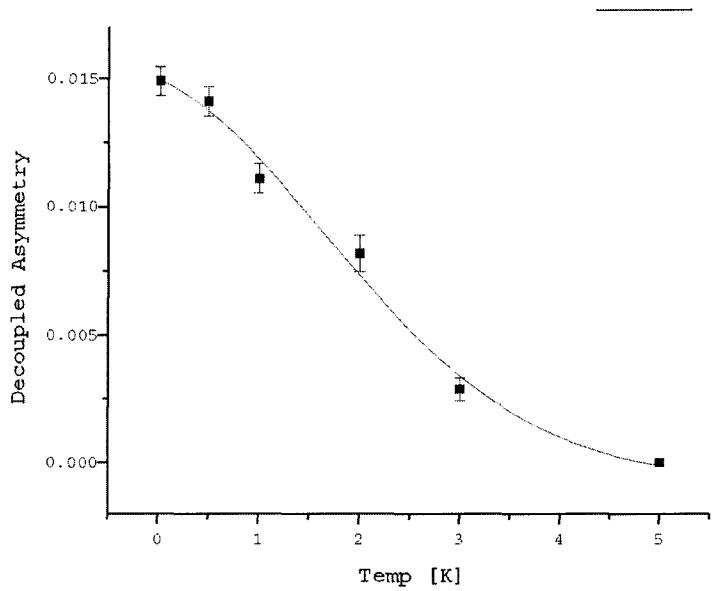

Figure 5.25: Baseline shift of 1T LF data as a function of temperature. Baseline is normalized of 5K's one. This indicate that spin fluctuation significantly slow down in the regime of 1K $\sim$ 3K. Red line is a quide to the eye.

Chapter 6

Conclusions

We have synthesized high quality ceramic specimens of $Ho_2Ru_2O_7$ and performed bulk (DC/AC susceptibility, specific heat) and microscopic (μSR) measurements on them.

We observed ruthenium spins ordering at 95K by DC susceptibility, specific heat experiments as well as in μSR experiments. In AC susceptibility we see a significant frequency dependence (freezing behavior) in χ' and χ'' below 3K which is just above the holmium ordering temperature.

μSR measurements show that the holmium moments are frozen below $\sim$ 1.5K. We can conclude that $Ho_2Ru_2O_7$ does not possess a spin ice ground state.

Despite several attempts, we were unable to synthesize single crystal of $Ho_2Ru_2O_7$ by the floating zone method, due to the high level of ruthenium evaporation. Single crystal, if they can be grown, might be synthesize by some other technique.

Appendix A

μSR Runs

Table A.1: ZF and LF μSR runs from 2K to 250K at M15

	2K	5K	10K	20K	25K	35K	45K	55K	65K	75K
ZF	5870	5876	5879	5880						
1T	5871	5877	5878	5881	5882					
3T	5872	5888	5887	5886	5883	5884	5885			
5T	5873	5889	5890	5891	5892	5893	5894	5895	5896	5897

	85K	99K	105K	123K	151K	175K	200K	250K		
.2T			5903	5904	5911	5912	5919	5920		
1T			5902	5905	5910	5913	5918	5921		
3T			5901	5906	5909	5914	5917	5922		
5T	5898	5899	5900	5907	5908	5915	5916	5923		

Table A.2: ZF and LF μSR runs from 2K to 199K at M20

	2K	25K	45K	65K	85K	90	95/98	103K	123K	151K	180	199
ZF	512	511	509	508	506	519	517/521	502	522	516	523	518
100Oe								503				
100Oe								504		516		
2KOe	513	514			507			505				

Table A.3: ZF and LF μSR runs by Dilution Refrigerator at M15

	15mK	20mK	50mk	500mK	1K	1.5K	2K	3K	5K
ZF	7109		7110	7111	7112	7113	7114		7115
1T		7121		7120	7119		7118	7117	7116
2T		7122							
3T		7123							

Appendix B

Heat Capacity fitting

```
<<Statistics`NonlinearFit`
data1 = Import["C:\aaa1.dat", "Table"]
```

```
{{24.8617, 10.1014}, {31.0459, 16.7845}, {35.5998, 22.6384}, {40.6224, 29.999}, {45.6847, 38.1245},
 {49.5349, 44.5026}, {55.9603, 55.9227}, {60.5261, 65.9313}, {65.5159, 75.9022}, {70.4159, 85.7131},
 {75.3353, 95.1677}, {80.2755, 101.444}, {85.2793, 112.931}, {90.1723, 118.87}, {91.4851, 119.944},
 {92.0415, 120.76}, {92.553, 124.56}, {93.0556, 125.803}, {93.506, 125.981}, {94.0152, 123.935},
 {94.5248, 125.342}, {95.0275, 123.33}, {95.4897, 117.067}, {96.0447, 118.743}, {96.5089, 118.568},
 {97.0253, 118.462}, {97.4738, 118.415}, {97.99, 118.837}, {98.507, 118.993}, {98.961, 119.34},
 {99.4762, 119.757}, {99.9988, 120.117}, {100.457, 121.7}, {102., 123.}, {104., 124.9}}
```

```
ListPlot[data1]
```

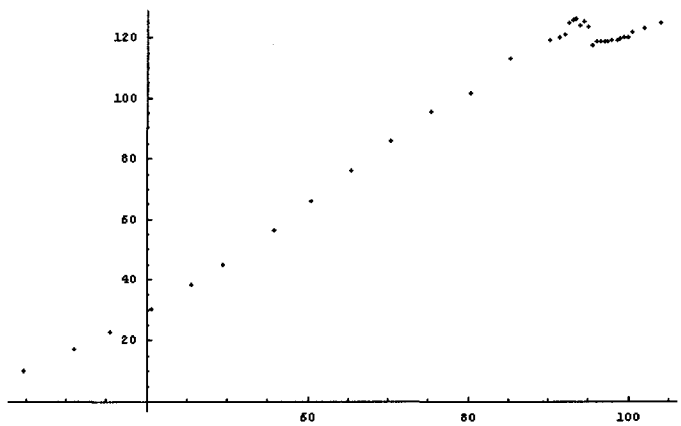


```
- Graphics -
```

```
R = 8.3 * 1; Q =.;
G[Q_, T_] := 9 * R * (T / Q) ^ 3 * Integrate[Exp[x] * x^4 / (Exp[x] - 1) ^ 2, {x, 0, Q / T}]
```

```
Q =.
9 * R * (T / Q) ^ 3 Integrate[Exp[x] * x^4 / (Exp[x] - 1) ^ 2, {x, 0, Q / T}]
```

```
NonlinearFit[data1, 9*R*(T/Q)^3*-1/((-1+e^(Q/T))Q^3 T), T, Q]

BestFitParameters /.
 NonlinearRegress[data1, 9*R*(T/Q)^3*-1/((-1+e^(Q/T))Q^3 T) (124.5 (15 e^(Q/T) Q^4 - 4 π^4 T^4 + 4 e^(Q/T) π^4 T^4)),
  T, Q, RegressionReport → BestFitParameters]
```

$$-\frac{2.2963\times 10^{-5}\,T^2}{-1+e^{56.5/T}}$$

```
Q = 441;
Plot[
 -1/((-1+e^(Q/T))Q^3 T)
  (54.78` (15 e^(Q/T) Q^4 - 4 π^4 T^4 + 4 e^(Q/T) π^4 T^4 + 60 Q^3 T Log[1 - e^(Q/T)] - 60 e^(Q/T) Q^3 T Log[1 - e^(Q/T)] +
      180 Q^2 T^2 PolyLog[2, e^(Q/T)] - 180 e^(Q/T) Q^2 T^2 PolyLog[2, e^(Q/T)] - 360 Q T^3 PolyLog[3, e^(Q/T)] +
      360 e^(Q/T) Q T^3 PolyLog[3, e^(Q/T)] + 360 T^4 PolyLog[4, e^(Q/T)] - 360 e^(Q/T) T^4 PolyLog[4, e^(Q/T)])), {T, 0.1, 200}]
```

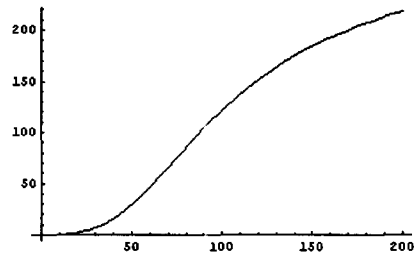


```
- Graphics -

Show[%8, %41]
```

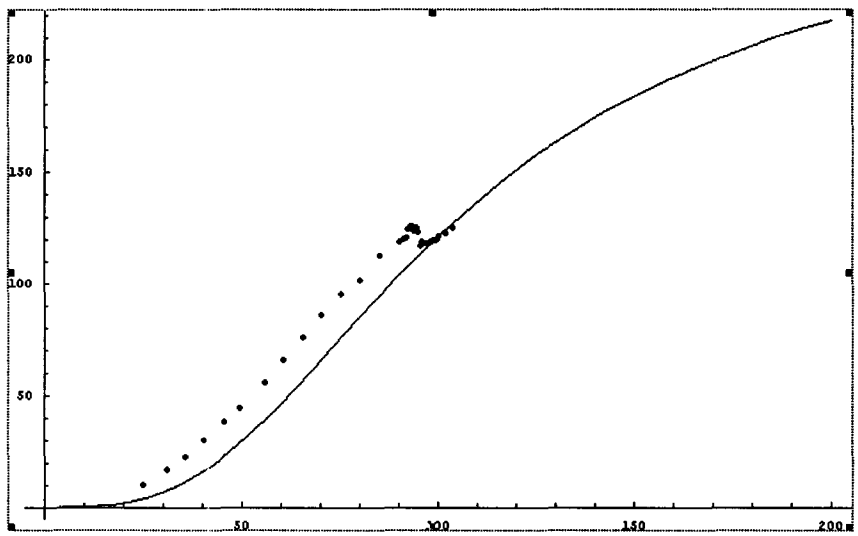


```
- Graphics -
```

Bibliography

[1] K.H. Fischer, Spin Glasses, ISBN-10: 0521447771 (1993)

[2] J.A. Mydosh, Spin Glasses, ISBN-0-7484-0038-9 (1993)

[3] J. N. Onuchic, P. G. Wolynes, Theory of protein folding:The energy landscape perspective. Ann. Rev. Phys. Chem. **48**, 545(1997)

[4] J. J. Hopfield, Neurons with graded response have collective computational properties like those of two-state neurons. Proc. Natl Acad. Sci. **81**, 3088(1984).

[5] N. P. Ong, More is different, ISBN-0691-08866-7 (2001)

[6] A. P. Ramirez, Strongly geometrically frustrated magnets, Ann. Rev. Mater. Sci. **24**, 453 (1994)

[7] P. W. Anderson, ordering and antiferromagnetism in ferrite, Phys. Rev **102**, 1008(1956)

[8] J. E. Greedan, Geometrically frustrated magnetic materials, Chem. Matter. **10**, 3058 (1998)

[9] S. L. Lee, S. H. Kilcoyne, R. Cywinski, Muon Science, ISBN 0-750-30630-0 (1998)

[10] S. T. Bramwell, M. Gingras, Spin ice state in frustrated magnetic pyrochlore materials, Science, **294**, 1495 (2001)

[11] M. J. Harris, S. T. Bramwell, Geometrical Frustration in the Ferromagnetic Pyrochlore $Ho_2Ti_2O_7$, Phys. Rev. Lett. **79**, 2554 (1997).

[12] J. S. Gardner, S. R. Dunsiger, B. D. Gaulin, Cooperative paramagnetism in the geometrically frustrated pyrochlore antiferromagnet $Tb_2Ti_2O_7$, Phys. Rev. Lett. **82**, 1012 (1999).

[13] S. T. Bramwell, M J Harris, Frustration in Ising-type spin models on the pyrochlore lattice, J. Phys. Condens. Matter, **10**, 215 (1998)

[14] H. Kadowaki, Y. Ishii, Neutron scattering study of dipolar spin ice $Ho_2Sn_2O_7$ Frustrated pyrochlore magnet, Phys. Rev. B **65**, 144421 (2002)

[15] Linus Pauling, The structure and entropy of ice and of other crystals with some randomness of atomic arrangement, J. Am. Chem. Soc. **57**, 2680 (1935)

[16] C. Bansal, H. Kawanaka, Structure and magnetic properties of the pyrochlore $Ho_2Ru_2O_7$:A possible dipolar spin ice system, Phys. Rev. B. **66**, 052406 (2002)

[17] C. R. Wiebe, J. S. Gardner, S.-J. Kim, G.M. Luke, S.Wills, B. D. Gaulin, J. E. Greedan, I. Swainson, Magnetic ordering in the spin-Ice candidate $Ho_2Ru_2O_7$, Phys. Rev. Lett. **93**, 076403 (2004)

[18] Quntum Design Inc, SQUID application note, 1052-202

[19] S. T. Bramwell,M. N. Field, M. J. Harris, I. P. Parkin, Bulk magnetization of the heavy rare earth titanate pyrochlores.a series of model frustrated magnets, J. Phys. Condens. Matter. **12**, 483 (2000)

[20] B.D. Cullity, Introduction to magnetic materials, Addison Wesley, ISBN 0-201-01218-9 (1972)

[21] M. Ito, Y. Yasuia, M. Kanada, Nature of spin freezing transition of geometrically frustrated pyrochlore system $R_2Ru_2O_7$,J. Phys. Chem. Solids **62**, 337 (2001)

[22] M. Ito, Neutron Diffraction study of pyrochlore compound $R_2Ru_2O_7(R = Y, Nd)$ above and below the spin freezing temperature, J. Physical society of japan, **69**, 888 (2000)

[23] C. A. M. Mulder, J. A. Mydosh, Susceptibility of the $CuMn$ spin glass: Frequency and field dependence, Phys. Rev. B **23**, 1384 (1981)

[24] K. Matsuhira, Y Hinatsu , K Tenya, Low temperature magnetic properties of frustrated pyrochlore ferromagnets $Ho_2Sn_2O_7$ and $Ho_2Ti_2O_7$, J. Phys: Condens. Matter, **12**, 40 (2000)

[25] C. Y. Ho *et al.*, Specific heat of solids, ISBN-0-89116-834-6 (1988)

[26] C. Kittel, Introduction to Solid State Physics, ISBN 0-471-11181-3 (1996)

[27] K. S. Lee, D.K. Seo, Structural and electronic factors governing the metallic and nonmetallic properties of the pyrochlores $A_2Ru_2O_{7-y}$, J. Solid. Chem, **131**, 405 (1997)

[28] N. Raju, E. Gmelin, R. K. Kremer *et al.*, Magnetic-susceptibility and specific-heat studies of spin-glass-like ordering in the pyrochlore compound $R_2Mo_2O_7$, Phys. Rrev. Lett. B. **46**, 5450 (1992)

[29] M. Bouvier, P. Lethuiller, Specific heat in some gadolinium compounds, Phys. Rev. Lett. B. **43** (1991)

[30] M. T. Rovers, Spin liquid behavior in geometrically frustrated chromium oxides, Master thesis, Mcmaster Univ (2001)

[31] P. P. Kyriakou, The quest for broken time reversal symmetry in Ni^{+2} doped $Bi_2Sr_2Ca(Cu_{1-x}Ni_x)_2O_{8+\delta}$, Master thesis, Mcmaster Univ (2002)

[32] A. A. Azhar, C. D. Mitescu, Specific heat of GdRh, J. Appl. Phys. **57**, 3235 (1985).

[33] Kenji Kojima, Muon spin relaxation measurements of singlet ground-state materials, Ph'D thesis, Univ of Tokyo (1995)

[34] S.H. Neddermeyer, C.D. Anderson, New evidence for the existence of a particle of mass intermediate between the proton and electron, Phys. Rev. **52**, 1003 (1937)

[35] F. Rasetti, Evidence for the radioactivity of slow mesotrons, Phys. Rev. **59** , 613(1941)

[36] T.D. Lee, C. N. Yang, Parity nonconservation and a two-Component theory of the neutrino, Phys. Rev. 105, 1671 (1957)

[37] A. keren, Probing the Spin-Spin dynamical autocorrelation function in a spin glass above T_g via muon spin relaxation, Phys. Rev. Lett. **77**, 1386 (1996)

[38] K.H Chow, R.F Kiefl, MULTI-new detector new logic new science, Physica B, Vol 326, **1**, 279 (2003)

[39] J. E. Sonier, Muon spin rotation/relaxation/resonace, Introductory brochure (2001)

[40] R. Kubo and T. Toyabe, Magnetic resonance and relaxation, North-Holland, Amsterdam (1967)

[41] R. S. Hayano, Y. J. Uemura, Zero and low field spin relaxation studied by positive muons, Phys. Rev. B, **20**, 850 (1979)

[42] C. R. Wiebe, Studies of magnetism in rhenium and manganese based perovskite oxides, Ph,D. thesis, Mcmaster Univ, (2003)